

2011

A Left Ventricular Motion Phantom for Cardiac Magnetic Resonance Imaging

Mehmet Ersoy
Cleveland State University

Follow this and additional works at: <https://engagedscholarship.csuohio.edu/etdarchive>

 Part of the [Biomedical Engineering and Bioengineering Commons](#)

How does access to this work benefit you? Let us know!

Recommended Citation

Ersoy, Mehmet, "A Left Ventricular Motion Phantom for Cardiac Magnetic Resonance Imaging" (2011). *ETD Archive*. 671.
<https://engagedscholarship.csuohio.edu/etdarchive/671>

This Thesis is brought to you for free and open access by EngagedScholarship@CSU. It has been accepted for inclusion in ETD Archive by an authorized administrator of EngagedScholarship@CSU. For more information, please contact library.es@csuohio.edu.

A LEFT VENTRICULAR MOTION PHANTOM
FOR CARDIAC MAGNETIC RESONANCE IMAGING

MEHMET ERSOY

Bachelor of Science in Chemical Engineering

Cleveland State University

August, 2009

Submitted in partial fulfillment of requirements for the degree of

MASTER OF SCIENCE IN BIOMEDICAL ENGINEERING

at the

CLEVELAND STATE UNIVERSITY

April, 2011

This thesis has been approved
For the Department of Chemical and Biomedical Engineering
and the College of Graduate Studies by

Thesis Committee Chairperson, D.Sc. Randolph M. Setser
Department of Chemical and Biomedical Engineering

Date

PhD. Sandra Halliburton
Department of Chemical and Biomedical Engineering

Date

PhD. George Chatzimavroudis
Department of Chemical and Biomedical Engineering

Date

ACKNOWLEDGEMENT

I would like to take this chance to first express my deep appreciation and gratitude towards my parents and sisters, whose most sincere support and enthusiasm have been always with me.

I am indebted to my thesis advisor, D.Sc. Randolph Setser. He provided me with whatever I asked for with a great speed. He went to great lengths to make my life a more productive one on academic level and a happier one on personal level. I feel that I learnt immensely from him. Almost equally I have to thank great scientists, D.Sc. Melanie Kotys, who provided me insightful angles for my research. I owe these two people the regain of my self-confidence as well.

I would like to extend my gratitude towards my co-advisor, Dr. George Chatzimavroudis, who has been helping me with his advice from the time I arrived at Cleveland State University. I thank him for not abandoning me through some tough times during my studies. His advice has been right on target throughout this time. I also would like to thank my other committee member, Dr. Sandra Halliburton, for her support and suggestions during my studies. Dr. Chatzimavroudis provided me essential resources for my research and Dr. Halliburton supported my endeavors through honest advice.

I am indebted towards my friends, whose companionship made this long journey away from home bearable and joyful. In fear of leaving a name out, I abstain attempting mentioning their names here, but I will keep good memories with me here and beyond.

I don't know how many times I thanked Becky Laird and Darlene Montgomery, the best coordinators any department might have, for their help during my studies. I would also like to take this opportunity to thank them once again.

I also want to thank Dave Epperly for his remarkable help in the machine lab with the hardware.

Finally, my deep appreciation also goes to some people who helped me more than they would imagine. Uma Numburi, Carla Thompson, Xiaopeng Zhou Li, YuJaung Kim and all the undergraduate students I have taught helped me tremendously improve myself in different ways.

Thanks to anybody else that helped me finish this work.

A LEFT VENTRICULAR MOTION PHANTOM FOR CARDIAC MAGNETIC RESONANCE IMAGING

MEHMET ERSOY

ABSTRACT

The mammalian left ventricle (LV) has two distinct motion patterns: wall thickening and rotation. The purpose of this study was to design and build a low-cost, non-ferromagnetic LV motion phantom, for use with cardiac magnetic resonance imaging (MRI), that is able to produce physiologically realistic LV wall thickening and rotation.

Cardiac MRI is continuously expanding its range of techniques with new pulse sequences, including new tissue tagging techniques which allow intra-myocardial deformation to be visualized. An essential step in the development of new cardiac MRI techniques is validating their performance in the presence of motion. MRI-compatible dynamic motion phantoms are of substantial benefit in the development of cardiac specific-magnetic resonance imaging techniques. These phantoms enable the investigation of motion effects images by mimicking the three dimensional motion of the heart. To date, no single study has succeeded in duplicating both LV motion patterns, in an MRI-compatible cardiac motion phantom. In addition, a phantom that is 100% MRI-compatible with low cost to build would be desirable to researchers.

We have built two MRI-compatible phantoms, housed within a common enclosure and each filled with MRI-visible dielectric gel (as a surrogate to myocardium),

which model the wall thickening and rotation motions of the left ventricle independently. The wall motion phantom is pneumatic, driven by a custom non-ferromagnetic pump which cyclically fills and empties a latex balloon within the phantom. The rotation phantom is manually driven by a plastic actuator which rotates the phantom through a specified angular rotation. Each phantom also generates a TTL pulse for triggering the MRI scanner. Although this circuitry contains ferromagnetic materials, it can be located outside the scanner bore.

The wall thickening motion phantom has been tested using segmented cine, real time cine and grid tagged MRI acquisition sequences. Results were significant with 4% average variability and physiologically realistic wall motion.

In a separate experiment, the rotation phantom has been imaged using a triggered grid-tagged sequence during a series of repeated 15, 20 and 35 degree rotations. As above, results matched the expected rotation only with 5% average variability.

In conclusion, we have designed and built a low-cost left ventricular motion phantom, capable of accurately modeling both wall and rotation motions of the left ventricle, with up to 96% repeatability and accuracy for use in evaluating new MRI pulse sequences.

TABLE OF CONTENTS

	Page
Acknowledgement.....	iii
ABSTRACT.....	v
LIST OF FIGURES.....	ix
I. INTRODUCTION.....	1
II. BACKGROUND.....	3
2.1 Cardiovascular Function.....	3
2.1.1 Left Ventricular Function.....	4
2.1.2 The Left Ventricular Systole.....	6
2.1.3 The Left Ventricular Diastole.....	6
2.2 Magnetic Resonance Imaging.....	8
2.3 Quantification of Cardiac Function with MRI.....	14
2.3.1 Tissue Tagging.....	15
2.4 Dynamic Cardiac Phantoms.....	17
III. LEFT VENTRICLE MOTION PHANTOM DESIGN.....	23
3.1 Design Requirements.....	23
3.2 Design Solution.....	25
IV. LEFT VENTRICLE WALL THICKENING MOTION PHANTOM.....	33
4.1 Design and Construction of the LV Wall Thickening Motion Phantom.....	33
4.2 Wall Thickening Motion Phantom with Pump 1.0.....	35
4.2.1 Image Acquisition and Results for Pump 1.0.....	36

4.2.2 Discussion	40
4.3 Wall Thickening Motion Phantom with Pump 2.0	41
4.3.1 Image Acquisition and Results for Pump 2.0	46
4.3.2 Discussion	50
4.4 Wall Thickening Motion Phantom with Pump 3.0	51
4.4.1 Image Acquisition and Results for Pump 3.0	53
4.4.2 Discussion	58
V. LEFT VENTRICLE ROTATION MOTION PHANTOM	59
5.1 Design and Construction of the LV Rotation Motion Phantom	59
5.2 Wall thickening Motion Phantom with an Attached Wooden Rod 1.0	62
5.2.1 Image Acquisition and Results for Rotation Motion 1.0	62
5.2.2 Discussion	65
5.3 Wall Thickening Motion Phantom with a Plastic Actuator 2.0	65
5.3.1 Image Acquisition and Results for Rotation Motion 2.0	68
5.3.2 Discussion	102
VI. CONCLUSION	103
VII. LIMITATIONS AND FUTURE WORK	106
7.1 Limitations	106
7.2 Future Work	107
REFERENCES	108
APPENDIX (Copy Rights)	111

LIST OF FIGURES

Figures	Page
1. Time frames of systole and diastole with the measurements of intravascular pressure in the aorta, LV, left atrium (LA), and LV volume.....	5
2. Systolic and diastolic cardiac images by the use of MRI phase contrast velocity mapping technique.....	7
3. Rotation degrees of heart during systole and diastole.....	8
4. Schematic diagram of the spin echo pulse sequence.....	13
5. Schematic diagram of the gradient echo pulse sequence.....	13
6. Segments and their images between two heartbeats.....	15
7. Example of short-axis tagged images during cardiac cycle.....	16
8. Photograph of the experimental setup.....	25
9. The triggering circuit.....	28
10. Enclosed triggering circuit within the box with BNC output.....	28
11. Elements of the wall thickening motion phantom.....	30
12. Elements of rotation motion phantom.....	32
13. The wall thickening motion phantom with dimensions.....	34
14. Air pump 1.0.....	36
15. Wall motion phantom images with Air Pump 1.0.....	37
16. Cross-sectional area change as a function of time for wall motion phantom operated by the air pump version 1.0 run # 1.....	38
17. Cross-sectional area change as a function of time for wall motion phantom operated by the air pump version 1.0 run # 2.....	39

18. Percent error due to variability between different runs of wall motion phantom operated by the air pump version 1.0.....	40
19. Air pump 2.0 front view.....	42
20. Air pump 2.0 top view.....	43
21. Air Piston Pump 2.0 with attached trigger switch.....	44
22. The Air Piston Pump 2.0 with the attached triggering box and phantom.....	45
23. Change of the cross-sectional area within the wall of the gel with respect to the time for wall motion phantom when operated by the air pump version 2.0.....	46
24. The change in the volume of the endocardium in four different experimental run of the wall motion phantom when operated by the air pump version 2.0.....	47
25. Percent error due to variability between different runs for wall motion phantom operated by the air pump version 2.0.....	48
26. Set of images for wall motion phantom from different runs operated by the air pump version 2.0 for different runs at maximum, minimum and maximum cross-sectional areas.....	49
27. Set of grid tagged cine images from wall motion phantom run operated by the air pump version 2.0.....	50
28. Air pump 3.0.....	52
29. The change of the cross sectional area in four different experimental run of the wall motion phantom when operated by the air pump version 3.0.....	54
30. Percent error due to variability between different runs for wall motion phantom operated by the air pump version 2.0.....	55

31. Set of images for one beat of wall motion phantom from different 4 runs operated by the air pump version 3.0 at maximum and minimum cross-sectional areas.	56
32. Set of grid tagged cine images from wall motion phantom run operated by the air pump version 3.0.....	57
33. The rotation motion phantom with its dimensions and experimental setup.....	60
34. The distribution of the regions which are used for the analysis of the tagged images by HARP.....	61
35. The wall thickening motion phantom version 1.0.....	62
36. The rotation angle obtained in each frame during the one beat cycle for rotation motion phantom when operated by the motion mechanism 1.0.....	63
37. Set of images from rotation motion phantom operated by the motion mechanism 1.0.....	64
38. The top view of the plastic actuator.....	66
39. The front view of the plastic actuator.....	66
40. The front view of the plastic actuator with its components.....	67
41. The rotation angle obtained in each frame during the one beat cycle for 15 degree rotation run # 1.....	69
42. The non-uniform deformation percentage through the cross section of the gel for 15 degree rotation run 1.....	70
43. Set of grid tagged cine images from rotation motion phantom 15 degree rotation run #1.....	71
44. The rotation angle obtained in each frame during the one beat cycle for 15 degree rotation run #2.....	72

45. The non-uniform deformation percentage through the cross section of the gel for 15 degree rotation run 2.....	73
46. Set of grid tagged cine images from rotation motion phantom 15 degree rotation run #2.....	74
47. The rotation angle obtained in each frame during the one beat cycle for 15 degree run # 3.....	75
48. The non-uniform deformation percentage through the cross section of the gel for 15 degree rotation run 3.....	76
49. Set of grid tagged cine images from rotation motion phantom 15 degree rotation run # 3.....	77
50. The mean rotation angle obtained in three different runs # 1, 2, and 3 with 15 degree rotation.....	78
51. The percent error for the reproducibility of the rotation motion phantom 15 degree rotation for different runs 1, 2, and 3 are shown.....	79
52. The rotation angle obtained in each frame during the one beat cycle for 20 degree rotation run # 1.....	80
53. The non-uniform deformation percentage through the cross section of the gel for 20 degree rotation run 1.....	81
54. Set of grid tagged cine images from rotation motion phantom 20 degree rotation run # 1.....	82
55. The rotation angle obtained in each frame during the one beat cycle for 20 degree rotation run # 2.....	83

56. The non-uniform deformation percentage through the cross section of the gel for 20 degree rotation run 2.....	84
57. Set of grid tagged cine images from rotation motion phantom 20 degree rotation run # 2.....	85
58. The rotation angle obtained in each frame during the one beat cycle for 20 degree rotation run # 3.....	86
59. The non-uniform deformation percentage through the cross section of the gel for 20 degree rotation run 3.....	87
60. Set of grid tagged cine images from rotation motion phantom 20 degree rotation run # 3.....	88
61. The mean rotation angle obtained in three different 20 degree rotation runs # 1, 2, and 3.....	89
62. The percent error for the reproducibility of the rotation motion phantom 20 degree rotation for different runs 1, 2, and 3 are shown.....	90
63. The rotation angle obtained in each frame during the one beat cycle for 35 degree rotation run # 1.....	91
64. The non-uniform deformation percentage through the cross section of the gel for 35 degree rotation run 1.....	92
65. Set of grid tagged cine images from rotation motion phantom 35 degree rotation run # 1.....	93
66. The rotation angle obtained in each frame during the one beat cycle for 35 degree rotation run #2.....	94

67. The non-uniform deformation percentage through the cross section of the gel for 35 degree rotation run 2.....	95
68. Set of grid tagged cine images from rotation motion phantom 35 degree rotation run # 2.....	96
69. The rotation angle obtained in each frame during the one beat cycle for 35 degree rotation run # 3.....	97
70. The non-uniform deformation percentage through the cross section of the gel for 35 degree rotation run 3.....	98
71. Set of grid tagged cine images from rotation motion phantom 35 degree rotation run # 3.....	99
72. The mean rotation angle obtained in three different 35 degree rotation runs # 1, 2, and 3.....	100
73. The percent error for the reproducibility of the rotation motion phantom 35 degree rotation for different runs 1, 2, and 3 are shown.....	101

CHAPTER I

INTRODUCTION

Cardiovascular disease is the main cause of death for 17.1 million people every year in the world [1]. Because the heart is an electro-mechanical pump, assessment of its mechanical function plays an important role for the diagnosis and prognosis in patients with cardiovascular disease. To this end, researchers have sought to evaluate the left ventricular (LV) function and quantitatively assess the heart's functionality by analysis of wall deformation [2, 3]. Many Magnetic Resonance Imaging techniques have been developed to help researchers meet this goal [4]. However, these techniques can be difficult to apply to patients or volunteers for validation because of the long examination time and lack of sufficient accuracy and repeatability of motion patterns in vivo, especially with breath hold scanning sequences.

Many of these limitations can be overcome with the design and construction of moving MRI-compatible heart models called dynamic cardiac phantoms. These phantoms duplicate the motion patterns of the heart in vitro, assuring the control of the motion without time or comfort limitations. In addition, the constant physiology of

phantoms is superior when compared to the deformation patterns encountered in vivo. Thus, phantoms have become a valuable tool in the validation of new cardiac-specific MRI techniques.

Although cardiac phantoms have improved research into cardiac-specific MRI techniques, most of the existing cardiac phantoms are expensive and complicated. Additionally, researchers have not yet built a sophisticated 3D dynamic phantom that duplicates both the wall and rotation motion patterns of the left ventricle of the heart.

We believe that a dynamic cardiac phantom with the capability of accurately modeling both wall thickening and rotation motions of the left ventricle will be a valuable tool in evaluating new pulse sequences. The aim of this study, therefore, was to design and build a low-cost, non-ferromagnetic dynamic left ventricle phantom with sufficient accuracy and repeatability for use with cardiac MRI. In addition, we sought to validate this phantom using a variety of commonly used cardiac MRI imaging techniques.

The remainder of this thesis is organized as follows:

Chapter 2 describes the relevant background material, including reported discussion of previously reported cardiac motion phantoms. Chapter 3 describes the design requirements for LV motion phantom. Chapter 4 describes the LV wall thickening motion phantom. Chapter 5 describes the LV rotation motion phantom. Chapter 6 includes the conclusion and future work of the current study.

CHAPTER II

BACKGROUND

2.1 Cardiovascular Function

From the first studies of the heart, it is well known that the heart functions like a pump to circulate blood through the body. Its structure and its function are inseparable aspects. The heart embodies four cardiac components: right and left atria, and right and left ventricles. Each component has its specific features and its own structural characteristics [5]. By the contraction of the ventricles, the right side of the heart pumps blood through the lungs and the left side pumps blood through the aorta to the peripheral organs. During the filling of the heart, the atria assist to move blood into ventricles [6]. Heart function has two distinct phases: systole and diastole. The systolic and the diastolic function of the heart consist of ventricular motions of thinning, shortening, lengthening, widening and twisting. Myocytes cause the ventricular contraction. The clock wise and anti-clockwise spiral muscle pattern causes the ventricular twisting [5]. The heart has three distinct layers of tissue: epicardium (external layer), myocardium (middle layer)

and endocardium (inner layer). Changes in volume in the different layers of the heart due to the ventricular motion are not in equal amount to each other.

2.1.1 Left Ventricular Function

The best way to understand left ventricular function is to be familiar with its structure. The electrophysiological and elastomechanical performance of the left ventricle is created by the structural features of the heart [7]. The left ventricle walls consist of a collagenous matrix and branching myocytes. The myocytes are lined up well, branched, and are also fixed within the collagenous matrix. In the anchored structured formation of muscles, there are gaps between the neighboring myocytes. In fact, it is believed that those gaps are necessary for wall thickening during the systolic phase [8]. The normal mechanical events of a cycle of the left ventricle can be defined as one complete sequence of contraction and relaxation. The ventricular muscle contraction phase is referred as systole and the ventricular muscle relaxation phase is referred as diastole. At a normal resting heart rate, the heart spends around two thirds of the cardiac cycle in diastole and one third in systole. According to this physiological behavior of heart, volume change in the left ventricle during the systole and diastole phase is shown as Figure 1 [5].

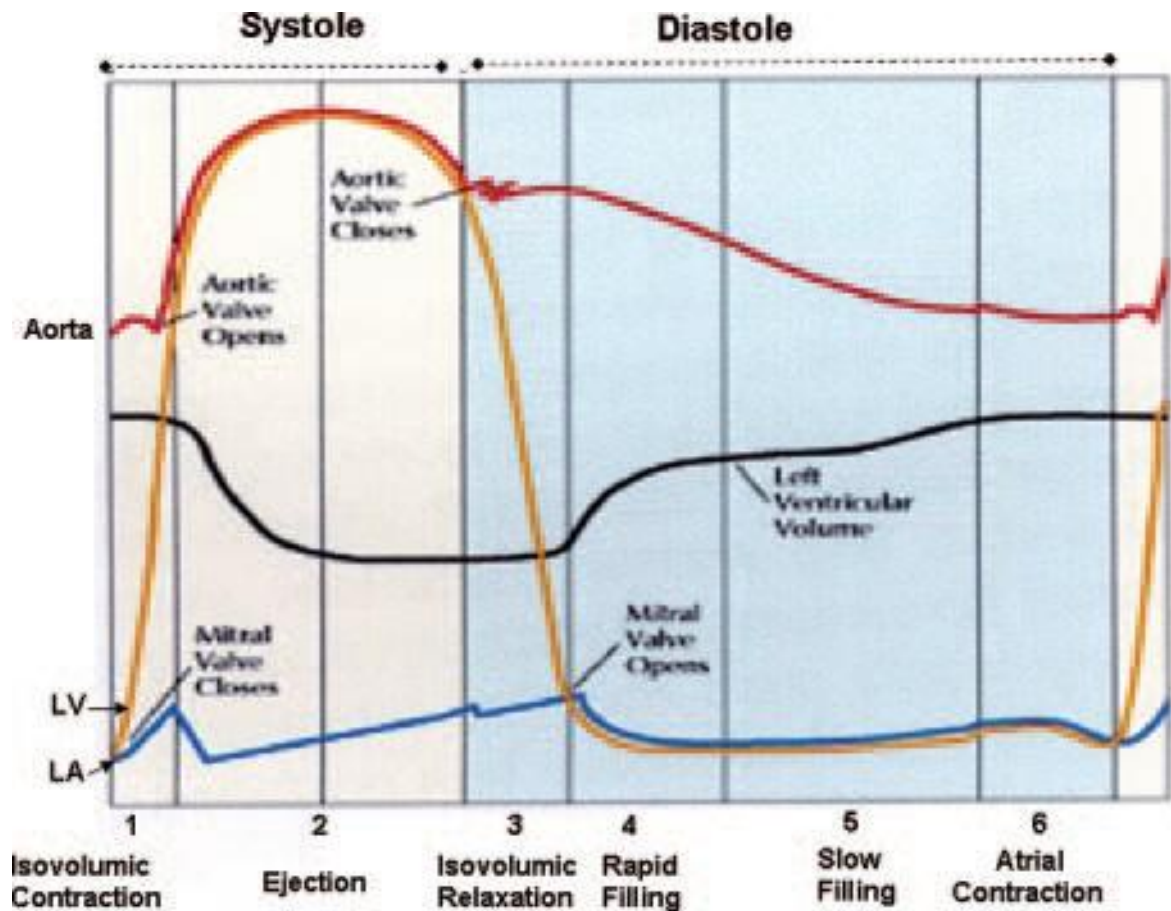


Figure 1. Time frames of systole and diastole with the measurements of intravascular pressure in the aorta, LV, left atrium (LA), and LV volume. (From [5]. Used with permission. See appendix)

The change in the LV intravascular pressure is due to multi-directional ventricular motions within the LV wall. Overall, these ventricular motions can be defined as two distinct motion patterns: wall thickening and rotation motion. The wall thickening and rotation motion patterns are explained according to events of a cycle of the left ventricle: the ventricular systole and the ventricular diastole.

2.1.2 The Left Ventricular Systole

The ventricular systole begins with the result of electrical stimulation which causes myocytes contraction and results in high fiber tension and short fiber length. This change in fibers causes thickening in the ventricular wall and decrease in ventricular volume thus sequential ventricular emptying happens [5]. During the contraction of left ventricle, the epicardium does not have noticeable change in its wall thickness while the endocardium contracts towards its center and increases the thickness of myocardium wall. The amount of blood ejected from the left ventricle during a single cycle is called stroke volume. The stroke volume is the difference between the ventricular end diastolic volume and ventricular end systolic volume. The left ventricle reaches its minimum or end systolic volume at the end of systole. For a healthy heart, the normal end systolic ventricular volume range is 16 to 143 ml and typical value is 50 ml [9].

2.1.3 The Left Ventricular Diastole

The ventricular diastole is the phase during which the myocardium and endocardium returns to its initial length and tension relationship [10]. During the diastole, the relaxation of the fibers result in widening of the endocardium and decrease in the wall thickness of the myocardium. Thus, pressure and volume increase. The normal left ventricular diastolic function is defined as the ability of ventricle to fill to a normal end-diastolic volume [10]. The left ventricle reaches its maximum or end diastolic volume at the end of diastole. For a healthy heart, the normal end diastolic ventricular volume range is 65 to 240 ml and typical value is 120 ml [9]. When the typical end diastolic ventricular

volume is subtracted from the typical end systolic ventricular volume, the typical stroke volume is found as 70 ml and according to age and body size it ranges from 55 to 100 ml.

When the end systolic and the end diastolic endocardial and epicardial contours are examined in the MR images, the rotation motion is observed in the left ventricle of the heart. The rotation motion of the left ventricle is created by the clockwise and anti-clockwise spiral muscles. The counterclockwise rotation of the apex (bottom part of the heart) and clockwise rotation of the base (upper part of the heart) occurs during the muscle's contraction of the left ventricle. Then, this rotation motion reversely occurs to create a phase of relaxation (diastole). Systolic and diastolic cardiac images which show the rotation motion are shown in Figure 2 [5].

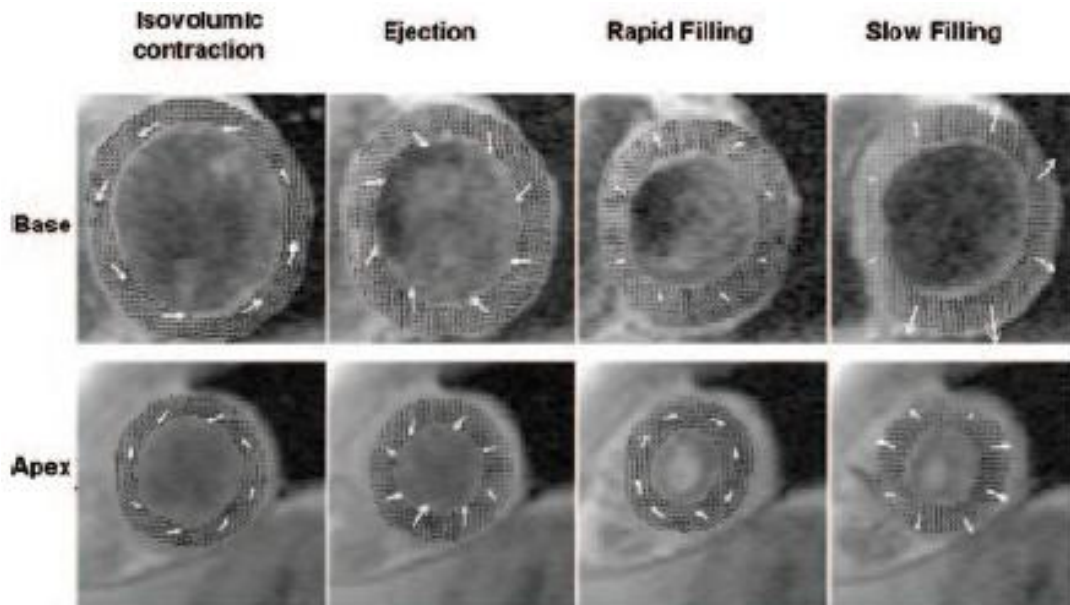


Figure 2. Systolic and diastolic cardiac images by the use of MRI phase contrast velocity mapping technique.(From [5]. Used with permission. See appendix)

Observed and quantified left ventricular rotation at the wall surface is 5.1 ± 1.2 degrees in clockwise direction at base and 11 ± 1.2 degrees anti-clockwise direction at apex. According to measurement at apex and base, the total amount of twist created by the each beat of heart is 16 ± 2.4 degree. During the systole and diastole periods of heart, the rotational degrees are also represented as in Figure 3 [5].

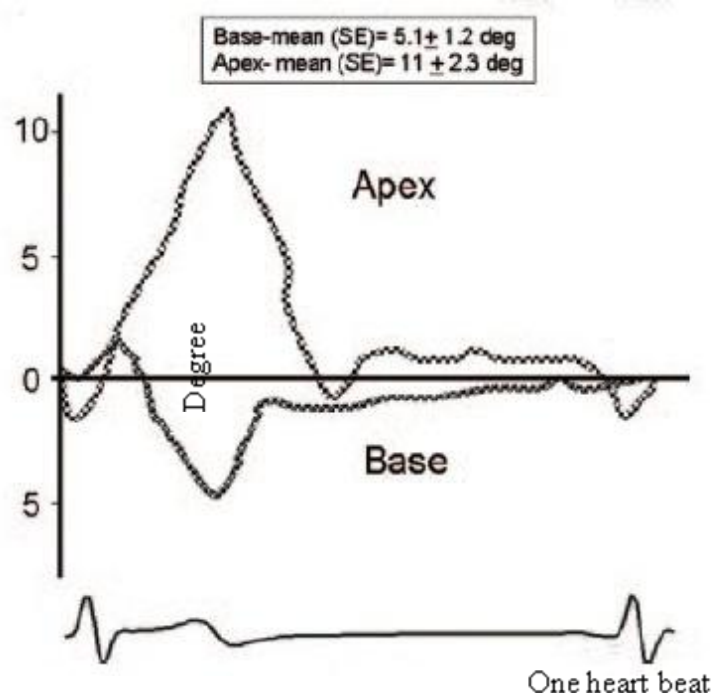


Figure 3. *Rotation degrees of heart during systole and diastole.*(From [5]. Used with permission. See appendix)

2.2 Magnetic Resonance Imaging

Magnetic resonance imaging (MRI) is a non-invasive imaging modality that uses powerful magnets and radio waves. A single proton in each hydrogen nucleus has an electric charge and spin around its axis. The 63% of the human body consists of hydrogen

atoms and spins of hydrogen protons in the human body are aligned by the high-strength static magnetic field. These aligned spins are excited and detected with coils. The two different relaxation times, proton density, flow and motion, changes in susceptibility, molecular diffusion, magnetization transfer, etc. affect the signal arising from the tissues [6]. The image contrast is determined by the excitation pulses and magnetic field. The four main principles of MRI are called: excitation, relaxation, localization and data acquisition.

In general, the small magnetic fields, which are produced by the spinning of each proton around its axis at water nucleus, are randomly oriented. By the existence of an external large magnetic field (such as an MRI scanner), protons will be aligned parallel to the long axis of the external magnetic field (B_0). The addition of all the small magnetic fields of the protons will create an equilibrium magnetization which is much smaller than B_0 . The interaction of the external large magnetic field and equilibrium magnetization is via a property called “spin”. The precession of this spin with a specific frequency is formulated by Larmor Equation [6]. The frequency of precession (ω) depends on a constants called the gyromagnetic ratio (γ) and the magnetic field strength (B_0). The gyromagnetic ratio for hydrogen is 42.7 MHz/Tesla.

$$\omega = \gamma B_0 \qquad \text{Eq. 2.1}$$

A higher magnetic field strength will result in a higher precession frequency.

The magnetic moment of each proton has two perpendicular components, called longitudinal and transverse. The sum of the all components results in only longitudinal

magnetization by the cancellation of the transverse components. As a result, the longitudinal magnetization composes the net magnetization which is aligned by the external magnetic field (B_0).

Excitation

Once the magnetic field of the body is aligned by the external magnetic field (B_0), a second external magnetic field (B_1) is applied to make the body emit a signal. This signal is the result of increasing the number of transitions from lower to higher energy state of the protons. This is one of the four main principles of MRI which is called excitation. By applying the B_1 field as a radiofrequency (RF) pulse, the net magnetization vector is flipped from z-axis to the xy plane. However, B_1 is required to be perpendicular to B_0 and the frequency of precession of the proton must be same as the applied radiofrequency to be able to achieve a successful excitation signal. The resulting transverse magnetization, which consists of the magnetization vectors flipped into xy plane, has a major importance in constructing the image. Since, MRI receiver can only detect the component of the magnetization vector which is in the xy plane. In addition to that, in a desire to localize in a specific part of the body, it is needed to detect signals only from the region of interest. In that case, the frequency of precession of the protons in that region happen to be different from the other parts of the body and this can be done by applying the magnetic gradient field when the RF pulse is applied.

Relaxation

After the excitation, relaxation of the protons occurs. Excited protons realign themselves from induced transverse magnetization to the longitudinal magnetization

(equilibrium state) by transmitting their gained energy. Excited protons transmit their energy by the RF pulses to the surrounding regions.

Relaxation has two distinct modes called T1 and T2 relaxation. Both of them are distinct properties of the material according to its physical and chemical properties and the surrounding environment. T1 is called the longitudinal relaxation time. In other word, T1 is the time it takes for the spins to realign along the z-axis [11]. During T1, the spins give the energy back, which they obtained from the RF pulse, to the surrounding lattice to go back to equilibrium state. T2 is the decay of magnetization perpendicular to the main magnetic field. T2 time is related to the effect of spins on each other. T2 time characterizes the rate at which the xy vector component decays.

Localization and Data Acquisition

To be able to distinguish the signals created by applying RF pulse in the whole body at the excitation, spatial encoding of the signal is performed. Spatial encoding is achieved through three steps which are slice selection, frequency encoding and phase encoding.

Slice selection is performed simultaneously by applying a gradient on the magnetic field with the RF pulse before the spatial encoding. After selecting a slice, another gradient G_x called the frequency encoding gradient is applied in the x-direction. By application of G_x , a difference in the precessional frequencies is created at different x levels. One more gradient G_y called the phase encoding gradient is applied also in y-direction. G_y is applied to perform phase encoding. G_y creates a different accumulated

phase at different y levels [12]. During the application of G_x and G_y , the signal is acquired or read out.

The strength and duration of the magnetic gradient determines the magnitude of the phase difference between the protons. Created phase differences are the part of required data to fill the k -space which will lead to final image by the Fourier Transform. Created phase differences between the protons may lose their coherence and lead to signal loss during the data acquisition. To prevent that situation, a pulse sequence is used. There are two different pulse sequences which are called spin echo (Figure 4) and gradient echo (Figure 5). Spin echo is created by employing two RF pulses while gradient echo is created by employing one RF pulse and magnetic field gradient.

The application order of RF pulse, magnetic field gradient, spatial encoding and their timing is called as a pulse sequence. Repetition of pulse sequences will result in collecting the required data to fill the k -space to create image. Time between the two consecutive RF pulses is called the repetition time (TR) and the time between the RF pulse and resulting echo is called echo time (TE).

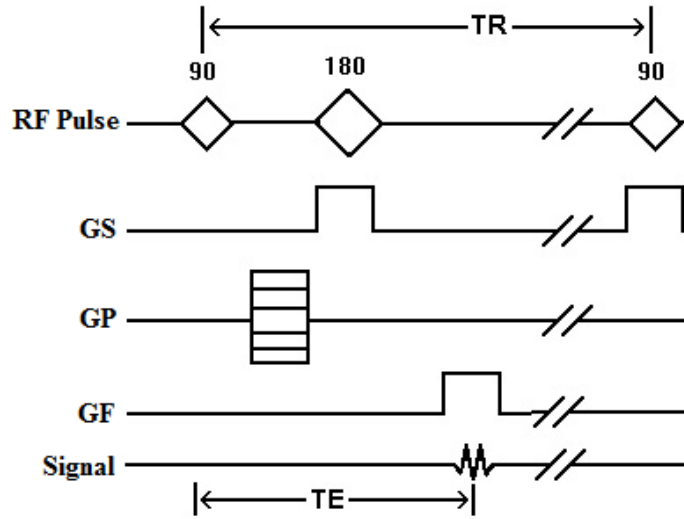


Figure 4. Schematic diagram of the spin echo pulse sequence where RF is radio frequency pulse, GS is slice selection, GP is phase encoding, and GF is frequency encoding.

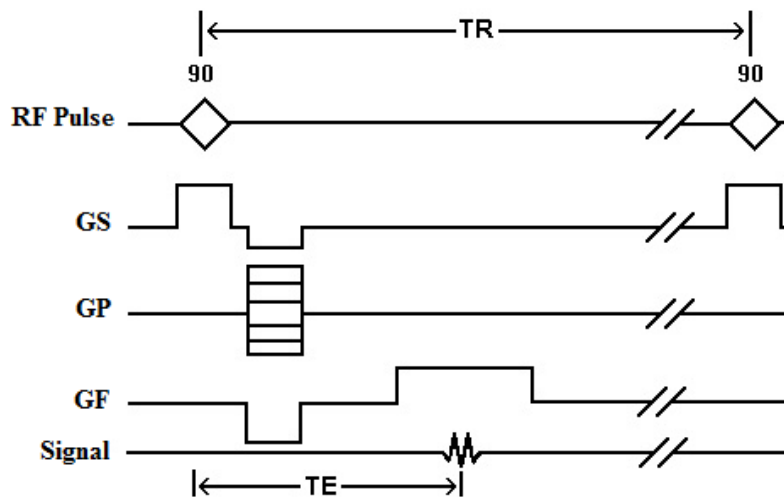


Figure 5. Schematic diagram of the gradient echo pulse sequence where RF is radio frequency pulse, GS is slice selection, GP is phase encoding, and GF is frequency encoding.

2.3 Quantification of Cardiac Function with MRI

As the heart is an electro-mechanical pump, assessment of its function plays an important role for the diagnosis and prognosis in patients. Cardiac activity has been studied by MRI since the middle of 1980's. However, it is still an evolving area due to fundamental problems related to cardiac motion.

Cardiac MRI can be used to quantify function of the left and right ventricle aortic flow, vascular function as well as cardiac volume function. Most clinical cardiac MRI examinations are done by 1.5T MR scanners. The spin echo MR sequences are typically used to show anatomy. For the functional imaging of moving regions, the gradient echo sequences are used. The cardiac MRI technology has growth very rapidly and new faster sequences to acquire the images as well as post processing of these images with minimal user interaction are created [9].

Left ventricular function is a very important diagnostic and prognostic factor for patients with heart disease [13]. Cardiovascular MRI with its reproducibility is used in quantification of ventricular volumes, ejection fractions and mass [6]. As it has been discussed in section 2.1.1, together rotational and wall thickening motion causes the left ventricle to exhibit complex motion patterns and results in difficulty to analyze anon. In spite of all challenges, there has been development of new techniques to assess the motion of left ventricle noninvasively.

With the stronger gradients and faster gradient switching capabilities of MR devices, new techniques for cine imaging enables to acquire a series of images through

the cardiac cycle. By cine imaging, a movie of a specific region or whole heart can be created and amount of data acquired can be customized by the user.

Commonly, each cardiac cycle is divided into segments and images are acquired for each segment. By the use of the images of each segment, the movie of the heartbeat is created. The sample images of the segments are shown in Figure 6 [12]. This technique is commonly used to study ventricular contractility and vascular function.

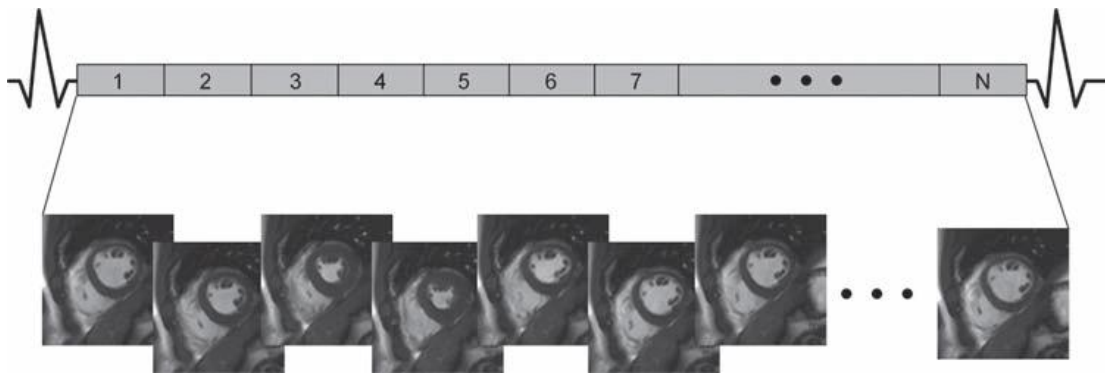


Figure 6. *This figure represents the segments and their images between two heartbeats [12].*

2.3.1 Tissue Tagging

Cine imaging makes possible to see the motion of the endocardium wall thickening. However, accurate measurement of the wall deformation within the walls is possible with using MRI tagging technique. Since 1988, line, radial and ring tagging which are created on myocardium have been used to calculate the strain, shape and function of ventricles [6].

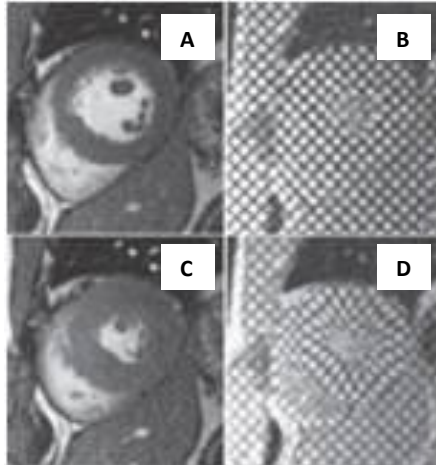


Figure 7. *Example of short-axis tagged images during cardiac cycle. A) Cine image of LV at end diastole, B) Tagged cine image of LV at end diastole, C) Cine image of LV at end systole, D) Tagged cine image of LV at end systole.*

Tagging of the tissues is achieved by applying excitation pulses prior to the applying the RF pulses required for imaging. Tissue's signal is destroyed in excited plane right before the imaging so that no signal is received from the protons of tissue and they look like black lines or areas (Figure 7). Highly reproducible data can be obtained in the heart by tissue tagging to analyze more sophisticated mechanical metrics of the heart such as wall thickening, strain and torsion. During the cardiac cycle, the displacement of each tagged area according to rotation or wall thickening motion of the heart can be followed from the acquired images and becomes possible to quantify the myocardial deformation by tracking tag lines [14, 15]. The mechanical properties of the heart are an accurate evaluation of the normal and diseased heart. Therefore, the use of tagging

increasingly becomes valuable in clinical applications to predict the clinical risk assessment and evaluate the therapeutic efficacy.

2.4 Dynamic Cardiac Phantoms

An essential step in the development of new cardiac MRI techniques is validation of their performance in the presence of cardiac motion. Commonly, validation is accomplished by scanning patients or volunteers. MRI-compatible dynamic motion phantoms, which mimic the motion patterns of the LV, can be of substantial benefit in the development of cardiac MRI techniques. However, there are two distinct components of LV motion, wall thickening and rotation. To date, no single MRI-compatible motion phantom has succeeded in duplicating both of these LV motion patterns. Most existing cardiac phantoms are expensive, are not 100% MRI-compatible; and cannot be easily modified for different settings. There are two general types of phantoms used for cardiovascular applications: flow phantoms and motion phantoms, discussed separately below.

Flow Phantoms

In healthy subjects, the flow profile in the cardiovascular system is often different than in subjects with cardiovascular disease, such as narrowing in a blood vessel or a malfunctioning heart valve. Flow phantoms can be scanned and the resulting images used to analyze flow patterns, either qualitatively using flow visualization or quantitatively using fluid mechanics principles [16]. Also, flow phantoms can be used for the assessment of new MRI techniques. Due to the existence of complex geometries such as in arteries, it is hard to achieve a completely noninvasive approach for the rapid

assessment of MRI new techniques with volunteers or patients [17]. Flow patterns are challenging to reproduce repeatedly in vivo for the validation of new techniques. Even with in vitro experiments, there can be obstacles such as the disruption of flow patterns by the presence of air bubbles in the phantoms [17].

As an example, In 1999, Smith et al. designed and built a phantom to duplicate the geometry of the stenotic carotid bifurcation. This phantom features variable stenotic geometries within the internal carotid artery [17]. The phantom was made from MRI-compatible materials. A durable, rigid geometry was attained by the use of plastic polyester. First, an aluminum mold was created to shape the stenosis model. Then, the plastic resin was poured into the container of aluminum mold. Once the plastic resin solidified, the mold was melted out. Finally, an agar gel was poured into the plastic housing of the model to achieve the tissue-like signal. A computer controlled flow pump was employed to have pulsatile or constant flow during the MRI examination. A water-glycerol mixture was used as an blood mimicking fluid. The resulting images obtained from MRI concluded that the phantom data were similar to anatomical properties. It was concluded that this realistic anthropomorphic carotid bifurcation phantom can be used for verification of magnetic resonance angiography techniques which quantify the stenosis severity and blood flow [17].

Left Ventricle Motion Phantom

Several attempts have been made to design and build dynamic motion phantoms with sufficient sophistication to model the physiological motion of the heart. However, these phantoms have not replicated the true motion of the left ventricle. Previous dynamic

cardiac phantoms were limited in that they cannot duplicate both the wall thickening and rotation motions of the left ventricle and are not fully MRI-compatible.

A low-cost MRI compatible moving phantom was created to investigate the motion phenomena related to respiratory and cardiac contraction motion [18]. The motion was modeled with a K'NEX plastic construction toy set. The phantom included several small gelatin filled containers and one small tube filled with corn oil, all of which were located in the phantom head. A fiber optic connection set was used for synchronization of the data acquisition with the phantom motion. The periodic interruption of a transmitted laser beam resulted in creation of signal. This signal was converted to TTL pulse. The presented phantom enabled the investigation of motion related phenomena in MR images by only rotation of the tubes [18]. However, rotating tubes did not simulate LV wall motion or myocardium.

Khan et al. designed and constructed a dynamic cardiac phantom for MRI to perform standard performance tests in the presence of motion. In this phantom, the pseudo-respiratory motion in both the anterior-posterior and cranio-caudal directions was duplicated [19]. Silicone and acrylic materials were used to achieve the motion of the moving heart structure and flowing blood motion. An MRI compatible flow pump was connected to mimic the blood flow through the chambers of heart. Successfully, there has not been any motion effects observed in images of this phantom when it was tested in three different MR Manufacturer systems: GE, Philips and Siemens [19]. However, phantom needed to have further modifications to achieve realistic cardiac motion.

In another study [20], a cardiac phantom was created to test and validate the gated cardiac single-photon emission computed tomography (SPECT) and to test different acquisition parameters. The phantom was able to produce variable left ventricular volumes and ejection fraction. The inner and outer wall of the left ventricle was modeled by filling the space between 1 mm thick flexible silicone membranes with radioactive solution. The volume between the silicone membranes was changed by driving a motor controlled piston. The piston followed an outline of a curved cam which was the connection between the piston and motor. Therefore, because of the shape of the cam, a physiological stroke volume curve was achieved by the motion of silicone membranes. The motion of the phantom was synchronized with a simulated ECG signal when the membranes reached the maximum modeled left ventricular filling volume. The stroke volumes measured from the examinations were constant. This phantom was successfully produced to monitor the stability of the single-photon emission tomography performance and quantification measurements [20]. The main limitation of the phantom was the small range of the producible heart rate which was limited between 60 to 80 beats per minute.

Myocardial velocities were measured using a MRI-compatible model of the left ventricle phantom [21]. The left ventricle was modeled by two concentric cylinders and space between them filled with the polyvinyl alcohol cryogel to mimic the myocardial tissue. To be able to create three dimensional motion, two motors concurrently were operated. One of the motors provided movement linearly along the axis of the MR magnet bore, the other one rotated the phantom in the transverse plane. The motors were operated by a computer. The motion of the phantom was synchronized by a 5V pulse at the beginning of each motion as an ECG input to the MRI scanner. This phantom was

used to measure the myocardial velocities by navigator echo gated phase contrast MRI in vitro. However, phantom was able to rotate maximum 6 degrees which was so small compared to actual rotation in the heart. In addition, three dimensional tissue velocity measurements in the myocardium of the patients and volunteers were done by phase contrast MR sequence. Seventeen healthy volunteers and twenty eight patients were scanned for the phase contrast MR velocity image acquisition. Comparison of in vitro and in vivo results showed the feasibility of the combining phase contrast MR imaging with navigator echo respiratory gating to acquire the 3D velocity data in myocardial tissue without breath holding [21].

A biventricular phantom which mimics the deformation of tissue similar to the human left ventricular wall was built out of polyvinyl alcohol for use in imaging by ultrasound [22]. The polyurethane elastomer mold was used to construct the phantom. One of the ventricles modeled the right ventricle with uniform wall and the dividing uniform wall between the left and right ventricle. The other one modeled the wall thickening motion of the left ventricle. The deformation was achieved by a computer controlled motor driven piston pump. The piston pump was used to move water reciprocally to mimic the beating left ventricle. The trigger signal was acquired from the pump controller and sent to the ECG input of the scanner. This phantom was able to reproduce the cyclic deformation of the ventricles while mimicking the mechanical and acoustic properties of the tissue [22]. The system reproducibility was satisfactory. One of the limitations of this study was that the phantom did not have mechanical anisotropy which is having a different magnitude when measured in different directions. The other was that the phantom was lack of the rotational motion component of the left ventricle.

Current Phantom Study

In summary, there has not been a study which has succeeded in duplicating both motion patterns of the left ventricle rotation and wall thickening, in a cardiac phantom to enable standard performance tests of new MR imaging techniques. In addition, a phantom that is 100% MRI-compatible with low cost to build would be desirable to researchers.

In this study, our aim was to design and build a dynamic cardiac motion phantom with the capability of accurately modeling both the wall thickening and rotation motions of the left ventricle with sufficient reproducibility for use in evaluating new pulse sequences. The mechanism is manually operated without need of any powered motor and is totally MRI-compatible, except for the attached triggering mechanism which generates a TTL pulse for triggering the MRI scanner. It is very easy to set up and use, and it can easily be reproduced with low cost even by user-specific modifications. Cardiac phantom is imaged in Philips 3T Achieve MRI Scanner and results are analyzed via dedicated Philips analysis tool and harmonic phase (HARP) diagnostic software. This is the first time that a 98% MRI-compatible phantom with significant ability of modeling the wall thickening and rotation motions of the left ventricle has been designed and built.

CHAPTER III

LEFT VENTRICLE MOTION PHANTOM DESIGN

3.1 Design Requirements

As discussed previously, there are two distinct components of left ventricular motion, wall thickening and rotation, which occur concurrently as the heart contracts. The wall thickening motion is observed as a thickening of the myocardium, and the rotation motion is observed as the twisting of the left ventricle about its long axis.

In practice, these two distinct motion patterns are quantified separately. Thus, we have developed two separate phantoms, within a common enclosure, to reproduce these motions independently. Our main scope is to create a cardiac phantom which does not need any motors in the experimental setup for motion generation. So, the basic elements of the left ventricular moving phantoms (wall thickening and rotation motion phantom) were the air pump, rotation motion actuator, trigger circuit, and an air pump. The air pump and rotation motion actuator were human operated.

For the MR phantoms, there are two main restrictions: the size of the phantom, which will be located in the bore of the magnet, and the materials used in the phantom

and the experimental setup. The size of the phantom's enclosure is limited to 13 inches in width and 13 inches in height for the Philips Achieva MRI Scanner. Each phantom needs to be similar to actual heart's size as well as heart's structural components.

On the other hand, selection of the construction materials used for the phantoms is also an essential step. It is very important to be aware of that working around a superconducting magnet that the magnetic field is always on. Therefore, ferromagnetic and non-ferromagnetic metallic material cannot be used in the experimental setup or within the phantom itself. Otherwise, the equipment could be pulled to the magnet bore and could result in serious injuries for the individuals and potentially damage the MRI scanner as well. Therefore, the phantom and the experimental setup were constructed exclusively of non-ferromagnetic materials (polycarbonate, wood, latex, sponge, dielectric gel) except for the triggering circuit. However, the triggering circuit was placed outside the scanner's Gauss line during the operation.

Both wall thickening and rotation motion phantoms are required to have a ring of gel inside to mimic the left ventricle wall during operation of the phantom. This gel should be MRI visible and mimic both the elasticity and T1/T2 of myocardium. The thickening in the wall motion phantom and the rotational deformation in the rotation motion phantom should be adjustable for different amounts and physiologically realistic. Deformations within the gel for both phantoms should be periodic and reproducible. It is technically challenging but operation of wall and rotation motion phantoms are ideally expected to be concentric as it is in the heart.

3.2 Design Solution

Considering these requirements, an experimental setup (Figure 8) housing two different phantoms were designed and built to duplicate the wall thickening and the rotation motion of the mammalian left ventricle separately. The cycle of the motion patterns was assumed to be purely periodic. The deformation patterns were uniform through the circumference of the phantoms.

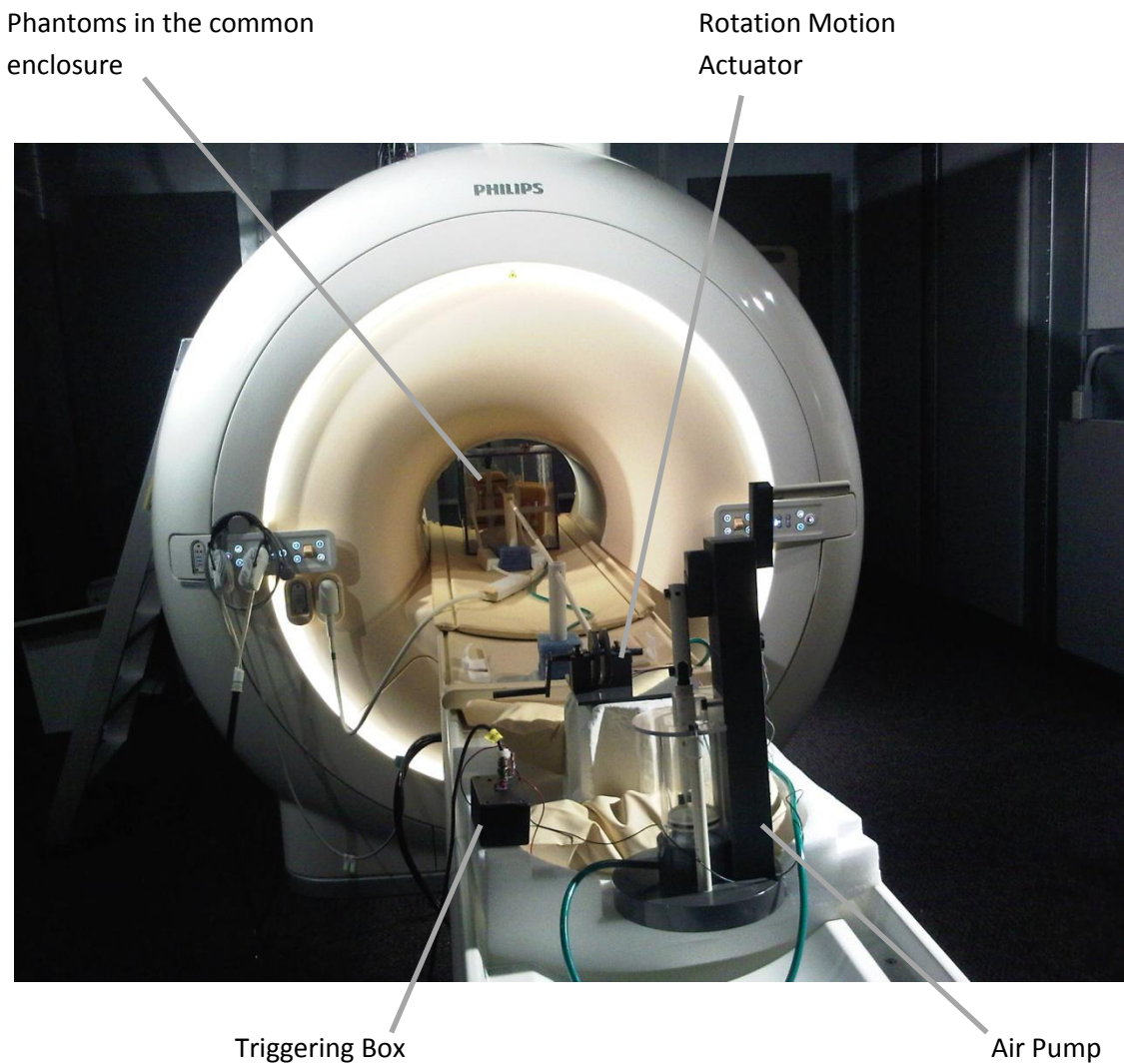


Figure 8. *Photograph of the experimental setup.*

In the construction of the phantom, air pump, and rotation motion actuator, polycarbonate was used as the primary building material. The common enclosure of the phantoms was 13 inches both in height and width. All the structural materials, joint connectors, screws and rods were MRI compatible.

Each phantom was filled with a commercially available di-electric silicone gel (Dow Corning Sylgard 527), which was used to model the myocardium in both the wall thickening and rotation phantoms. The Sylgard 527 di-electric gel retains much of the stress relief and rapid self-healing, and is naturally tacky surface. Therefore, it was stable enough to deform and reform to its initial state over and over at each cycle with uniform shape. Also, the tacky nature generated a great ability to re-heal the gel if damaged or was exposed to stress more than it could absorb. The gel was shipped as 2 separate parts; the part A and part B of the silicone gel product were in very low viscosity liquid form. At room temperature, the two parts were filled into the phantoms with mixing them 1:1 ratio. During the mixing process, one key point was to avoid generating air bubbles within the gel. Therefore, pouring of the parts into container or directly into phantom should be done very slowly by preventing the agitation. Once the gel was poured into the phantom, it was left to cure at least for one day. Then, it was ready to be used in the experiments. The gel was able to mimic the T1 and elasticity of the myocardium. Both wall thickening and rotation motion phantoms each had hard plastic cylindrical shell in 0.25 inches thickness and 0.9 inches thick ring of gel inside to mimic the left ventricle wall during operation of the phantom.

At each phantom's motion mechanism, a trigger switch was mounted to generate transistor-transistor logic (TTL) pulse by the use of trigger circuit to synchronize the data

acquisition with movement of the phantom. The MRI scanner had input for the external TTL signal. The wall thickening motion was triggered when the minimum thickness of the gel was achieved and the rotation motion was triggered at the beginning of each rotation cycle. The trigger circuit consists of 555 timer chip, resistors, capacitors, battery and switch. The 555 timer chip was used in systems to create continuous series of pulses with the periodic motion of the phantom. Figure 9 shows the triggering circuit and Figure 10 enclosed triggering circuit within the box with BNC output. This circuitry contains ferromagnetic materials but could be placed outside the scanner. However, no artifacts in the images were introduced by the trigger unit. Trigger pulse was transformed into transistor-transistor logic (TTL) pulse by transformer with 5V voltage output and connected to the external TTL signal input of the scanner. The transformer powered by 9V battery.

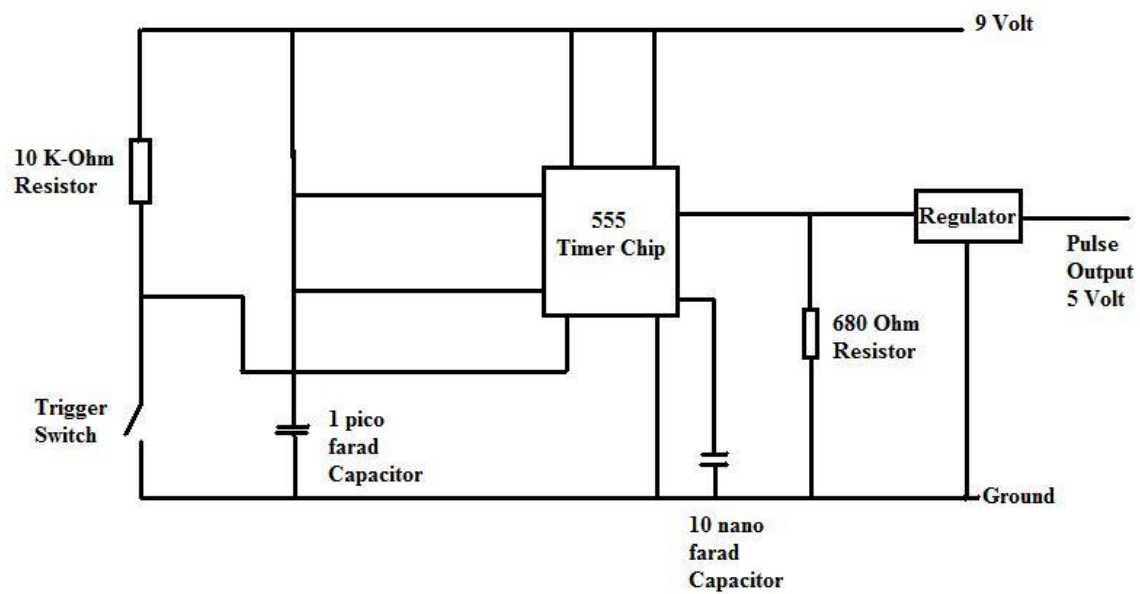


Figure 9. *The triggering circuit*

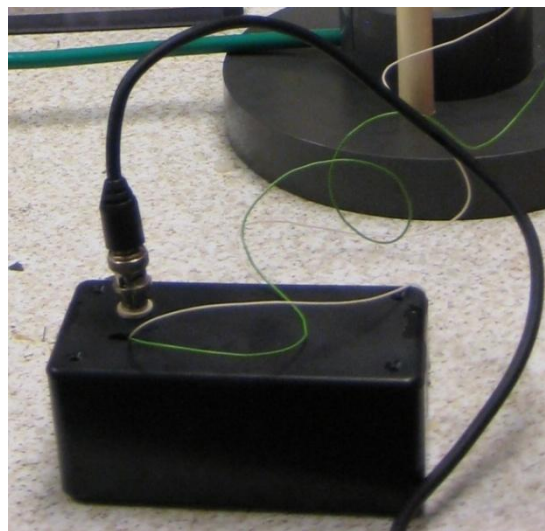


Figure 10. *Enclosed triggering circuit within the box with BNC output.*

Both for wall and rotation motion phantoms, no motors were attached to system to operate the phantoms. The present solution for the wall motion phantom was a pneumatic mechanism, driven by a custom non-ferromagnetic pump which cyclically fills and empties a latex balloon within the phantom. The variability of the motion could easily be adjusted by three different volume settings of the air pump. Figure 11 shows the wall motion phantom experimental setup components. The wall motion phantom will be discussed in more detail in Chapter 4.

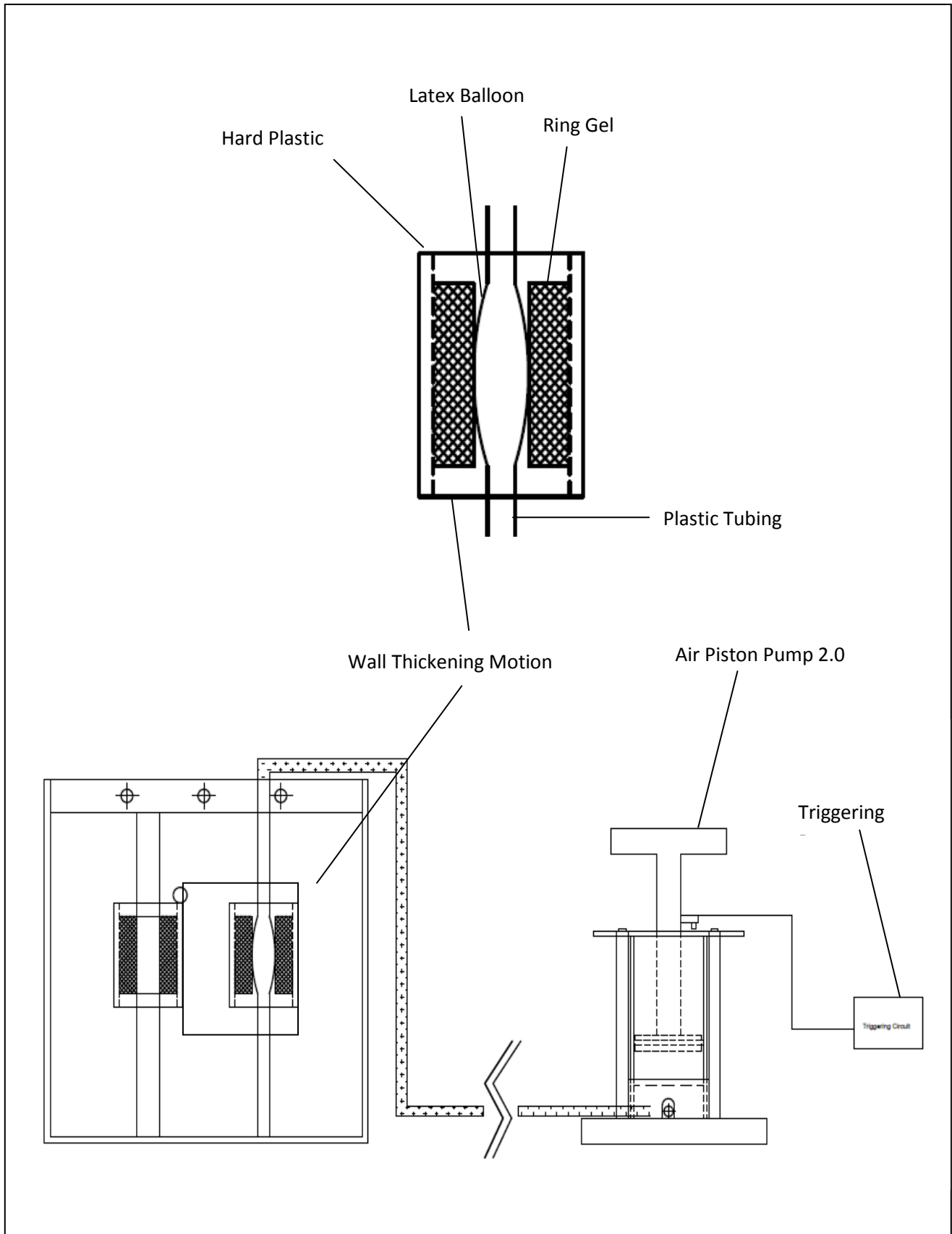


Figure 11. *Elements of the wall thickening motion phantom*

The rotation phantom is manually driven by a wooden rod attached to the phantom outer wall which rotates the phantom through a specified angular rotation. The other end of the rod was attached to plastic actuator which was operated by the human to create continuous cyclic displacement of the rod. Gel deformation was achieved by displacing the attached rod and rotating the outer wall of the phantom while the concentric inner cylinder was fixed. The variability of the rotation motion could easily be adjusted by different rotation amount settings of the actuator. The Figure 12 shows the rotation motion phantom experimental setup components. The rotation motion phantom will be discussed in more detail in Chapter 5.

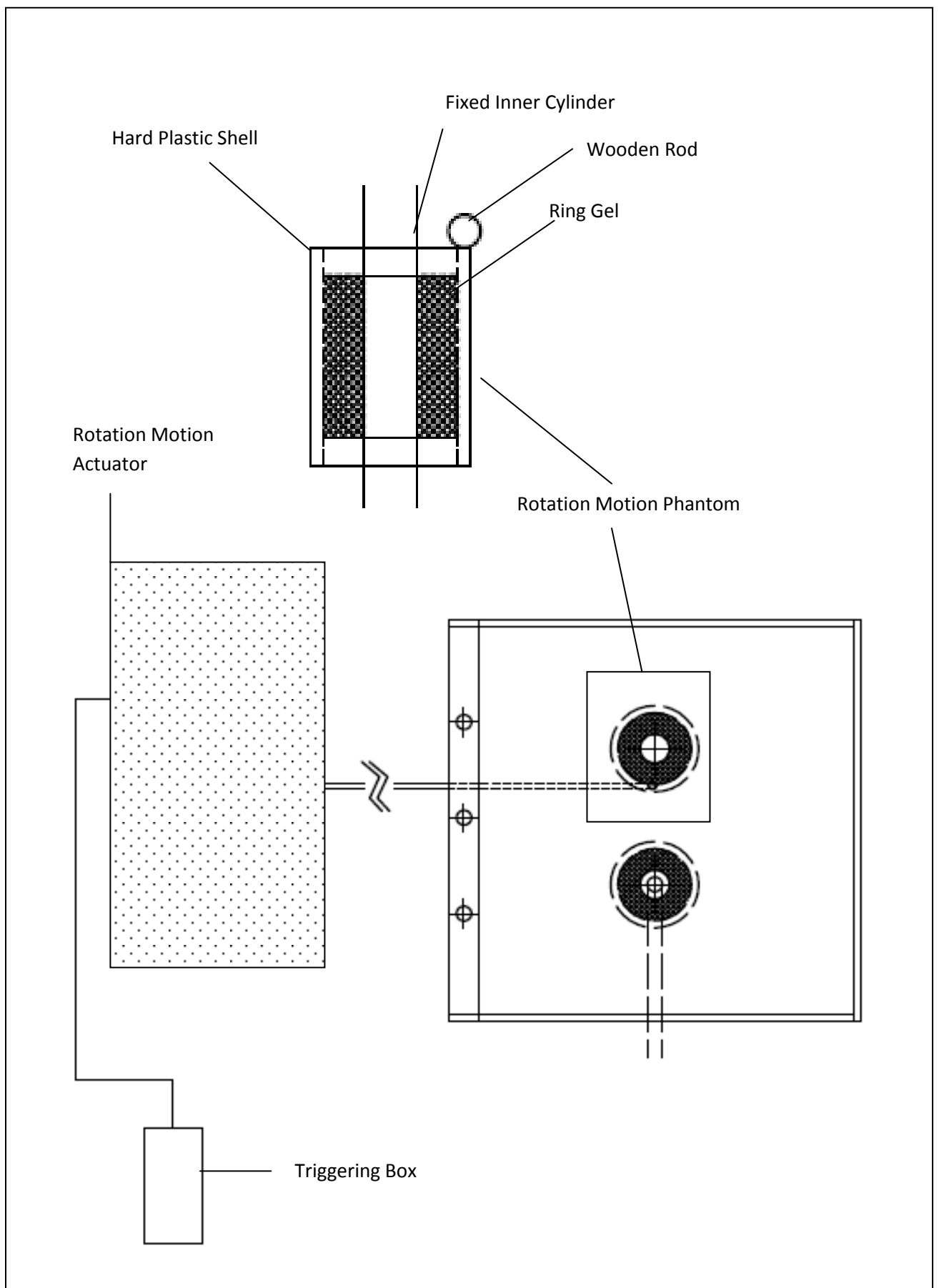


Figure 12. *Elements of rotation motion phantom*

CHAPTER IV

LEFT VENTRICLE WALL THICKENING MOTION PHANTOM

4.1 Design and Construction of the Left Ventricle Wall Thickening Motion Phantom

The wall motion phantom was pneumatic, driven by a custom non-ferromagnetic pump which cyclically filled and emptied a latex balloon within the phantom. The latex balloon stretched out inside the stationary rigid polycarbonate cylinder and both were concentric. The space between the balloon and the cylinder contains a ring of gel which represents the LV myocardium. The outer diameter of the gel, which adhered to the outer cylinder was 2.5 inches. The shell thickness was 0.25 inches. The inner diameter of the gel was 0.7 inch and had the balloon inside. The thickness of the gel was 0.9 inches. The cylindrical balloon was filled with air cyclically to cause uniform deformation through the gel. The Figure 13 shows the wall thickening motion phantom with dimensions.

Three iterations of the pump used to cyclically fill the balloon with air have been built. These pumps and corresponding results are presented in the remainder of this chapter.

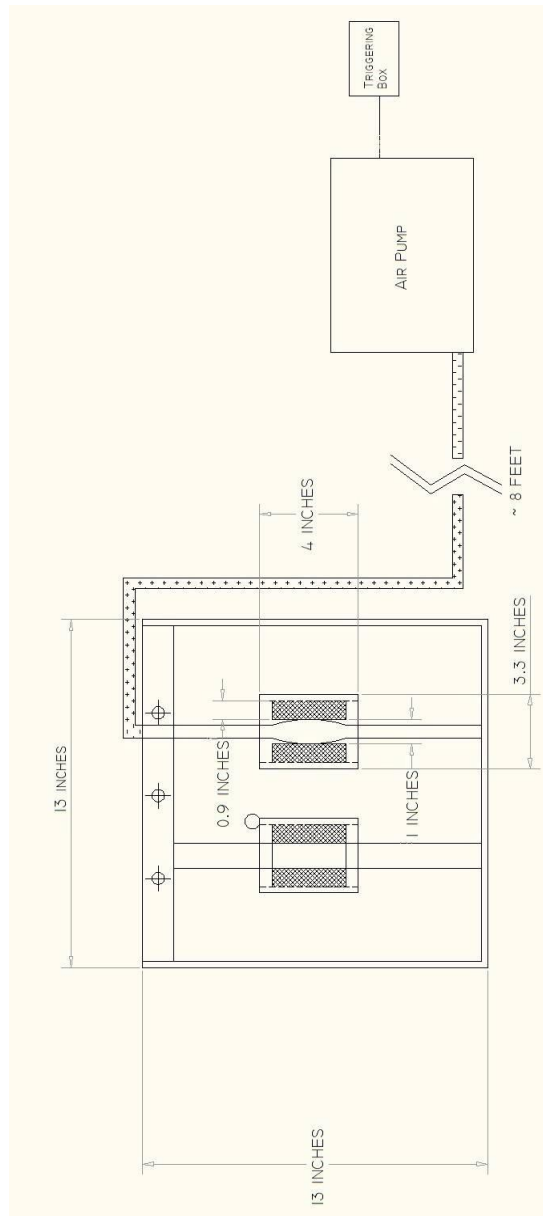


Figure 13. *The wall thickening motion phantom with dimensions.*

The gel was first poured into phantom while the phantom had a mold inside of it to ensure that gel would form in a perfect ring shape. Once the gel was formed into high viscous form, the mold was taken out of the phantom and the latex balloon was placed concentrically to the wall motion phantom. The latex balloon was attached to plastic tubing from the both end. One of the plastic tubing was connected to the pump while the other was mounted into the enclosure and had dead end.

4.2 Wall Thickening Motion Phantom with Pump Version 1.0

Air pump version 1.0 was designed in a simplistic manner. A cylindrical plastic plate, which was connected to camshaft, was placed into the plastic tubing. The balloon was inflated by moving the camshaft into the piston to result in air pressure. Expansion of the balloon with the air pressure created a thinning within the gel through the cylinder in radial form. Then, camshaft was pulled back to deflate the balloon which resulted in gel to recover to its primary shape itself. The pump 1.0 had scaling on it such as the typical syringes to see and operate how much camshaft was displaced. The three inches displacement resulted in the 77.5% thinning in the wall of the motion phantom. This deformation corresponded to maximum deformation that the phantom could have. The first version of the pump design is shown in the Figure 14.

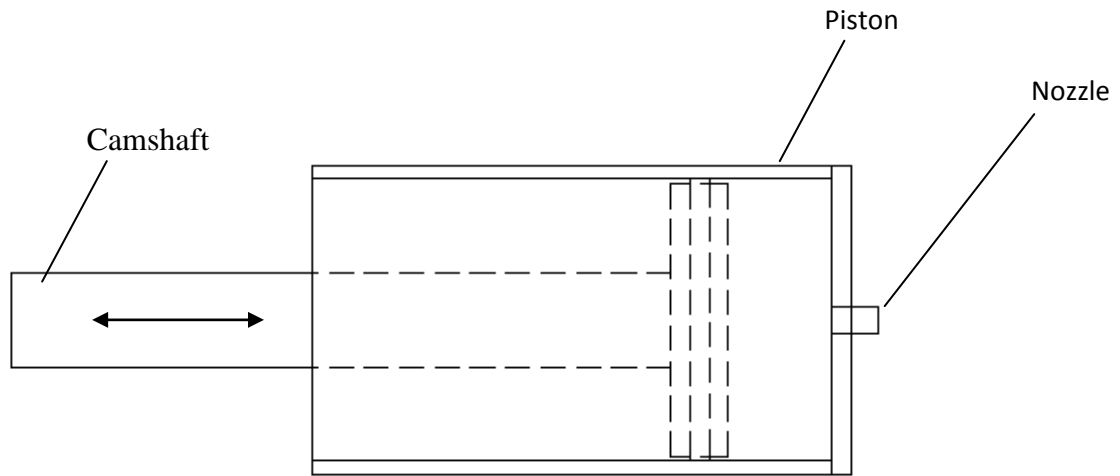


Figure 14. *Air pump 1.0 was operated by moving the camshaft in and out by holding the camshaft with one hand and holding the piston with the other hand.*

4.2.1 Image Acquisition and Results for Pump 1.0

MRI images were obtained with using a Philips Achieva 3.0 T MRI scanner (Philips Healthcare, Highland Heights, OH). Real time cine images of the wall motion phantom were obtained using Air Pump version 1.0 with two different runs. Acquisition parameters were as follows: 2.1 msec repetition time (TR), 0.8 msec echo time (TE), 110 ms temporal resolution, 15° flip angle, turbo factor 40, 130 mm field of view (FOV), 30 heart phases, 64/80r matrix, echo planar imaging factor 1, rectangular FOV 100%, 300 dynamics. The circular local receive coils were used.

Sample images from the wall motion phantom when operated by the air pump version 1.0 are shown in Figure 15.

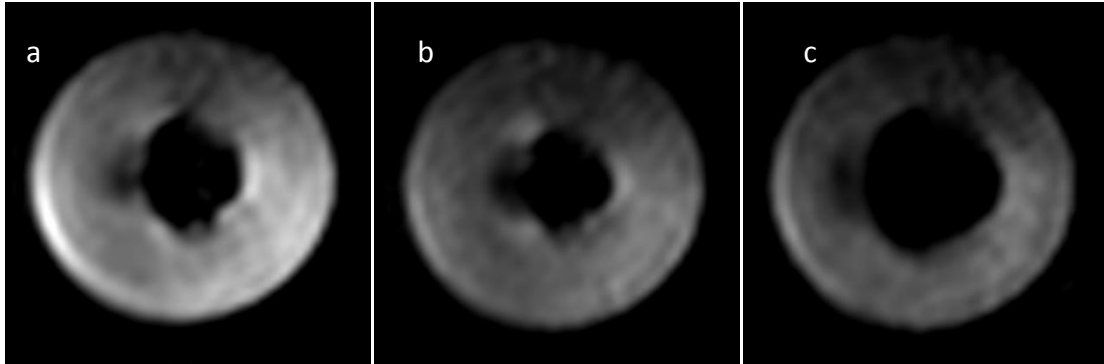


Figure 15. *Wall motion phantom images with Air Pump 1.0 at a) 0 sec, b) minimum cross-sectional area, and c) maximum cross-sectional area.*

The Figure 16 and 17 show the cross-sectional area change with respect to time for wall motion phantom when operated by the air pump version 1.0.

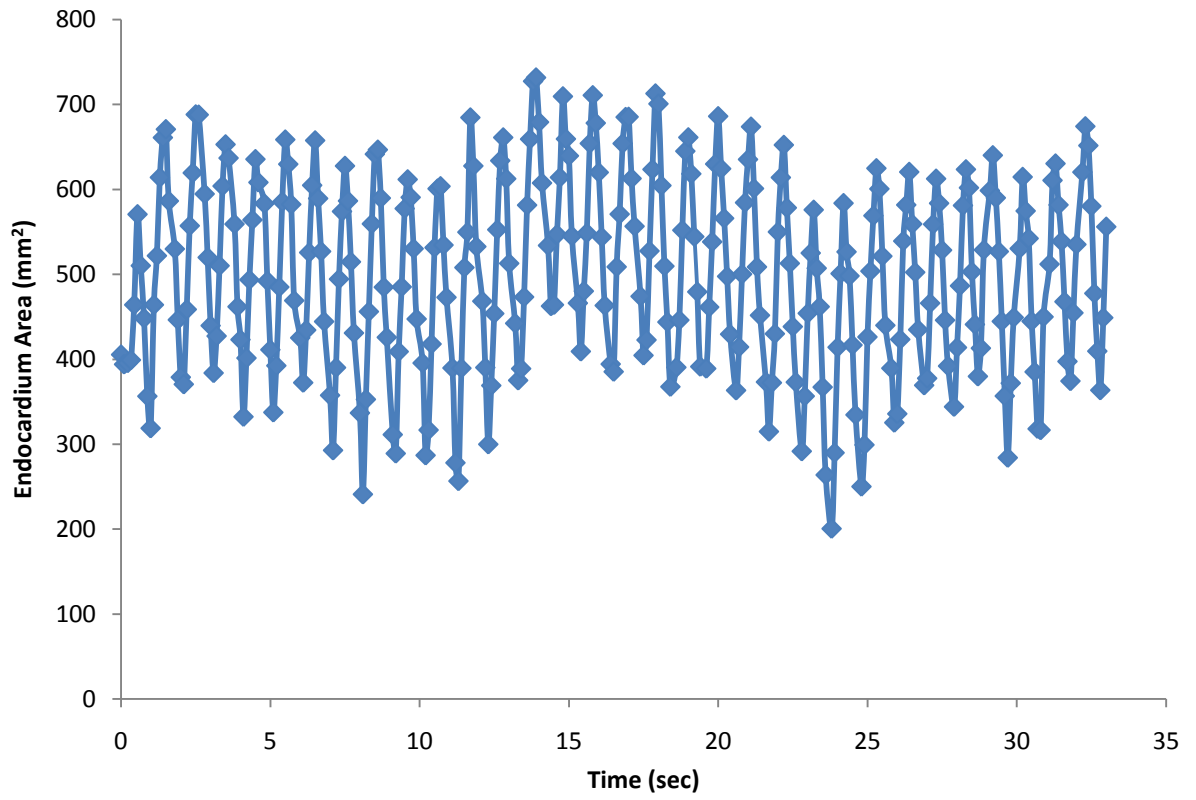


Figure 16. *Cross-sectional area change as a function of time for wall motion phantom operated by the air pump version 1.0 run # 1.*

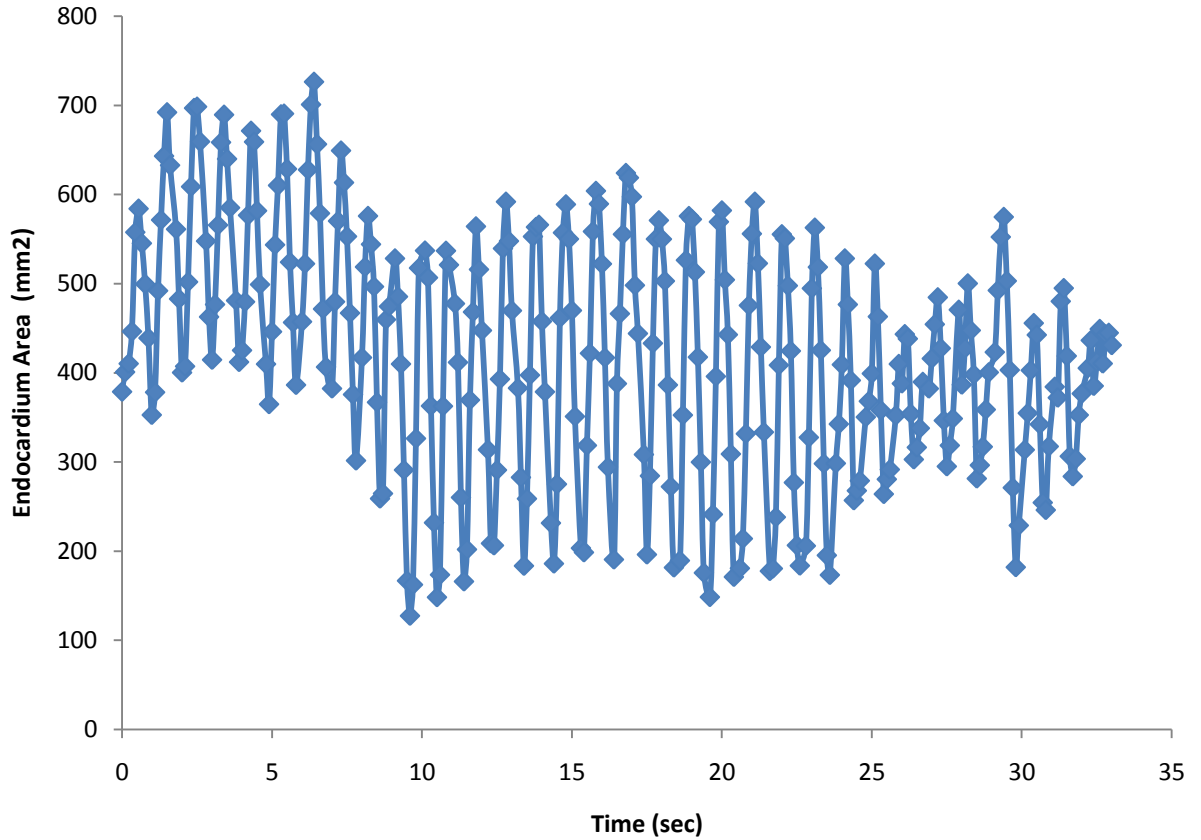


Figure 17. *Cross-sectional area change with the time for wall motion phantom operated by the air pump version 1.0 run # 2.*

The T1 value of the gel was determined using a Look-Locker pulse sequence to be 728 milliseconds. Acquisition parameters were as follows: 8 msec repetition time (TR), 3.2 msec echo time (TE), 8 ms temporal resolution, 7° flip angle, turbo factor 9, 150 mm field of view (FOV), 37 heart phases, 98/112r matrix, echo planar imaging factor 3, rectangular FOV 100%, PrePulse T1 150 msec. Same circular local receive coils were used.

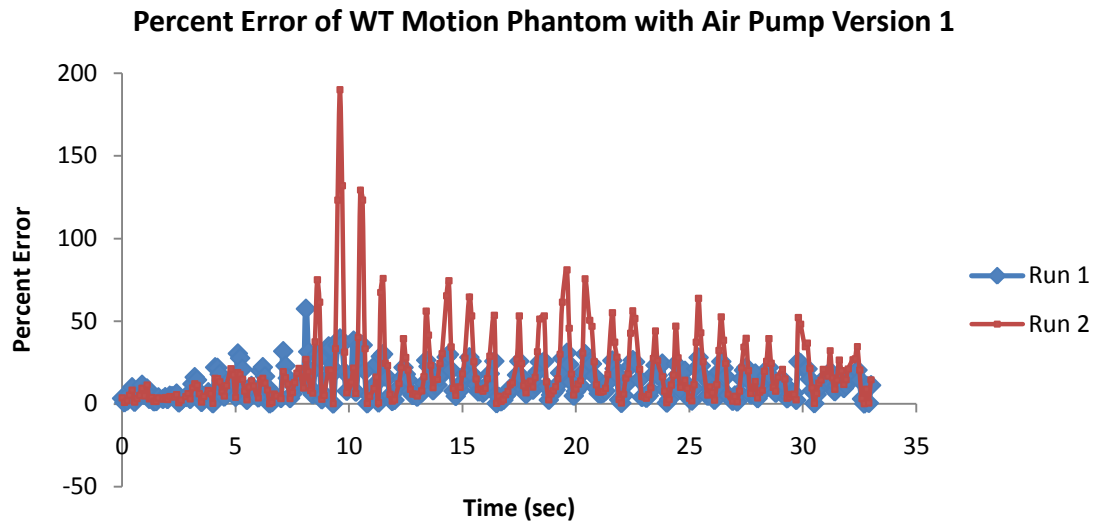


Figure 18. *Percent error due to variability between different runs of wall motion phantom operated by the air pump version 1.0.*

4.2.2 Discussion

From the Figures 16 and 17, the change in the modeled endocardium area with respect to time is seen. Each maximum and minimum area of the inner wall of the gel in the graphs represents the myocardium wall motion of the left ventricle at diastole and systole. The variations in the upper and lower limits of the area change and inconstant frequency of area change shows that the reproducibility of the motion is insufficient with up to 150% variability as shown in Figure 18. Also, the triangle waveform shape of the area change in the graphs is non-physiologic. Therefore, design and build of a piston air pump, which ensures the constancy and physiological area change, was the next aim of the study.

In addition to mechanic operation deficiency, a trigger pulse related to the cyclic motion of the phantom and similar to heart beat was also another missing component of the motion phantom. The mechanism for the synchronization of the data acquisition with the phantom motion was developed for the next version of the air pump.

4.3 Wall Thickening Motion Phantom with Pump 2.0

Because of the problems encountered with the first pump design, a modified pump (version 2.0) was designed and built.

Firstly, for the ease of operation of the air pump, a T-handle was mounted onto the camshaft. The body of the pump was attached to a supportive structure to increase stability during operation. Then, the maximum wall thickening motion of the gel was attained by mounting a circular plate cap on the open end of piston to stop the camshaft shift every time at the same location (shown in Figure 19). This cap had a hole at the center of it for the camshaft of the piston. On this camshaft, three different holes were created to attach pin to enable three different settings of volumes. Different pin location resulted in different amount of thinning in the gel of the wall motion phantom. The amounts of thinning in the gel with respect to three different settings were 78%, 52% and 26%.

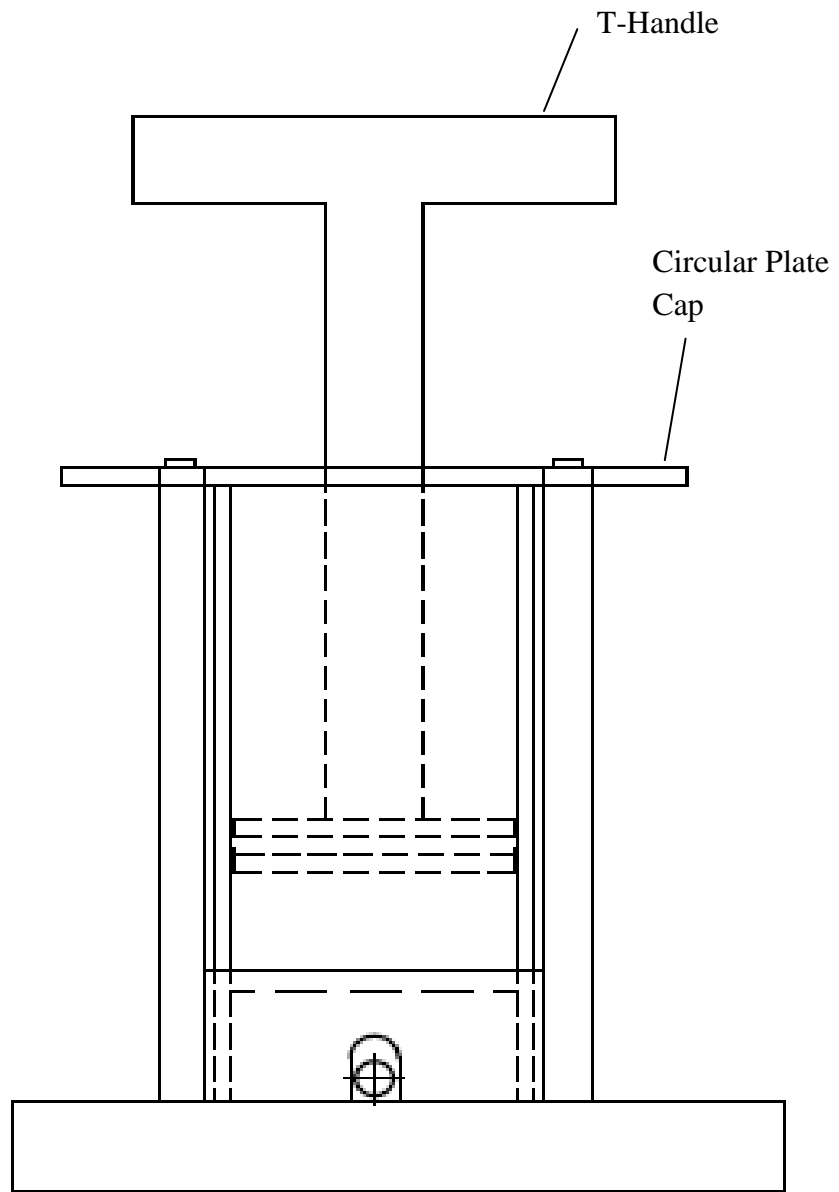


Figure 19. *Air pump 2.0 front view.*

The top view of the air pump is shown in Figure 19.

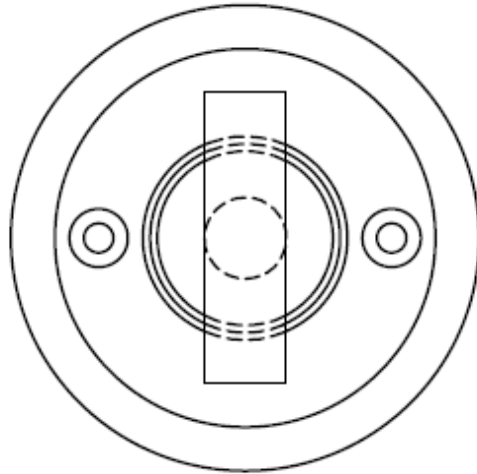


Figure 20. *Air pump 2.0 top view.*

Another important modification was the ability to attach the triggering switch into pump to create a triggering signal for the synchronization of movement with the MRI scanner (Figure 21). This switch was push on type and mounted into the rod of the cylinder. When the rod was pushed into the piston to pump the air, the switch was turned on by touching the cap of the piston. Thus, the trigger signal was created when the maximum thinning was achieved in the gel of the phantom.

The trigger switch attached to the pump was not completely MR-compatible. However, it was very small and mounted into the body of the pump. It did not have enough metal to project through the scanner. The switch was calibrated to be pressed when the piston was at lowest point. Multiple levels were possible to trigger at different amounts of contraction.

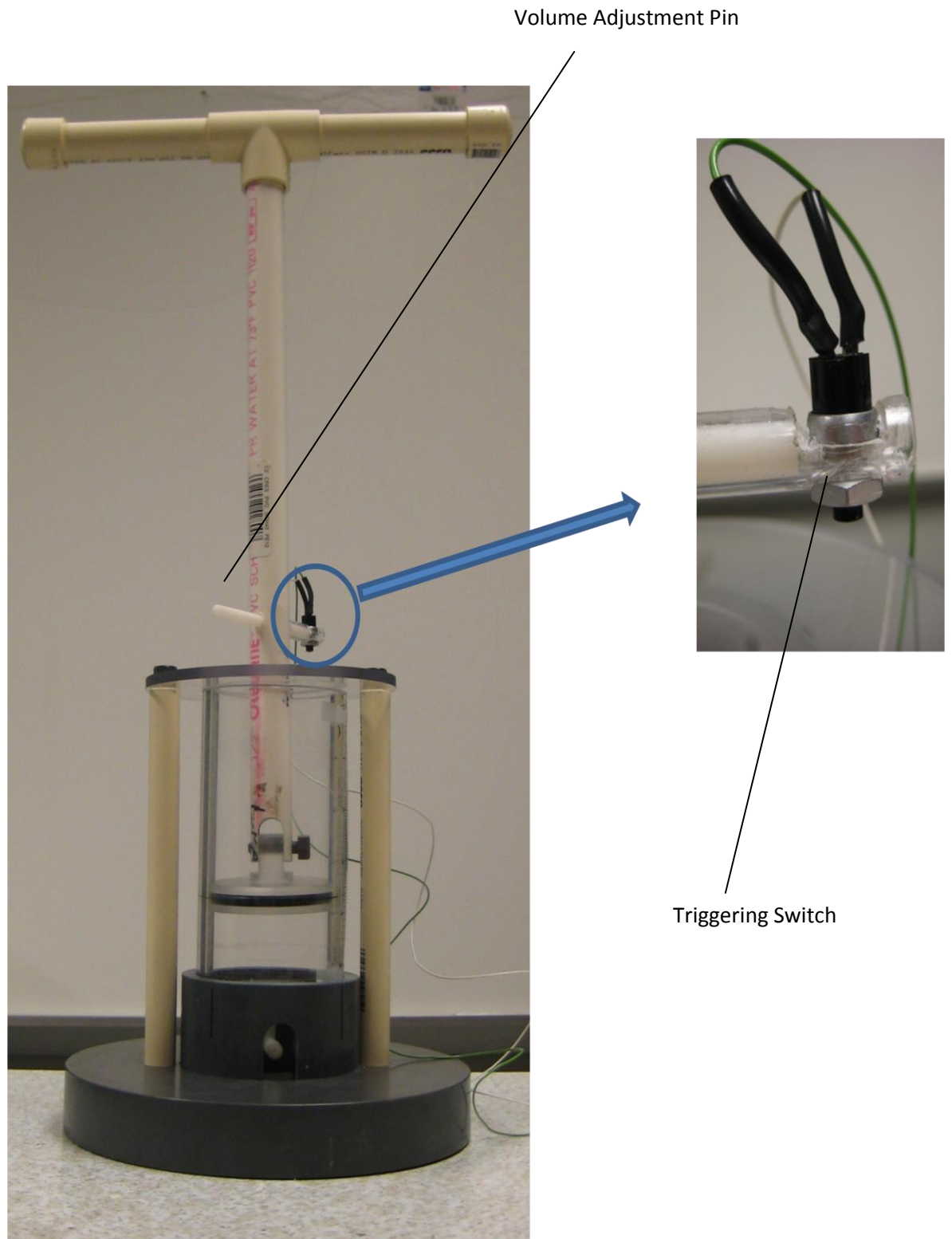


Figure 21. *Air Piston Pump 2.0 with attached triggering switch.*

The elements of wall motion phantom experimental setup are shown in the Figure 22. On the right side of the common enclosure is a wall thickening motion phantom which is driven by Air Piston Pump 2.0 and movement of the phantom is synchronized with the attached triggering circuit into the pump.

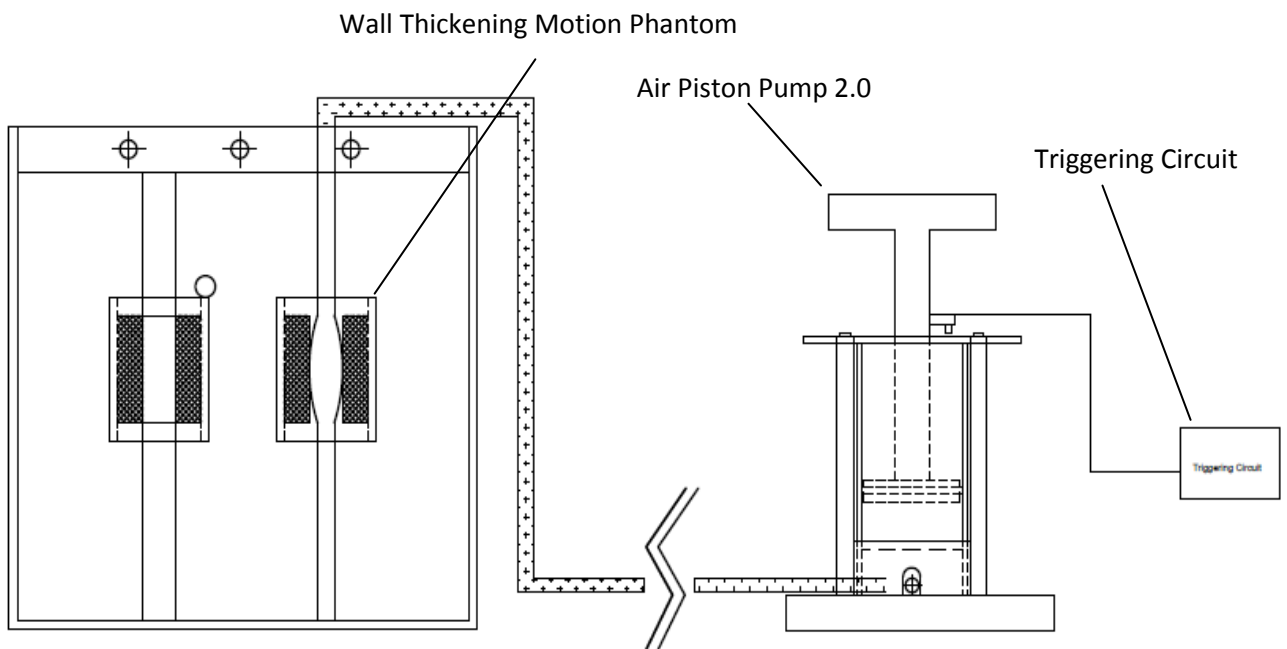


Figure 22. *The Air Piston Pump 2.0 is shown with the attached triggering box and phantom.*

4.3.1 Image Acquisition and Results for Pump 2.0

Triggered Cine images of the wall motion phantom were obtained by using Air Pump version 2.0. Acquisition parameters were as follows: 3.8 msec repetition time (TR),

1.6 msec echo time (TE), 50 ms temporal resolution, 15° flip angle, turbo factor 19, 150 mm field of view (FOV), 30 heart phases, 89/128r matrix, echo planar imaging factor 1, rectangular FOV 100%. The circular local receive coils were used. The cine image analysis of the wall motion is shown in Figure 23.

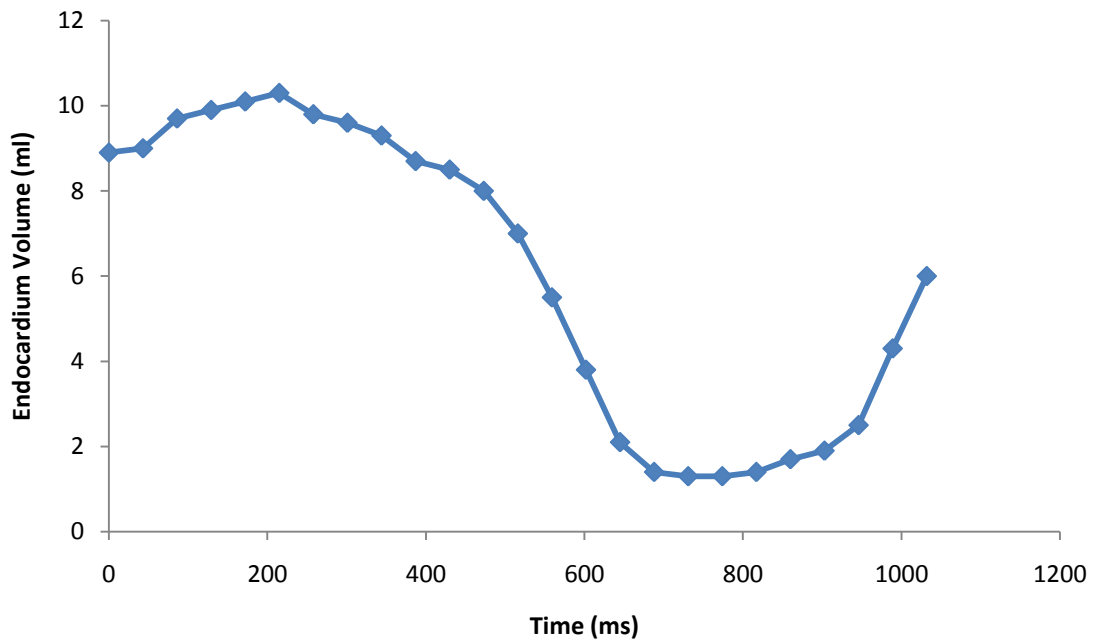


Figure 23. *Change of the cross-sectional area within the wall of the gel with respect to the time for wall motion phantom when operated by the air pump version 2.0.*

Additional four different series of wall motion experiments by applying same amount of contraction were run to validate the reproducibility of the wall motion phantom. The cine images of four different scanning results for the same amount of contraction (78% thinning) experiments of wall motion phantom were analyzed by using

Philips dedicated cardiac analysis tool. Runs had variability up to 60% as shown in Figure 25. Also, results are shown in Figure 24 and 26.

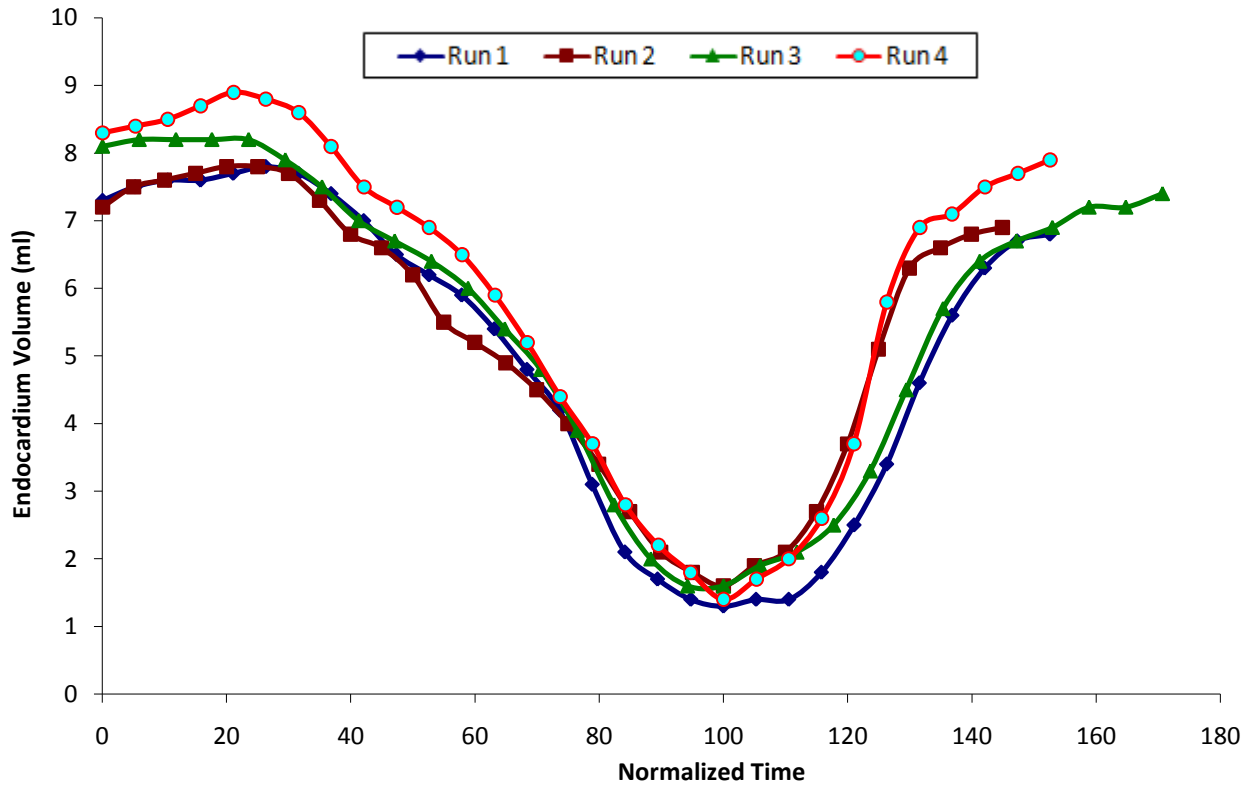


Figure 24. The change in the volume of the endocardium in four different experimental run of the wall motion phantom when operated by the air pump version 2.0.

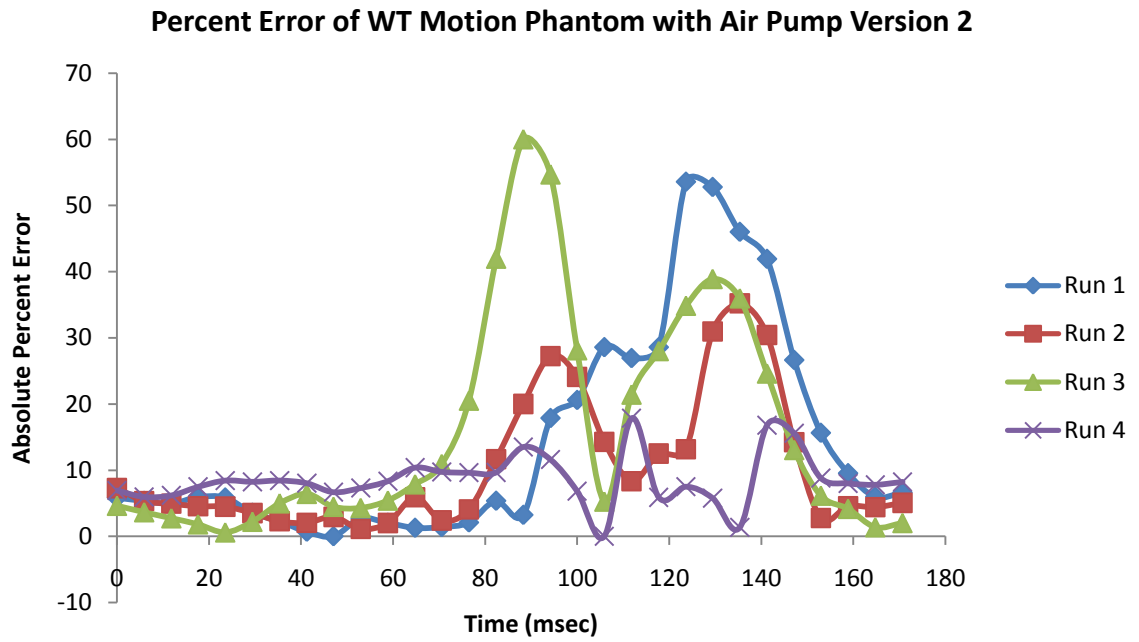


Figure 25. *Percent error due to variability between different runs for wall motion phantom operated by the air pump version 2.0.*

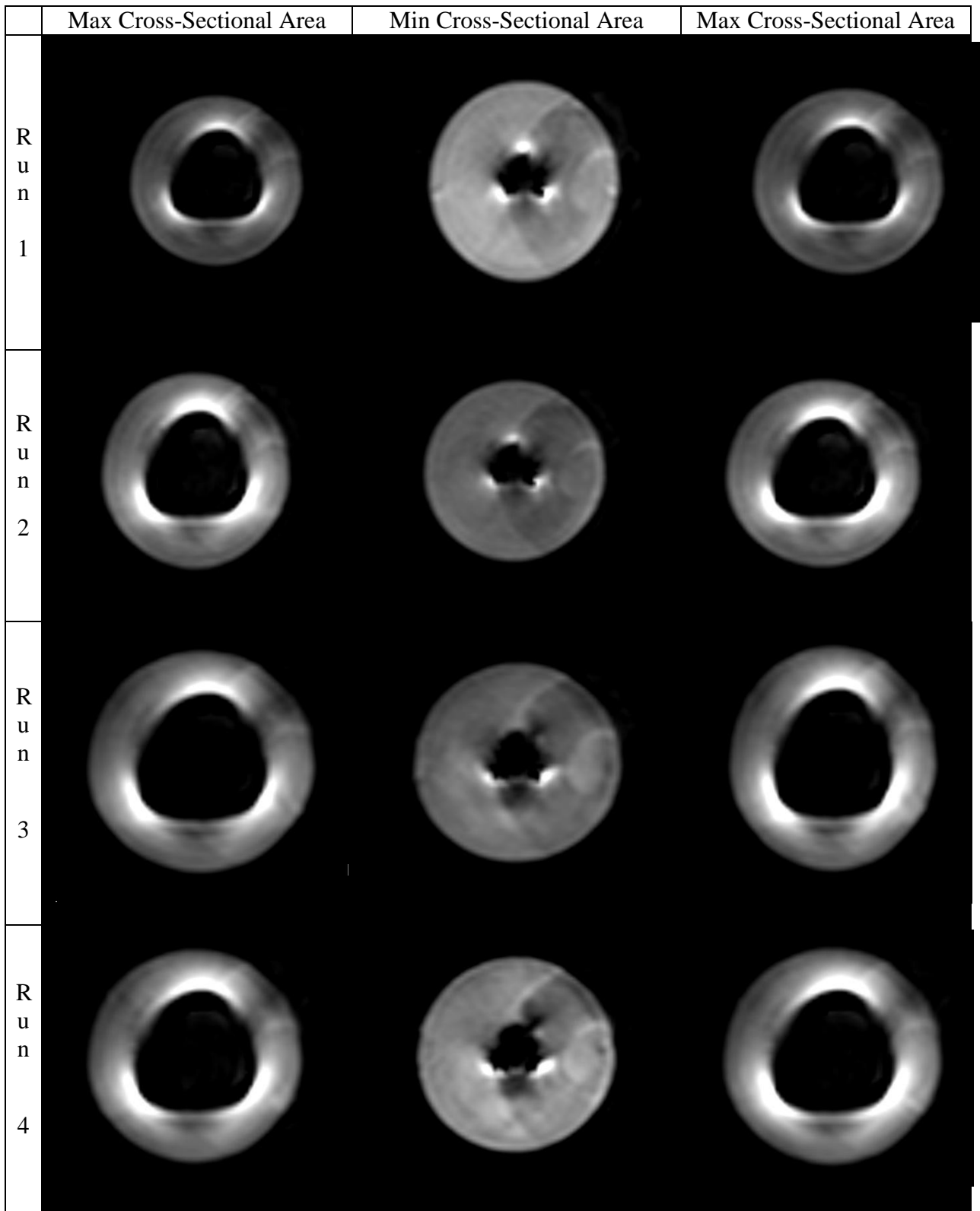


Figure 26. Set of images for wall motion phantom from different runs operated by the air pump version 2.0 for different runs at maximum, minimum and maximum cross-

sectional areas.

In the grid tagged cine images of the wall motion phantom, it was not possible to follow the deformation of the grid patterns from the images. The grid tagged cine images are shown in Figure 27.

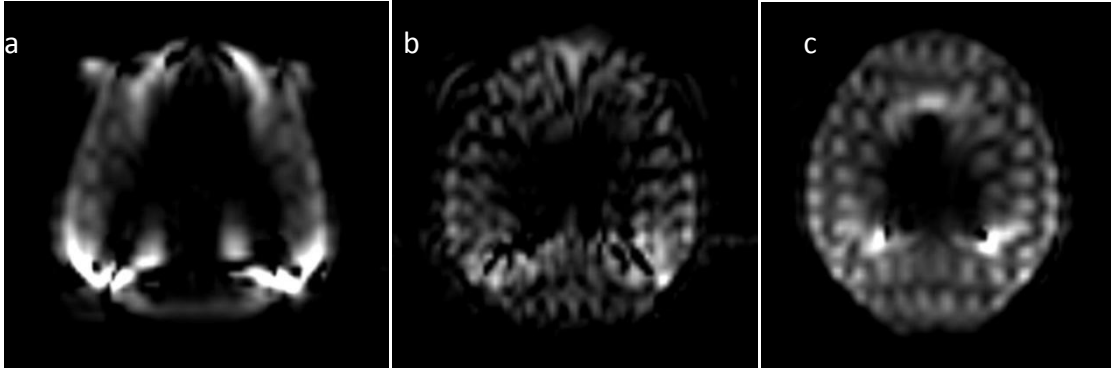


Figure 27. *Set of grid tagged cine images from wall motion phantom run operated by the air pump version 2.0 at a) diastole, b) systole, and c) diastole.*

4.3.2 Discussion

From the cine images, it was observed that up to 77.5% contraction in the phantom walls has been achieved and different runs with the same deformation settings concluded the reproducibility. The Figure 24 also shows four different runs and their consistent deformation data with respect to each other.

However, change in direction at end points of pump linear motion resulted in inconsistent frequency with up to 50% variability between cycles and inconsistent velocity through the cycle. These defects resulted in untraceable tagging in the images as

shown in the Figure 27. According to that problem, next step in the study to design a mechanism for the air pump 2.0 to operate it with the same frequency of motion.

4.4 Wall Thickening Motion Phantom with Pump 3.0

Due to insufficient constant frequency of operation with the air pump 2.0, an integrated actuator was designed and installed into the air pump 2.0 and air pump 3.0 was created.

Previously, air pump version 2.0 functioned in a non-continuous form. The pump was driven by pulling and pushing the piston rod. The transitions of the moving directions of the piston rod caused variations in the pumping frequency. It was hard for an individual to operate the pump in the same frequency within the existence of the non-continuous act. By the integrated actuator, continuous move of the piston rod was achieved. The air pump 3.0 also had three different volume settings to create different level of wall thickening motion in the phantom. These volumes caused the same amount of wall thinning as before: 78%, 52%, and 26%. The picture of the air pump 3.0 is shown in Figure 28.



Figure 28. *Air pump 3.0*

4.4.1 Image Acquisition and Results for Pump 3.0

With Air pump 3.0, triggered cine images of the wall thickening motion phantom were obtained by Philips MR Achieve 3.0 T scanner. Acquisition parameters were as follows: 2.5 msec repetition time (TR), 1.3 msec echo time (TE), 15° flip angle, turbo factor 47, 225 mm field of view (FOV), 30 heart phases, 62/96r matrix, echo planar imaging factor 1, rectangular FOV 100%. The circular local receive coils were used.

To validate the reproducibility of the air pump 3.0, four different series of wall motion experiments performed with constant contraction. The variation in the area change with respect to time between the four different experimental runs was decreased to 6% (see Figure 30). Results are shown in Figure 29 and 31.

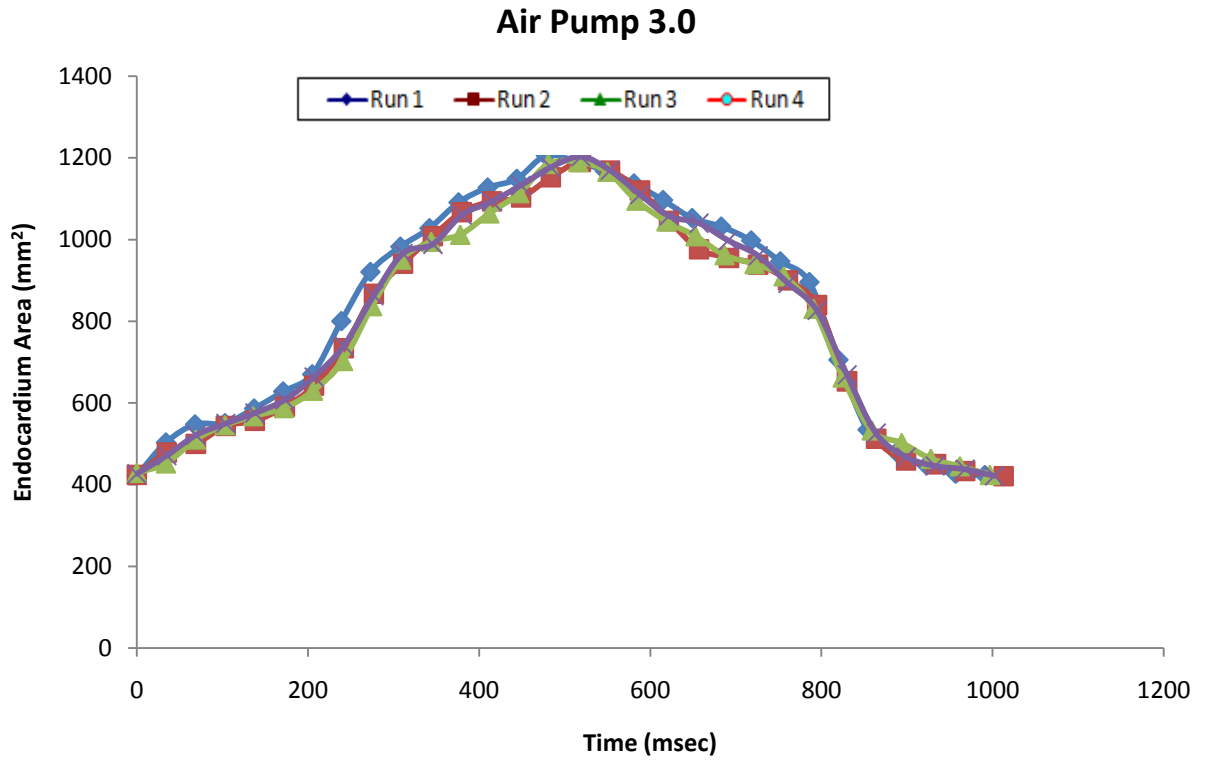


Figure 29. *The change of the cross sectional area in four different experimental run of the wall motion phantom when operated by the air pump version 3.0.*

Percent Error of WT Motion Phantom with Air Pump Version 3

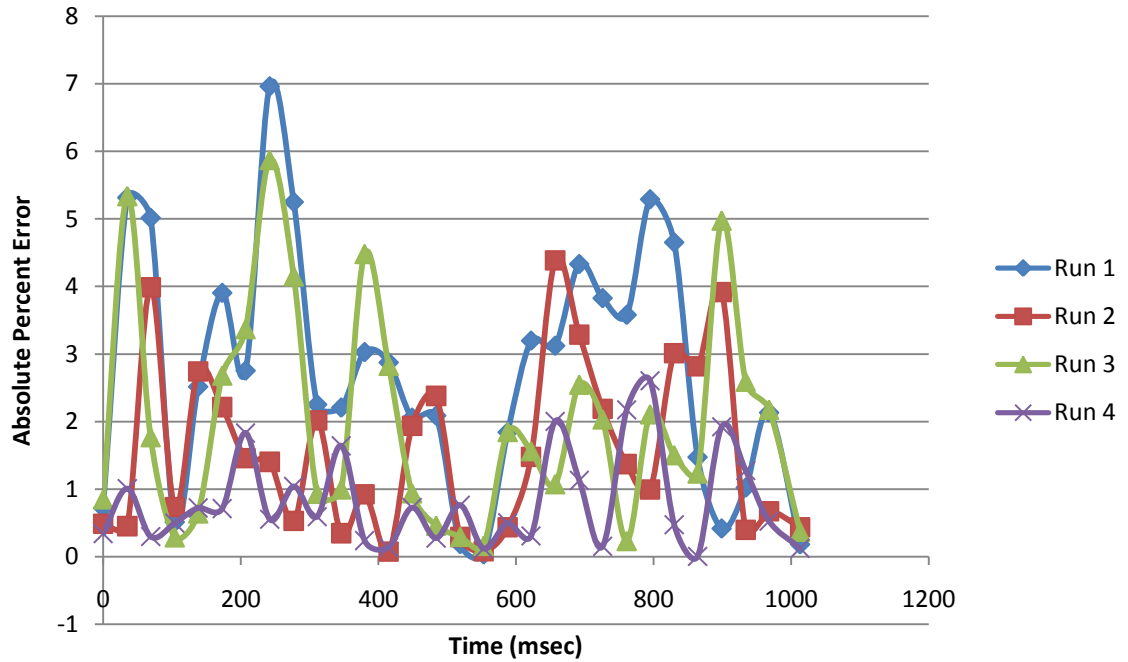


Figure 30. *Percent error due to variability between different runs for wall motion phantom operated by the air pump version 2.0.*

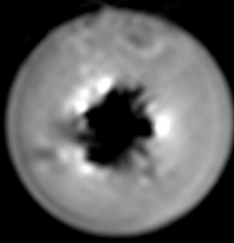
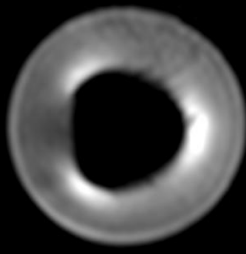
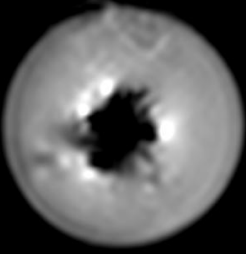
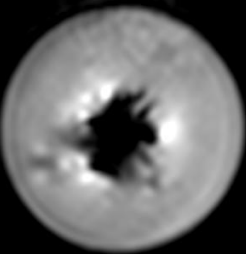
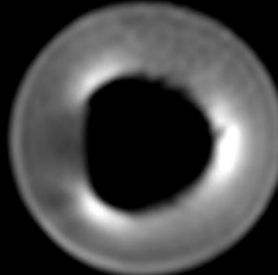
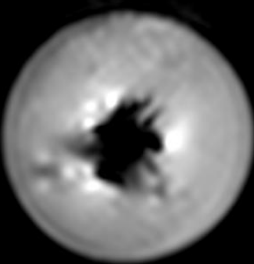
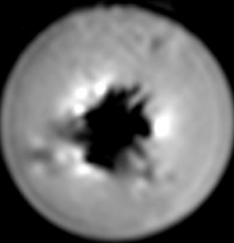
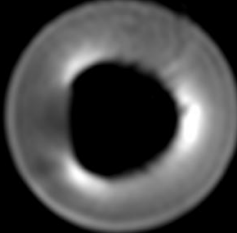
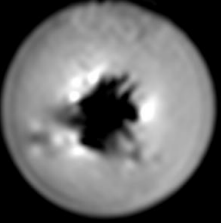
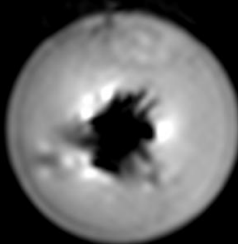
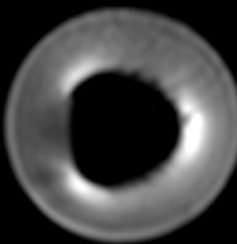
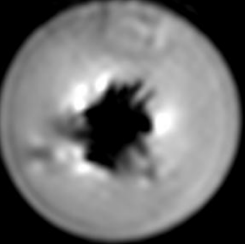
	Min Cross-Sectional Area	Max Cross-Sectional Area	Min Cross-Sectional Area
R u n 1			
R u n 2			
R u n 3			
R u n 4			

Figure 31. Set of images for one beat of wall motion phantom from different 4 runs operated by the air pump version 3.0 at maximum and minimum cross-sectional areas.

Provided constant deformation frequency by operation of air pump 3.0 resulted in efficiently traceable grid patterns within the wall of the wall thickening motion phantom. The grid tagged images of wall motion phantom from one single heart beat are showed in Figure 32.

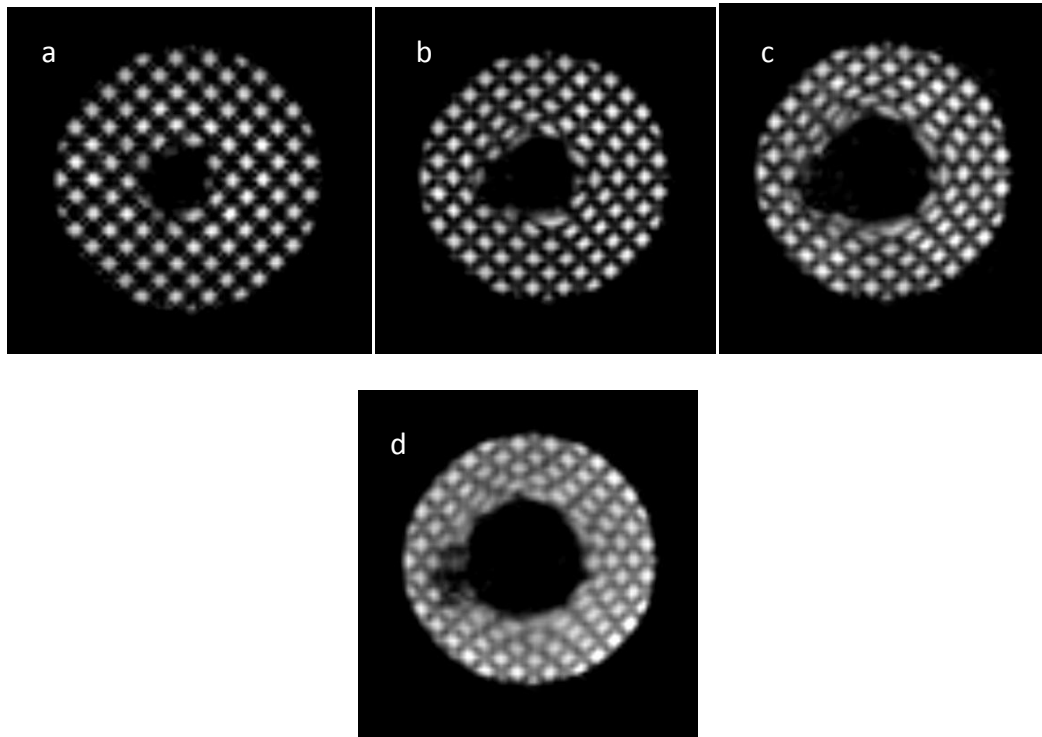


Figure 32. *Set of grid tagged cine images from wall motion phantom run operated by the air pump version 3.0 at a) 300 milliseconds, b) 600 milliseconds, c) 900 milliseconds and d) 1200 milliseconds.*

4.4.2 Discussion

With the integrated continuous actuator of the air pump 3.0, wall thickening motion phantom were able to be used as a dynamic cardiac phantom to acquire MR cine and tagged cine images successfully. The cine images of four different scanning results: with the same amount of contraction (78% thinning) experiments of wall motion phantom were analyzed by using Philips dedicated cardiac analysis tool. The Figure 29 shows four different runs and their area change profile with respect to time. The area change with respect to time was consistent between all runs and it did not require time normalization to match the profiles of the different runs. The variability between different runs was decreased 4% average value. Figure 30 represents the variability between different runs. The grid tagged cine images showed that wall thickening motion phantom was capable of producing accurate tagged images as well. In Figure 24, images from one heart beat in different phases are shown. The tags were significantly traceable within the wall with subjected deformation. LV wall motion phantom was concluded to be an essential tool to fulfill the needs of verification apparatus to test new pulse sequences and tagging techniques in MRI.

CHAPTER V

LEFT VENTRICLE ROTATION MOTION PHANTOM

5.1 Design and Construction of the Left Ventricle Rotation Motion Phantom

The rotation phantom was manually driven by a wooden rod attached to the phantom outer wall which rotates the phantom through a specified angular rotation. The rotation phantom consisted of two concentric cylinders. The outer cylinder which was the shell of the gel had a 3 inch diameter and 0.25 inch thickness. The space between the cylinders was filled with the gel which represents the LV myocardium. The thickness of the gel was 0.9 inches. The inner cylinder which passed through the center of phantom was fixed into the enclosure box and it had 0.875 inch diameter. This ring gel was formed to model the apex of the left ventricle of the heart. Gel deformation was achieved by displacing the attached rod and rotating the outer wall of the phantom while the inner cylinder was fixed. The Figure 33 shows the rotation motion phantom with its dimensions.

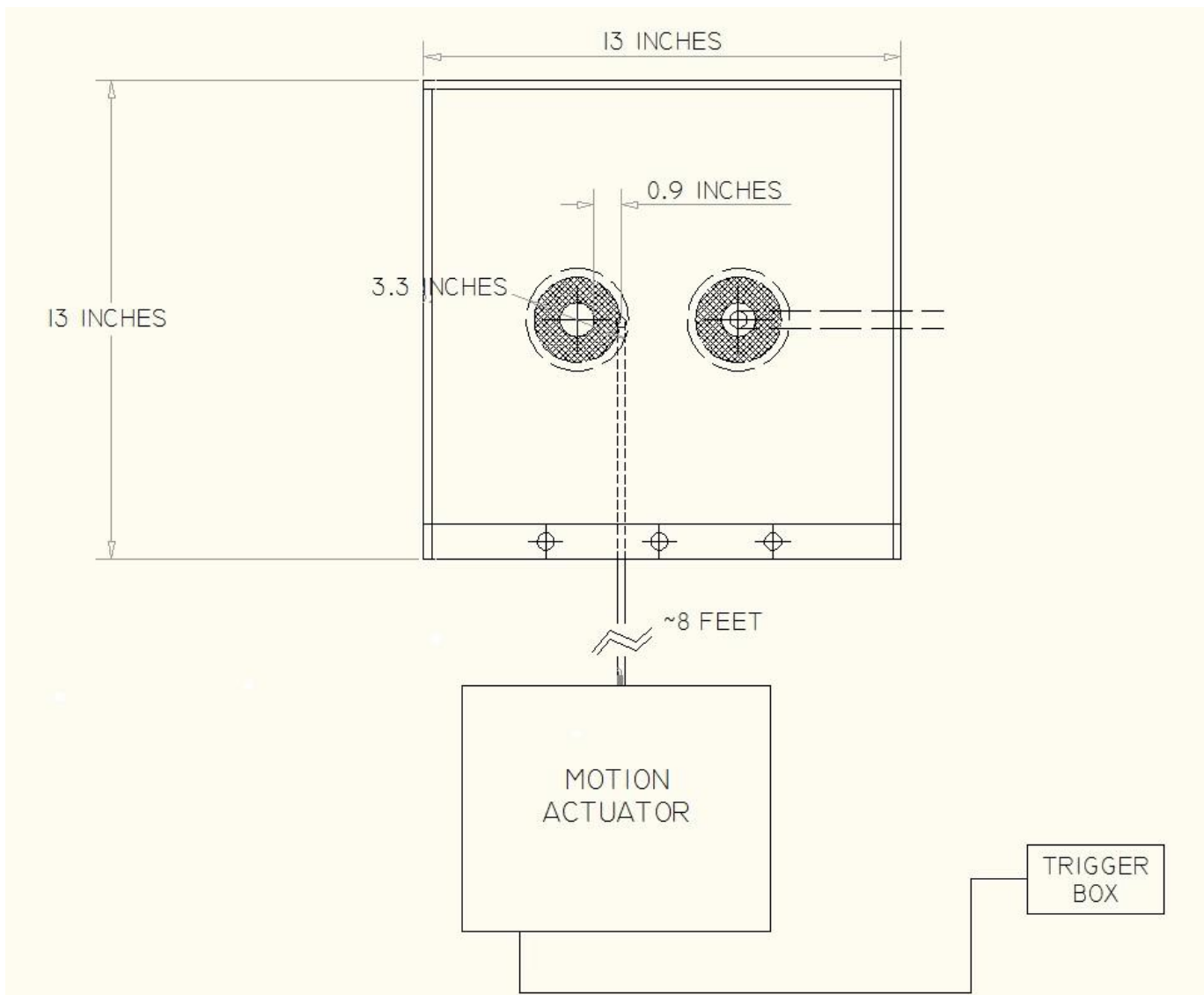


Figure 33. *The rotation motion phantom with its dimensions and experimental setup*

Once the rotation motion phantom was setup into the phantom's enclosure, the gel was poured into the rotation motion phantom. There had been two different versions of motion mechanisms to create the rotation motion of the phantom.

The tagged cine images of the rotation motion phantom were obtained and analyzed using harmonic phase (HARP) analysis software (Diagnosoft, Inc.) which makes analysis of six different cross-sectional regions of the gel such as shown in Figure 34.

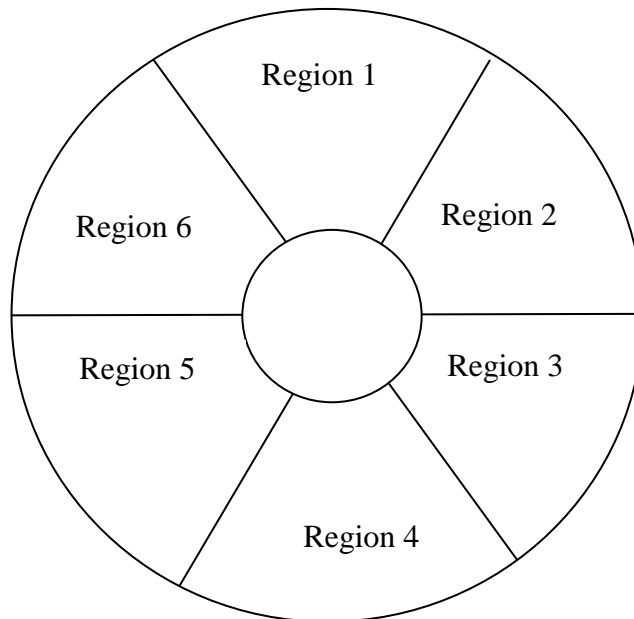


Figure 34. *The distribution of the regions which are used for the analysis of the tagged images by HARP.*

Results for the rotation motion phantom are represented in the remainder of this chapter.

5.2 Wall Thickening Motion Phantom with an Attached Wooden Rod (Version 1.0)

In the first version of the rotation motion mechanism, a wooden rod was attached to the outer cylinder of the rotation motion cylinder as it is shown in Figure 35. By the displacement of the rod backward and forward, the outer diameter of the phantom was rotated and the rotation motion was created to deform the gel.

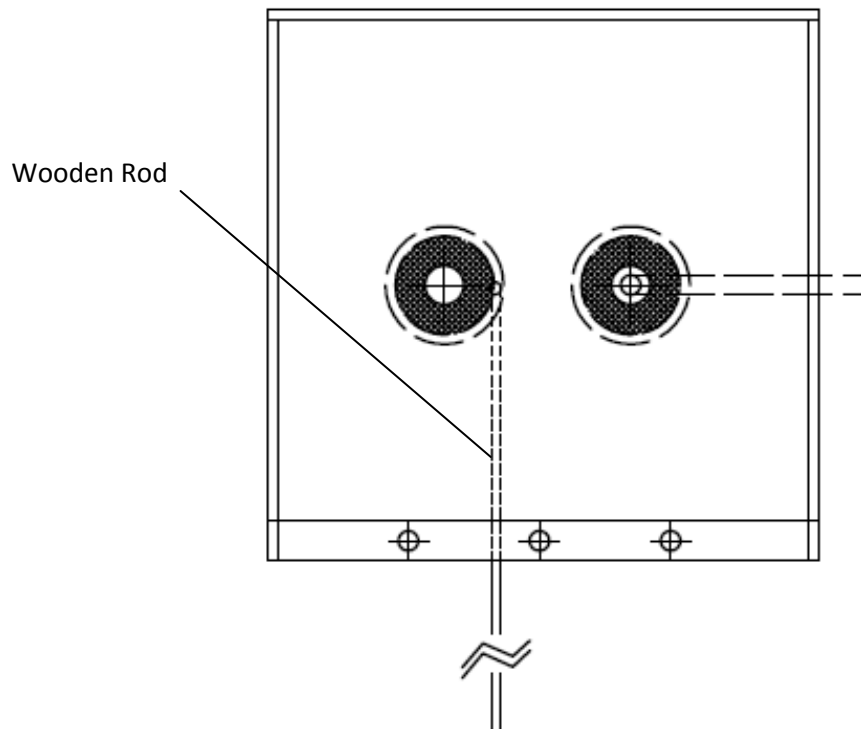


Figure 35. *The wall thickening motion phantom version 1.0*

5.2.1 Image Acquisition and Results for Rotation Motion 1.0

Tagged cine images of the rotation motion phantom were obtained by using rotation motion mechanism 1.0 for 20° rotation. Acquisition parameters were as follows: 8.9 msec repetition time (TR), 4.6 msec echo time (TE), 67 ms temporal resolution, 10^0

flip angle, turbo factor 9, 150 mm field of view (FOV), 16 heart phases, 97/128r matrix, echo planar imaging factor 3, rectangular FOV 100%. Two circular local receive coils were used. Sets of tagged images were acquired to examine reproducibility.

The analysis result and sample tagged cine images are shown in Figure 36 and 37.

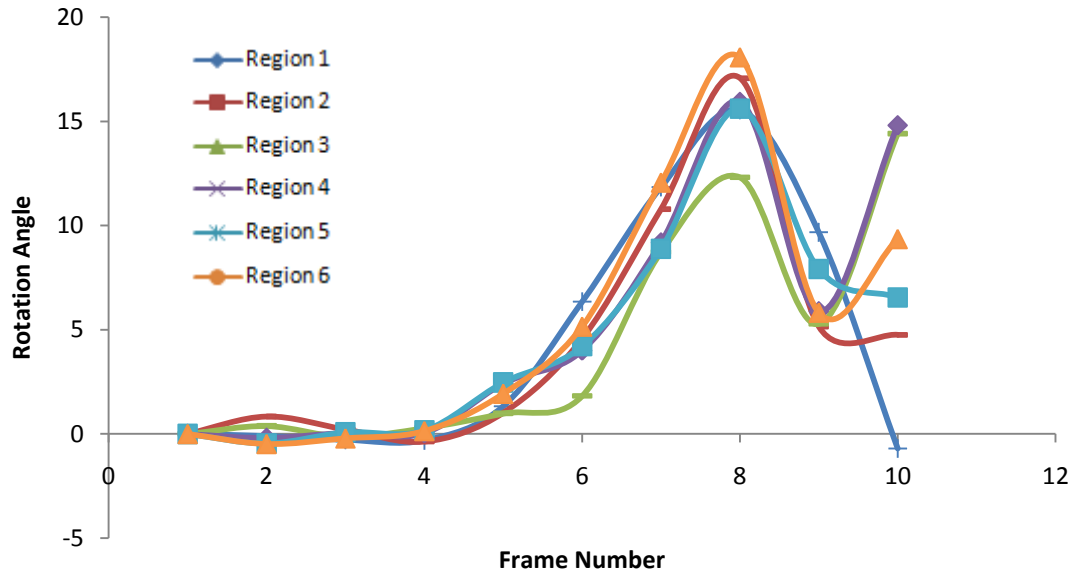


Figure 36. The rotation angle obtained in each frame during the one beat cycle for rotation motion phantom when operated by the motion mechanism 1.0. The tagged image acquisition is shown separately.

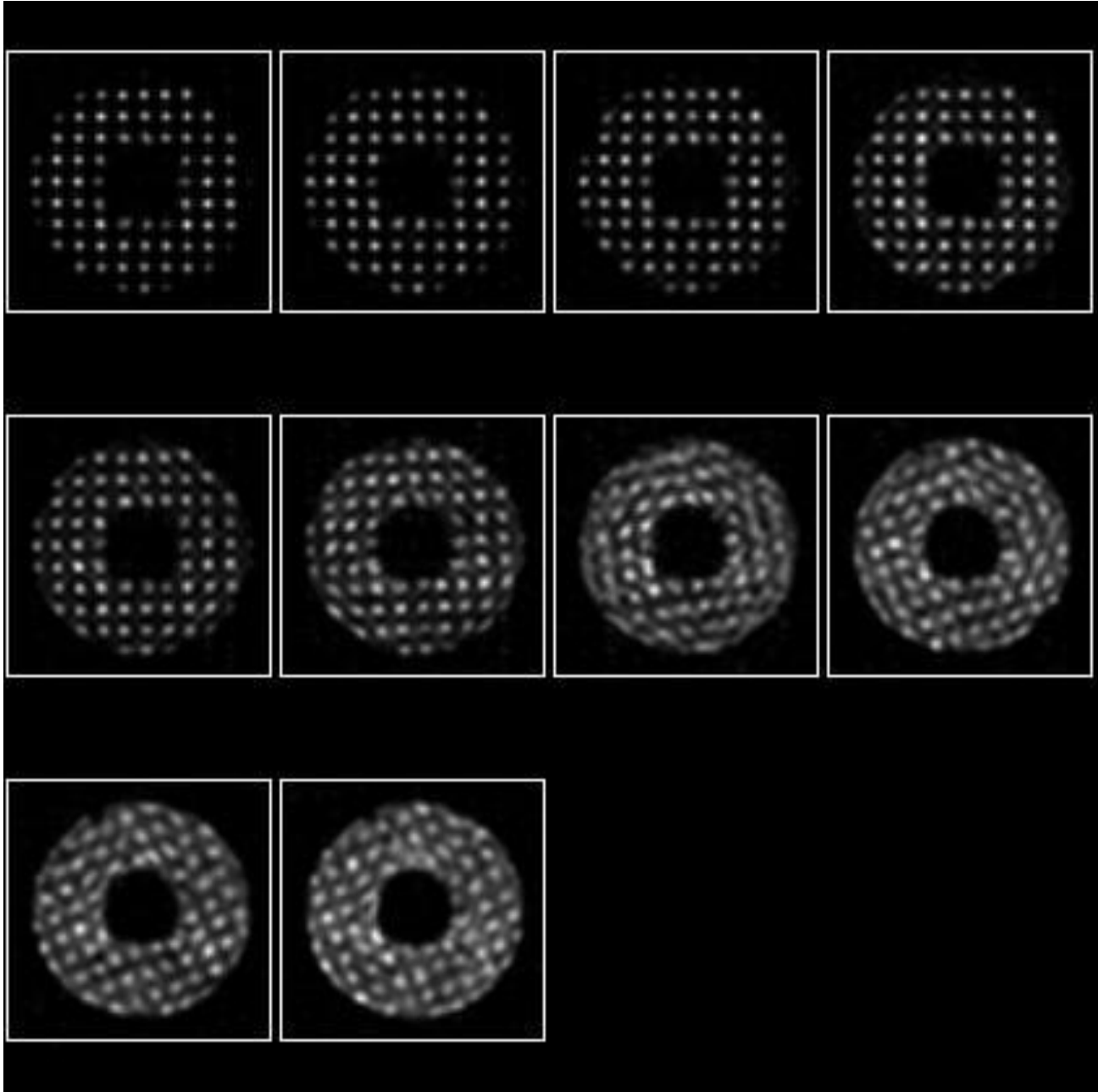


Figure 37. Set of images from rotation motion phantom operated by the motion mechanism 1.0 from diastole to systole of the left ventricle apex in the order of frame number from 1 to 10.

5.2.2 Discussion

One of the problems of the first rotation phantom was the non-uniform motion of the rotation motion of the gel over the entire course of cycles due to bad transition of movement direction from forward to backward or vice versa. In addition to that the triggering was also manual and trigger switch was turned on and off by the operator during the experiment. It was very hard to reproduce the rotation motion over the entire course of cycles with the same speed and frequency. When the tagged cine images in Figure 37 were analyzed, the graph (see Figure 36) for angle of deformation with respect to time was observed, a non-uniform motion of the rotation was seen. Also, the lack of periodic triggering of motion was concluded by the blurred grid patterns in the resulting images. To be able to solve this problem, a new experimental setup for the rotation phantom was created and called rotation motion mechanism version 2.0.

5.3 Wall Thickening Motion Phantom with a Plastic Actuator (Version 2.0)

According to problems that the rotation motion mechanism had, a new continuous motion mechanism (version 2.0) was developed. The plastic actuator in the rotation motion mechanism version 2.0 converted the radial continuous displacement into the linear displacement. This continuous movement of the rod decreased the user dependence motion artifacts such as operating the rotation phantom in different velocities and different rotation angles during the each cycle. In Figure 38 and 39, the design of the plastic actuator is shown. This mechanism was MR-compatible and was easy to operate even during a long period of time.

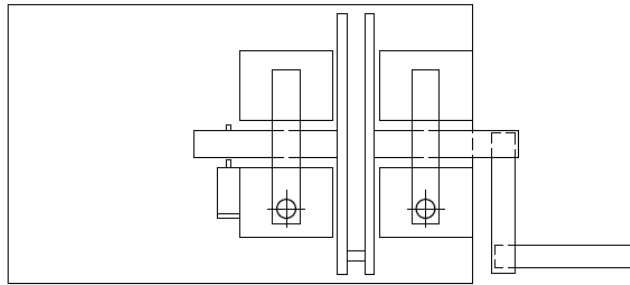


Figure 38. *The top view of the plastic actuator.*

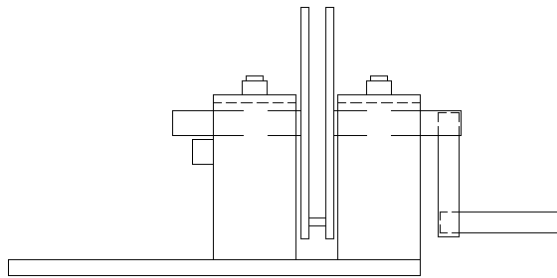
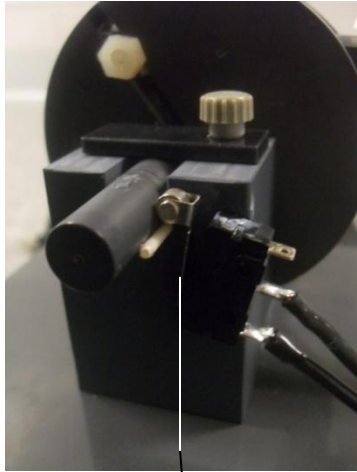
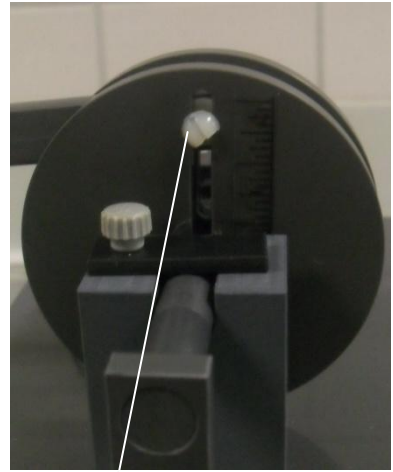


Figure 39. *The front view of the plastic actuator.*

The amount of rotation was adjusted with the crank pin which was used to attach the wooden rod on the actuator (shown in Figure 40). The amount of linear displacement was increased by locating the crank pin far away from the center of the actuator rotation wheel. The version 2.0 of the motion mechanism with the automatic motion trigger was able to reproduce the left ventricular twisting motion in the left ventricular model phantom in different angles ranging from 15° to 45° .



Trigger Switch



Adjustable Crank Pin

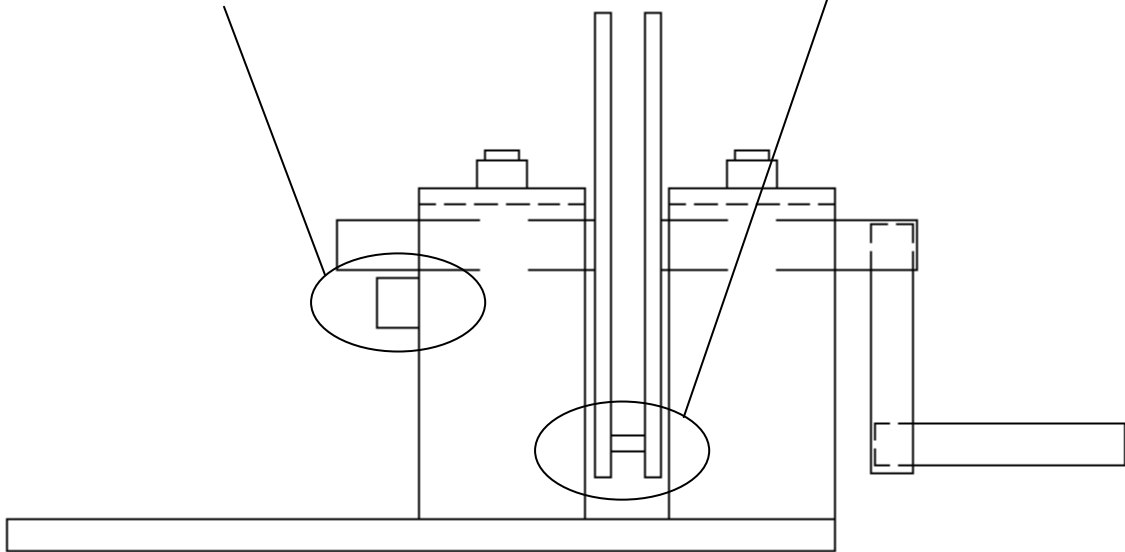


Figure 40. *The front view of the plastic actuator with its components.*

5.3.1 Image Acquisition and Results for Rotation Motion 2.0

Tagged cine images of the rotation motion phantom were obtained by using rotation motion mechanism 2.0, a plastic actuator, during series of three times repeated 15° , 20° , 35° rotations. Acquisition parameters were as follows: 8.9 msec repetition time (TR), 4.6 msec echo time (TE), 67 ms temporal resolution, 10° flip angle, turbo factor 9, 150 mm field of view (FOV), 16 heart phases, 97/128r matrix, echo planar imaging factor 3, rectangular FOV 100%. The circular local receive coils were used. The tagged cine image analysis of the rotation motion was done to validate the rotation angle obtained in the experimental run. The analysis result and sample tagged cine images are shown in following graphs and images.

15° Rotation Deformation Motion

Three different experimental runs which were named as 1, 2, and 3 were performed with adjusting the plastic actuator at 15 degree rotation settings. Images and rotation angle profiles for each frames are shown in following figures.

Tag 1 15 Degree Deformation - 7mm Tagging Line Thickness

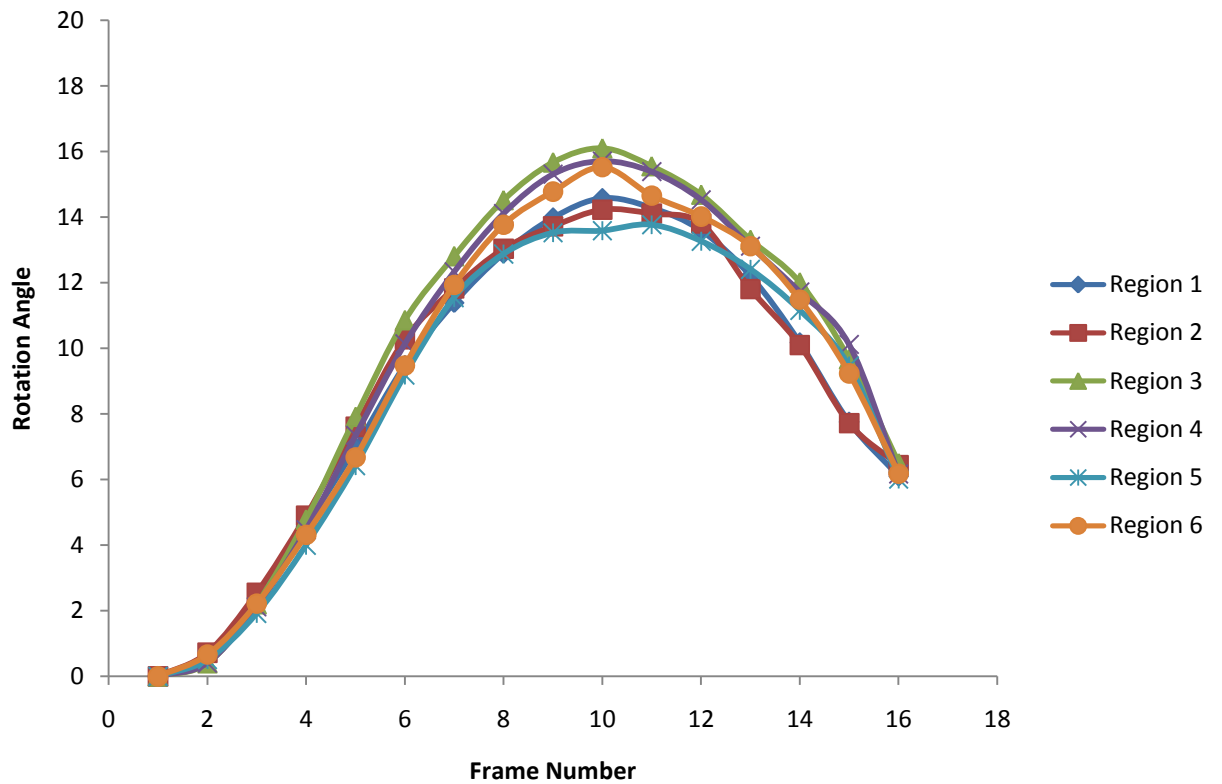


Figure 41. The rotation angle obtained in each frame during the one beat cycle for 15 degree rotation run # 1.

Analysis of the deformation uniformity through the gel is shown in Figure 42.

There was up to 8% non-uniform deformation through the cross sectional area of the gel.

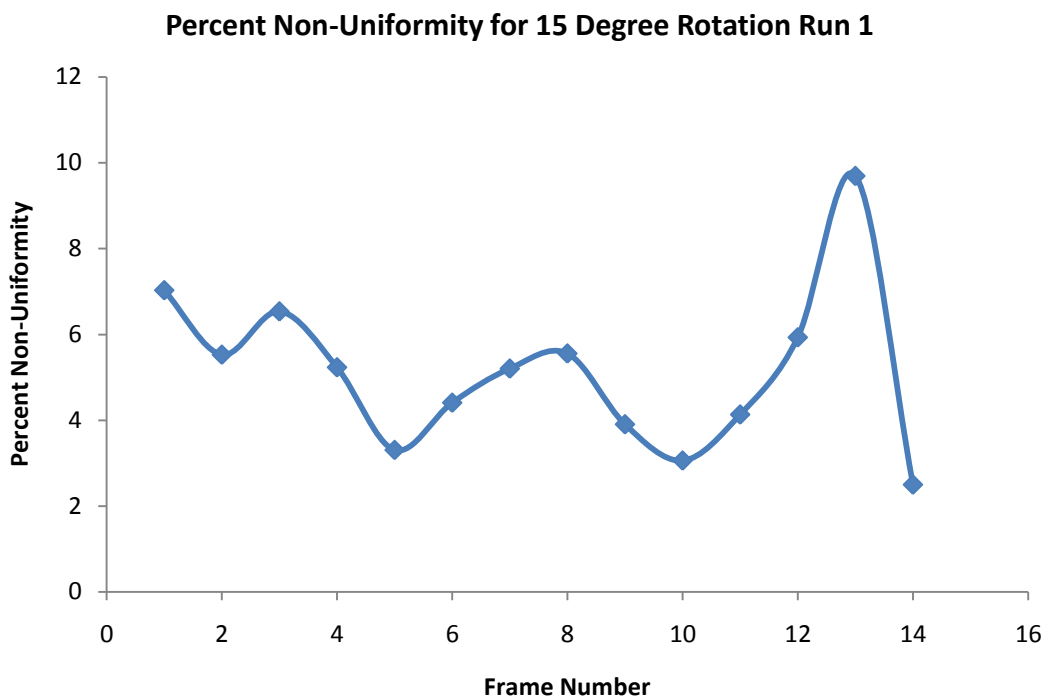


Figure 42. *The non-uniform deformation percentage through the cross section of the gel for 15 degree rotation run 1.*

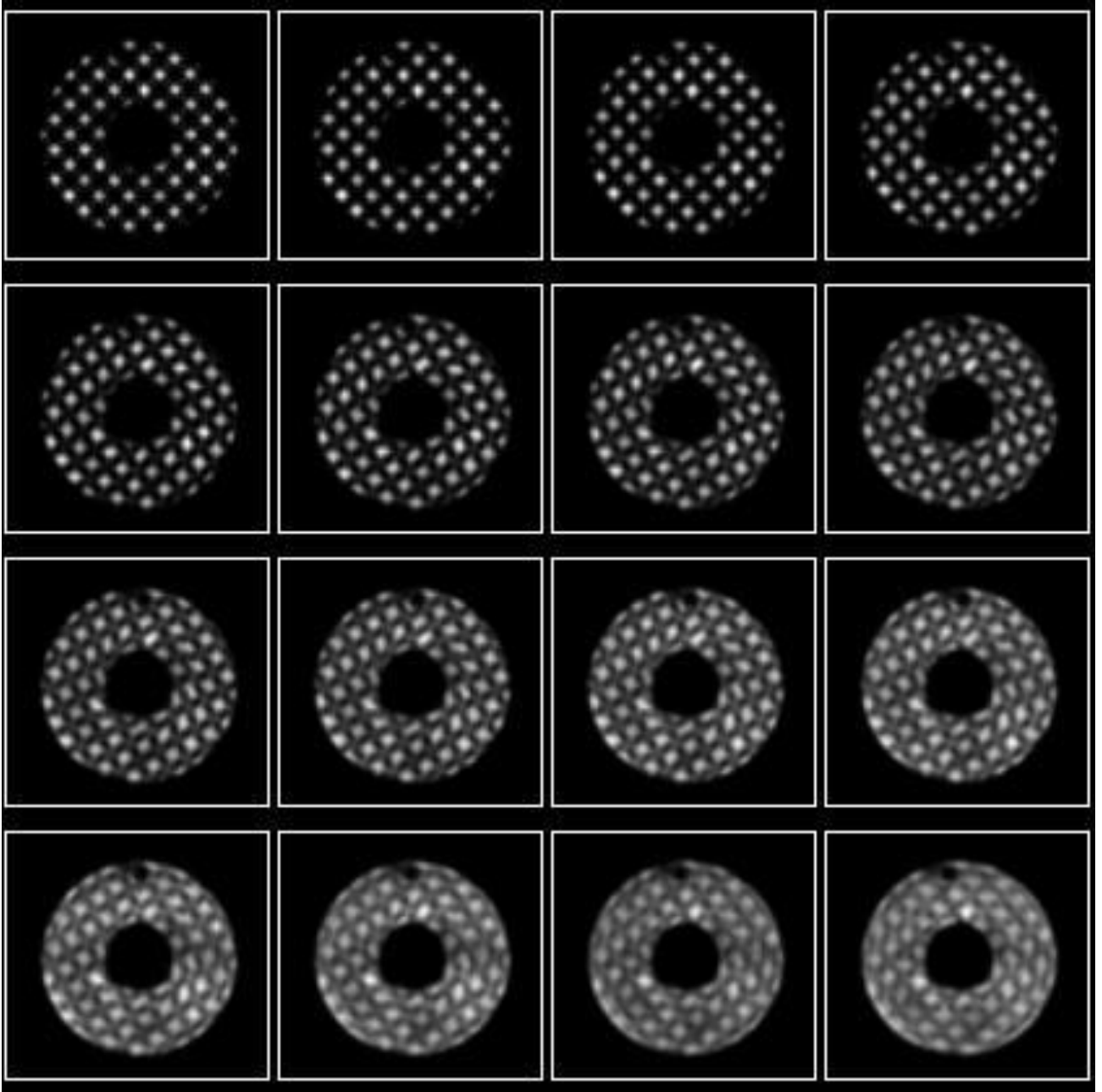


Figure 43. Set of grid tagged cine images from rotation motion phantom 15 degree rotation run # 1.

Tag 2 - 15 Degree Deformation - 5mm Tagging Line Thickness

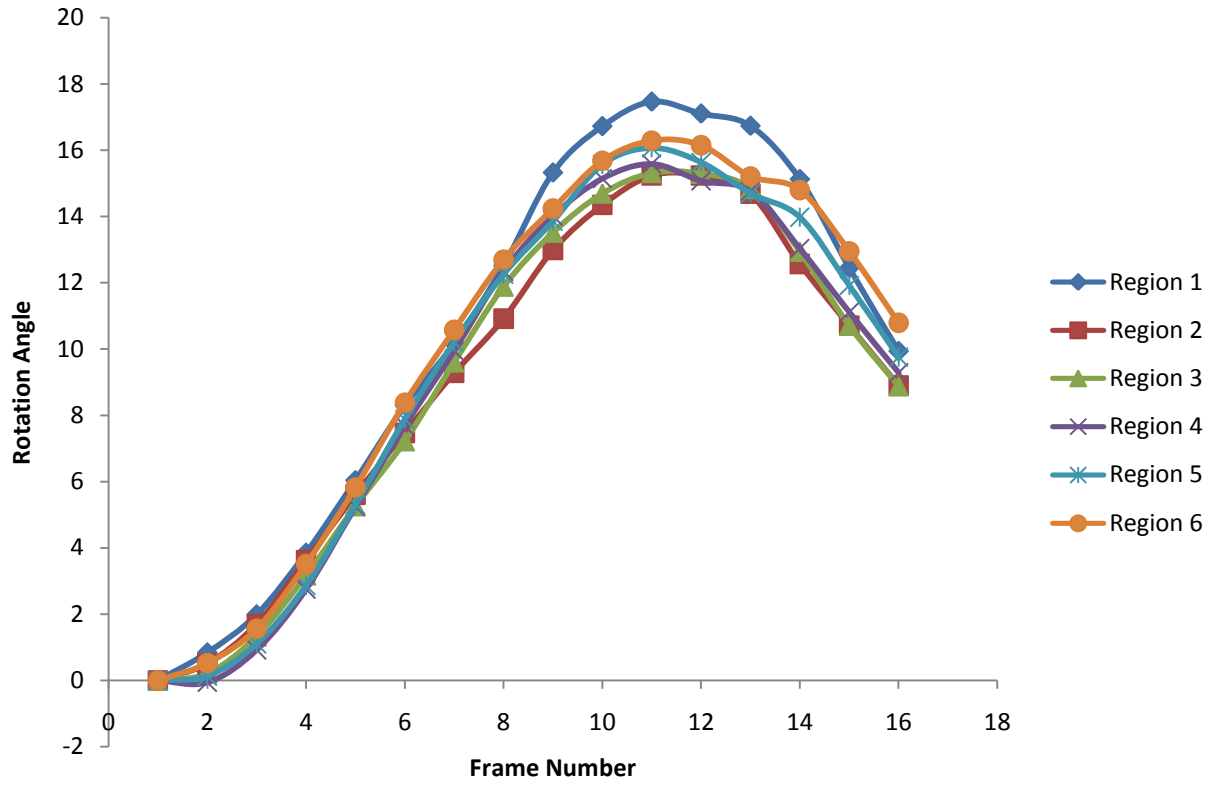


Figure 44. The rotation angle obtained in each frame during the one beat cycle for 15 degree rotation run # 2.

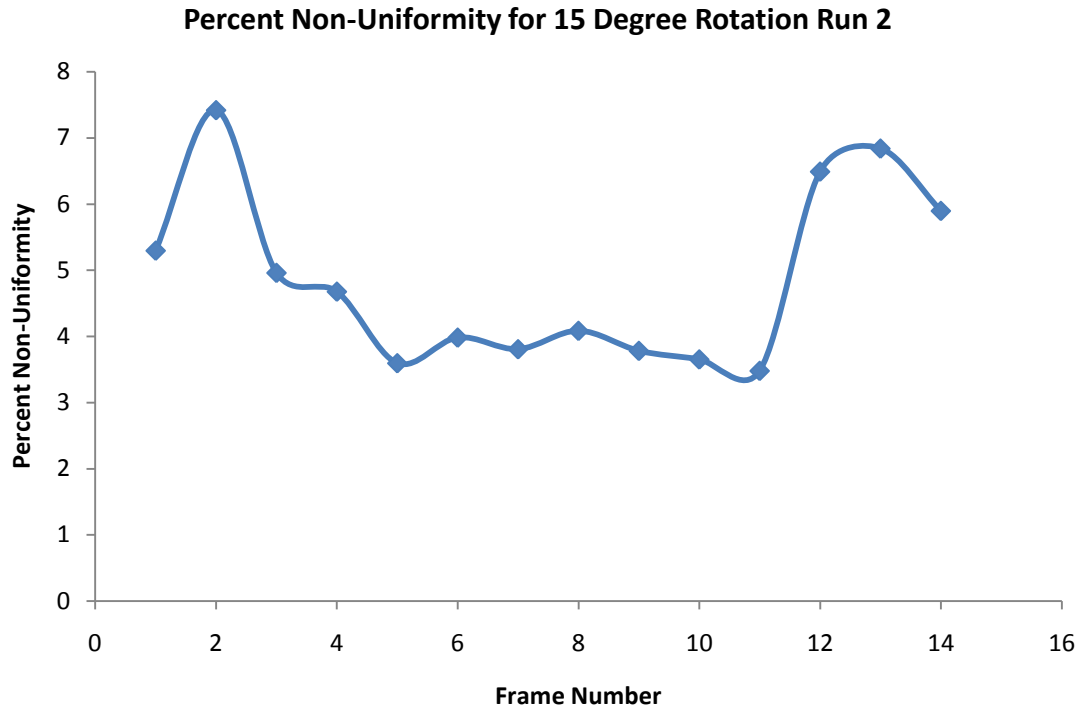


Figure 45. *The non-uniform deformation percentage through the cross section of the gel for 15 degree rotation run 2.*

Up to 8% of non-uniformity which was observed in the gel for the run 2 showed similar behavior as run 1.

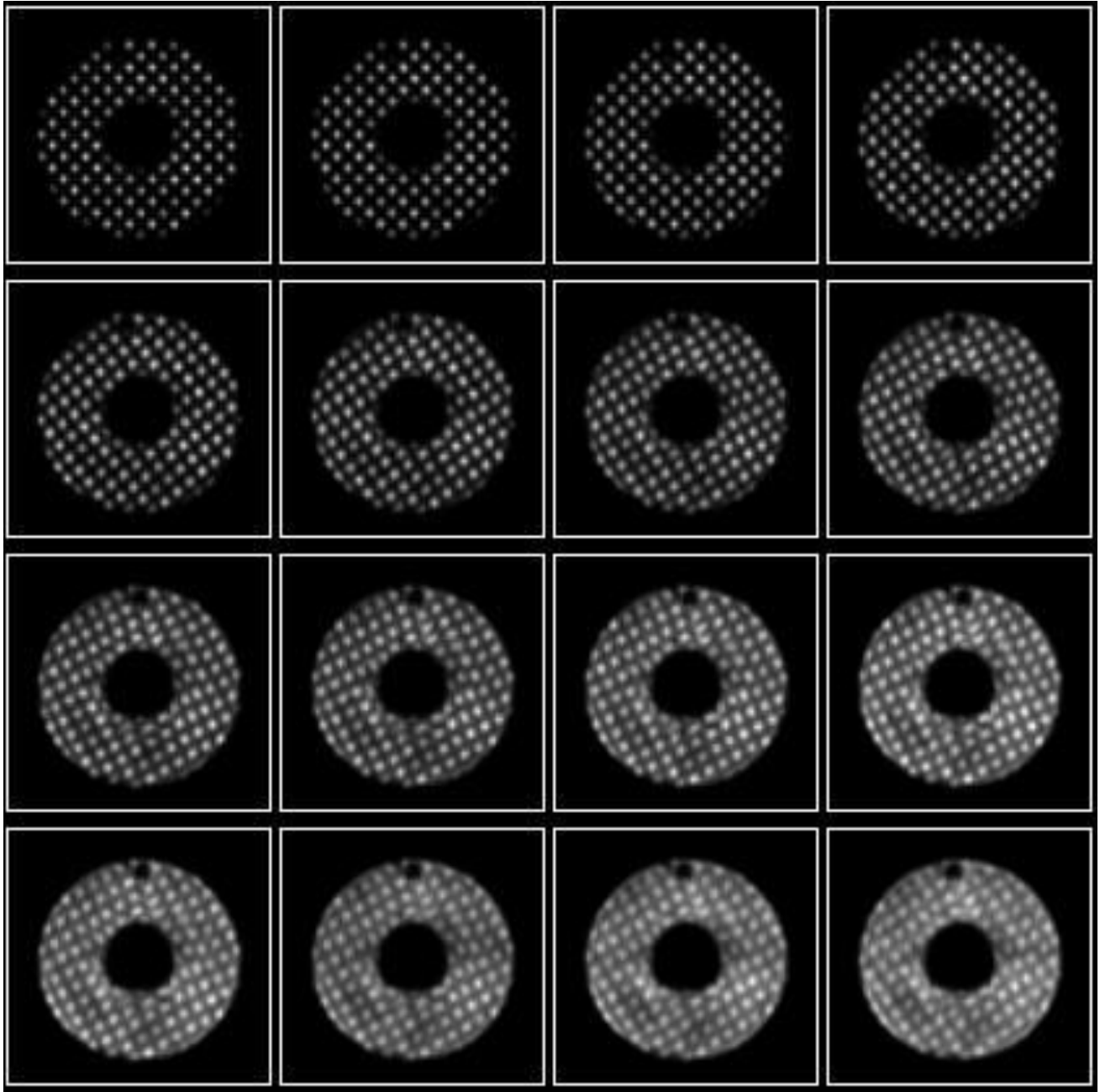


Figure 46. *Set of grid tagged cine images from rotation motion phantom 15 degree rotation run # 2.*

Tag : 3 15 Degree Deformation - 5mm Tagging Line Thickness

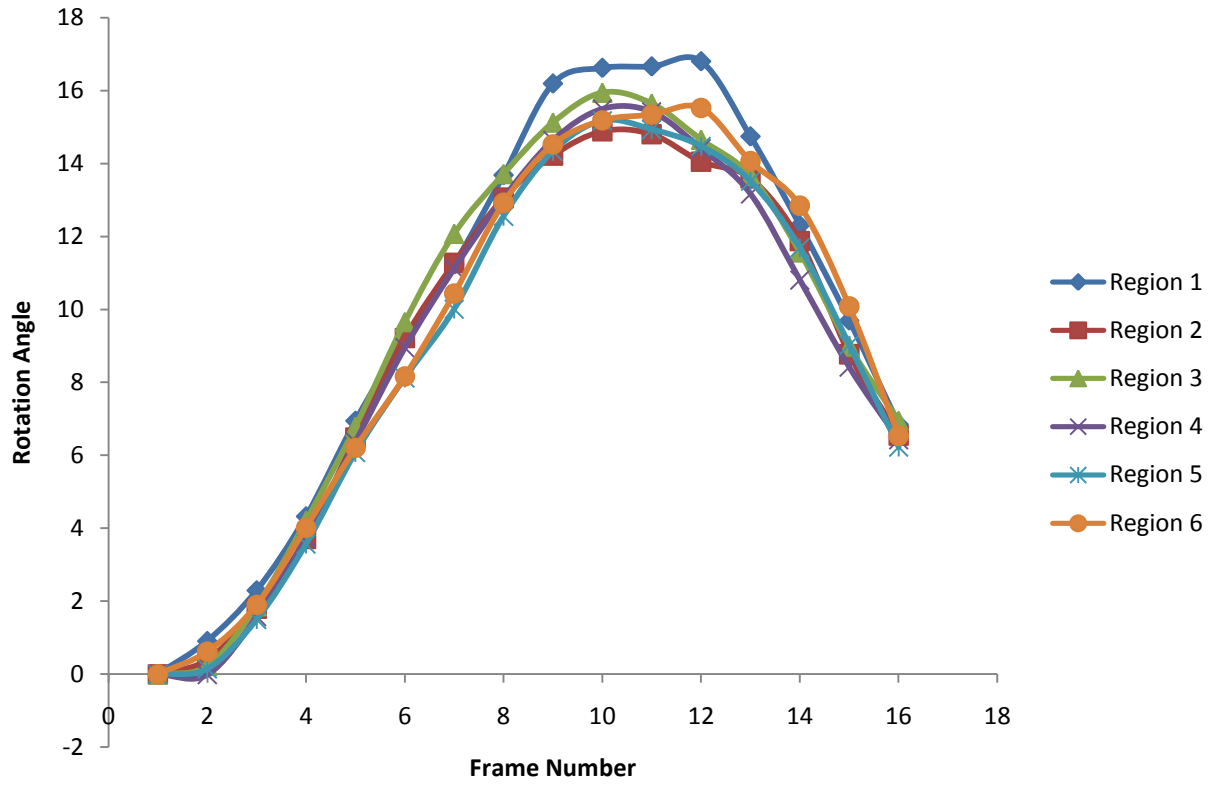


Figure 47. The rotation angle obtained in each frame during the one beat cycle for 15 degree run # 3.

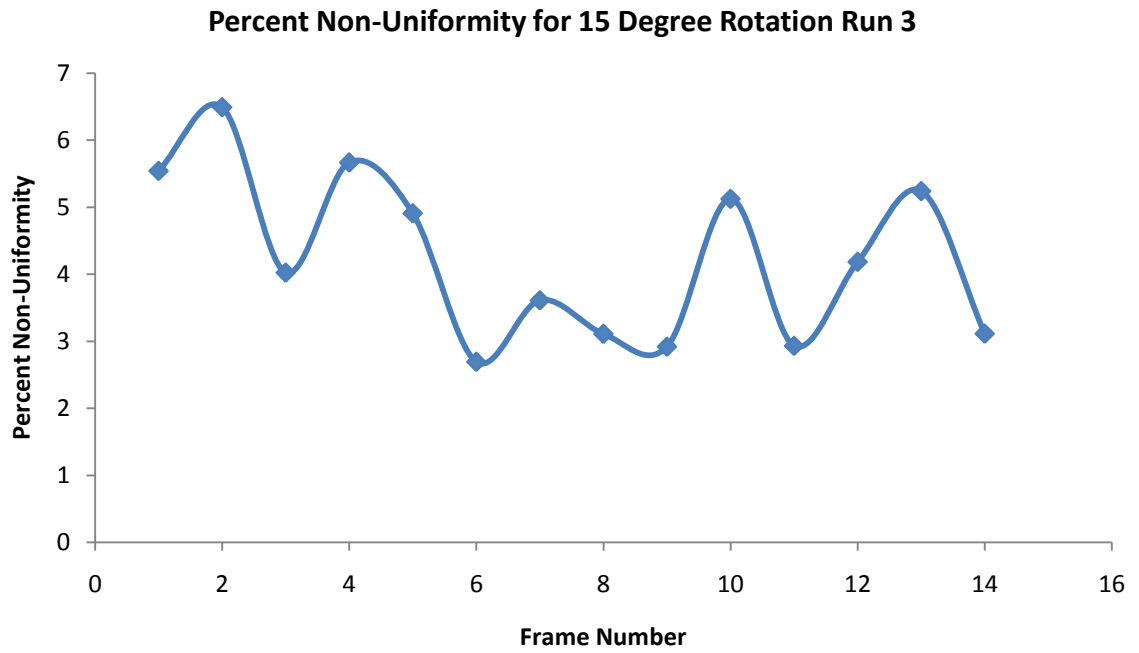


Figure 48. *The non-uniform deformation percentage through the cross section of the gel for 15 degree rotation run 3.*

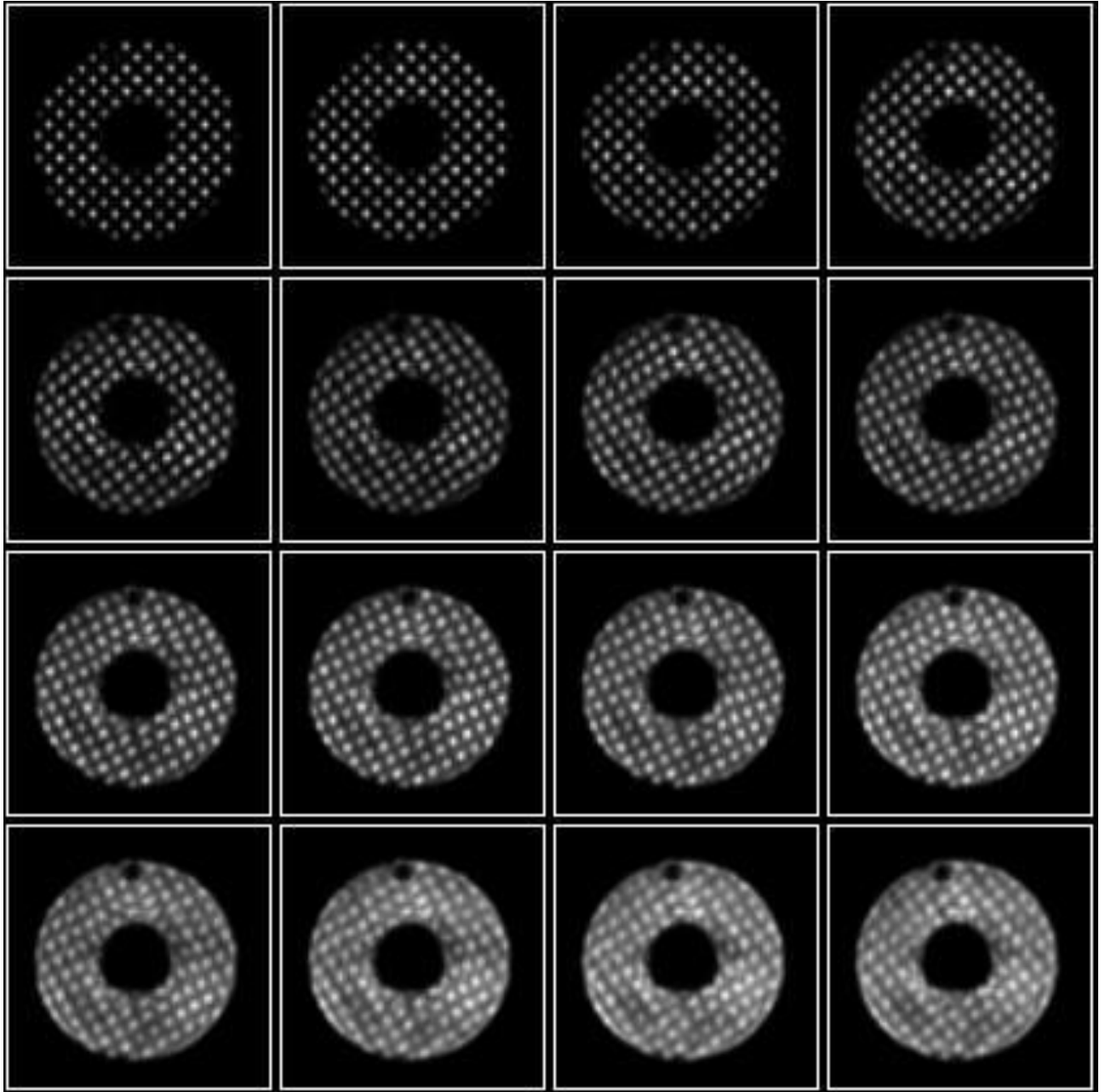


Figure 49. *Set of grid tagged cine images from rotation motion phantom 15 degree rotation run # 3.*

The graph below shows the average rotation degree values of each region of 15 degree rotation run # 1, 2 and 3 in the same graph.

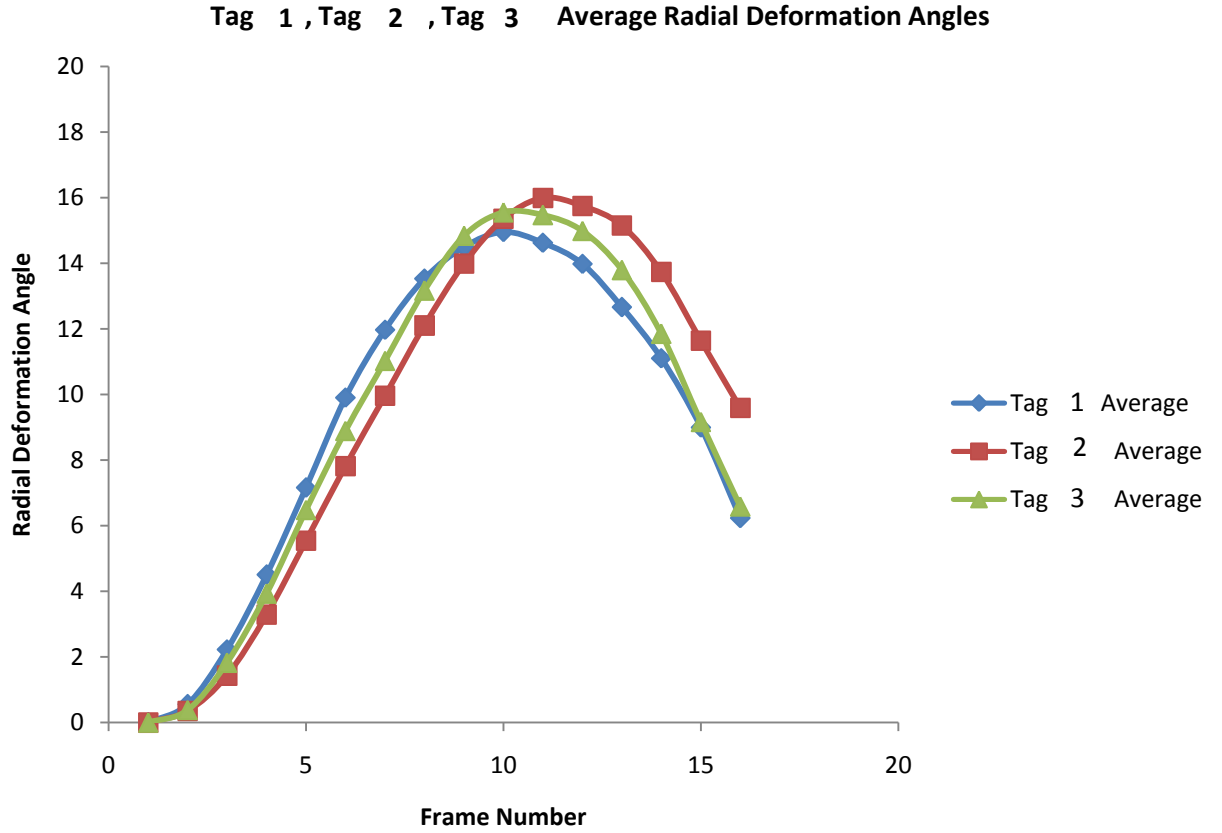


Figure 50. The mean rotation angle obtained in three different runs # 1, 2, and 3 with 15 degree rotation.

Percent Error of RT Motion Phantom with Motion Actuator for 15 Degree

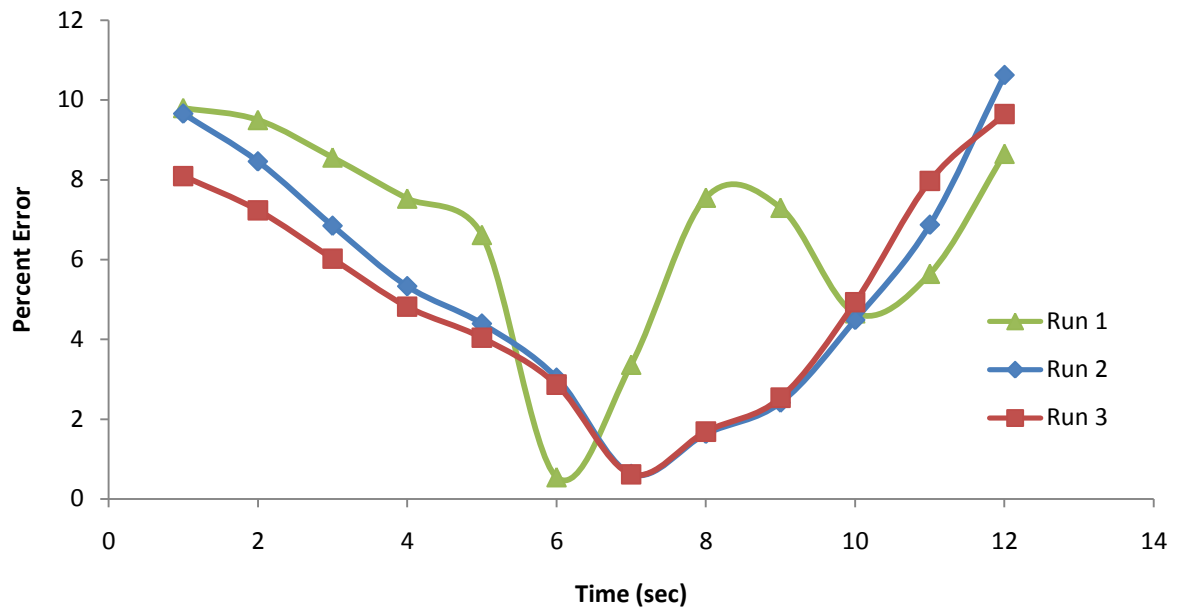


Figure 51. The percent error for the reproducibility of the rotation motion phantom 15 degree rotation for different runs 1, 2, and 3 are shown.

20° Rotation Deformation Motion

Three different experimental runs which were named as 1, 2, and 3 were done with adjusting the plastic actuator at 20 degree rotation settings.

Tag 1 20 Degree Deformation - 7mm Tagging Line Thickness

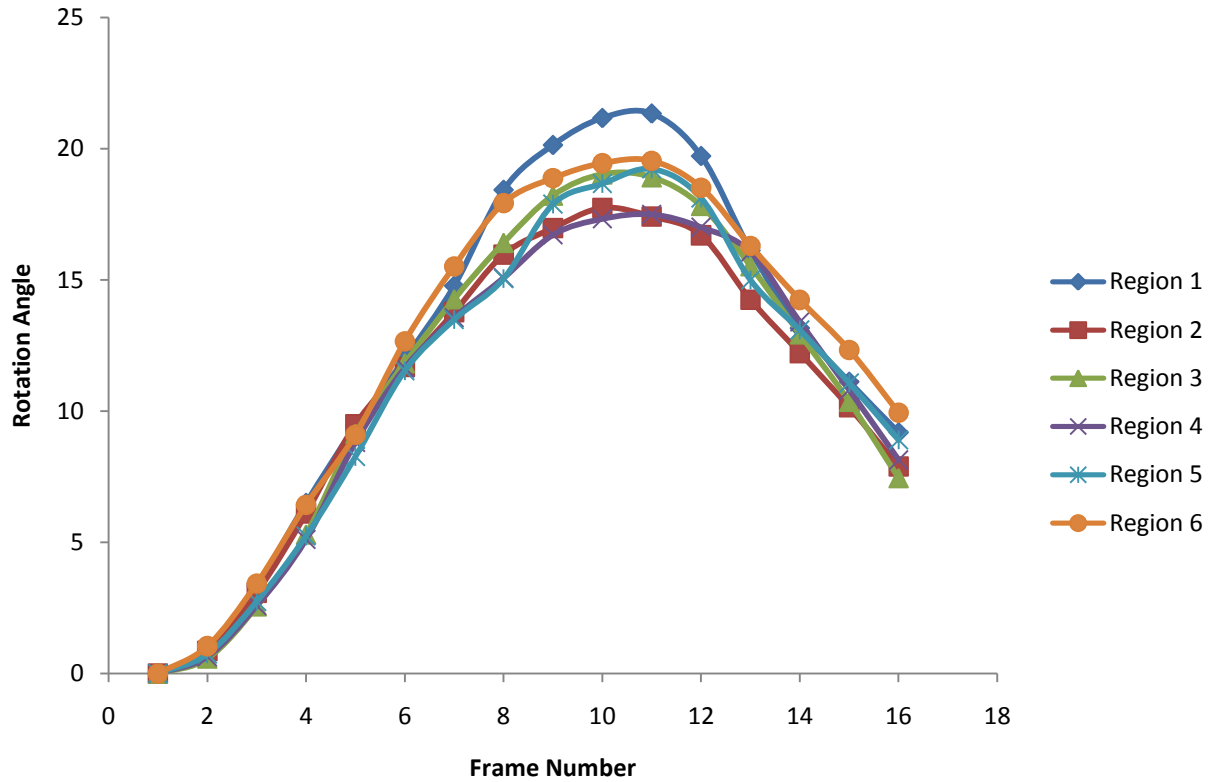


Figure 52. The rotation angle obtained in each frame during the one beat cycle for 20 degree rotation run # 1.

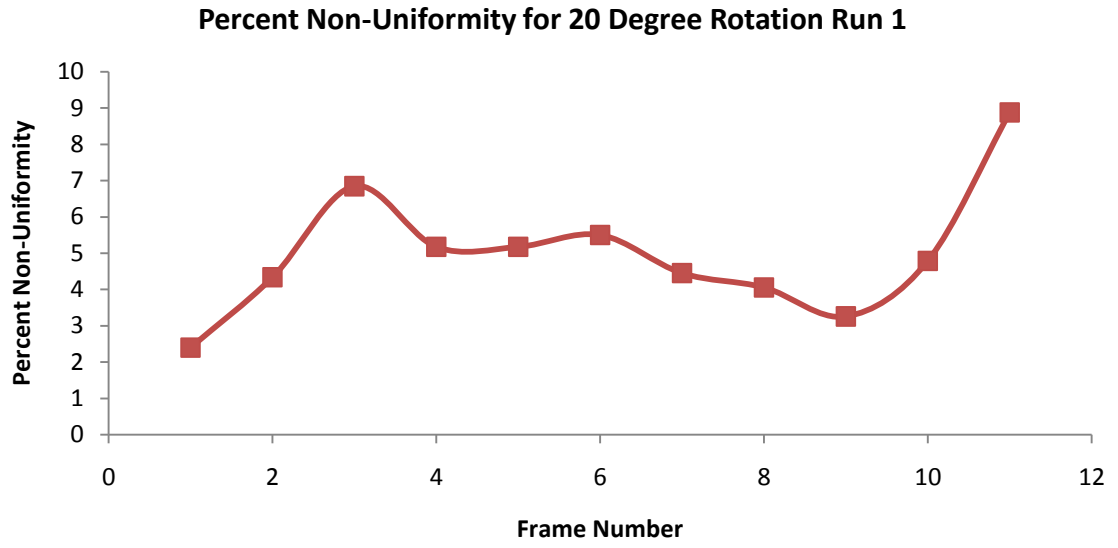


Figure 53. *The non-uniform deformation percentage through the cross section of the gel for 20 degree rotation run 1.*

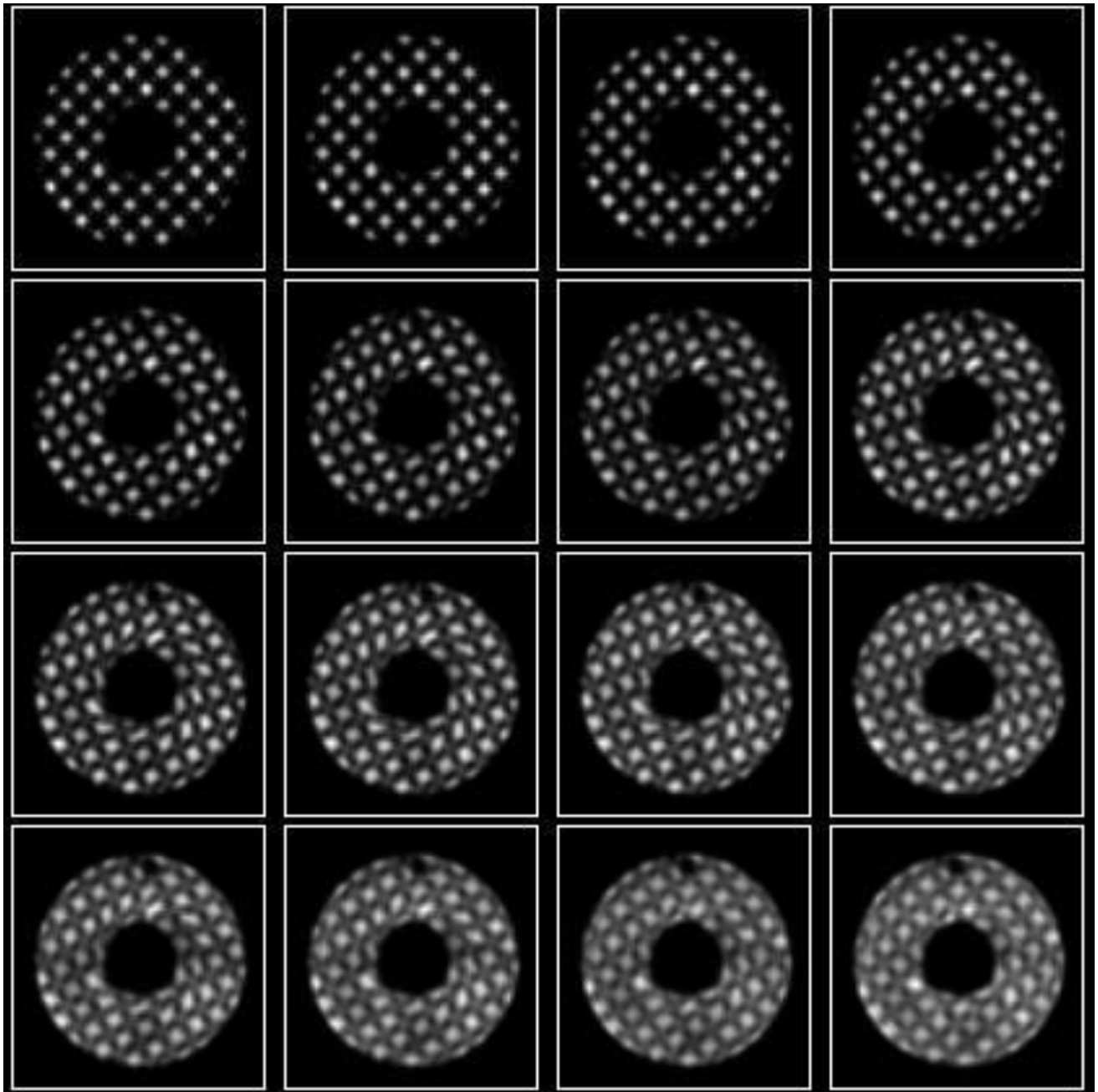


Figure 54. *Set of grid tagged cine images from rotation motion phantom 20 degree rotation run # 1.*

Tag 2 20 Degree Deformation - 5mm Tagging Line Thickness

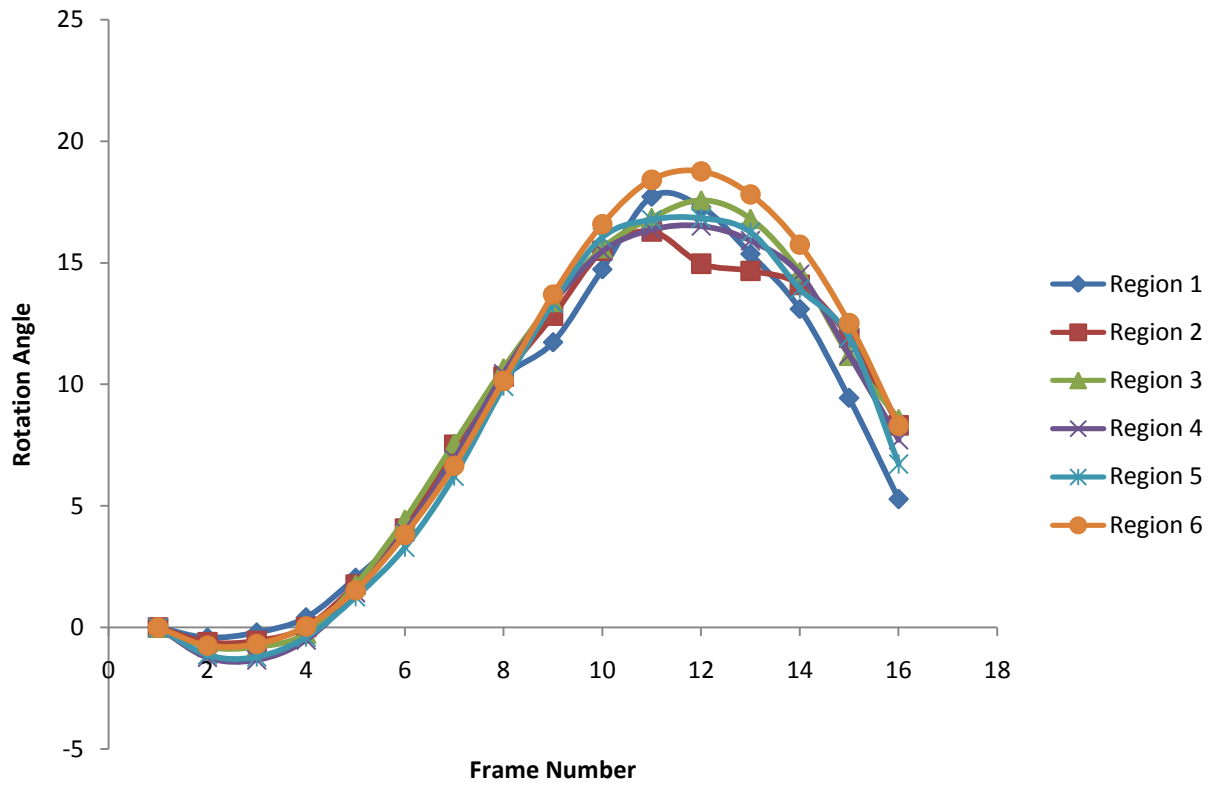


Figure 55. The rotation angle obtained in each frame during the one beat cycle for 20 degree rotation run # 2.

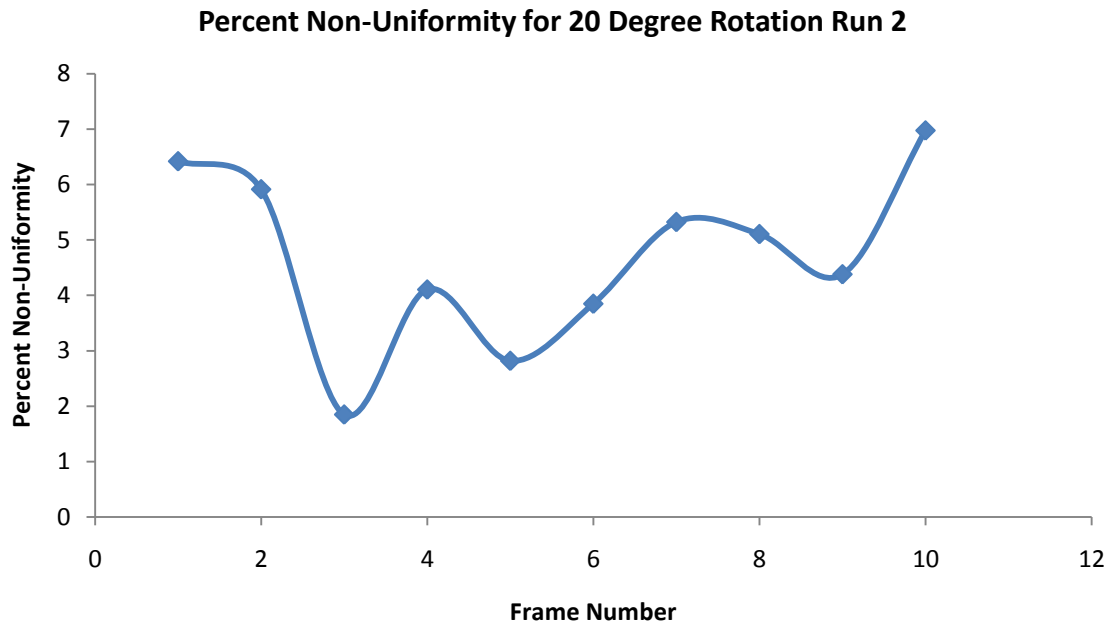


Figure 56. *The non-uniform deformation percentage through the cross section of the gel for 20 degree rotation run 2.*

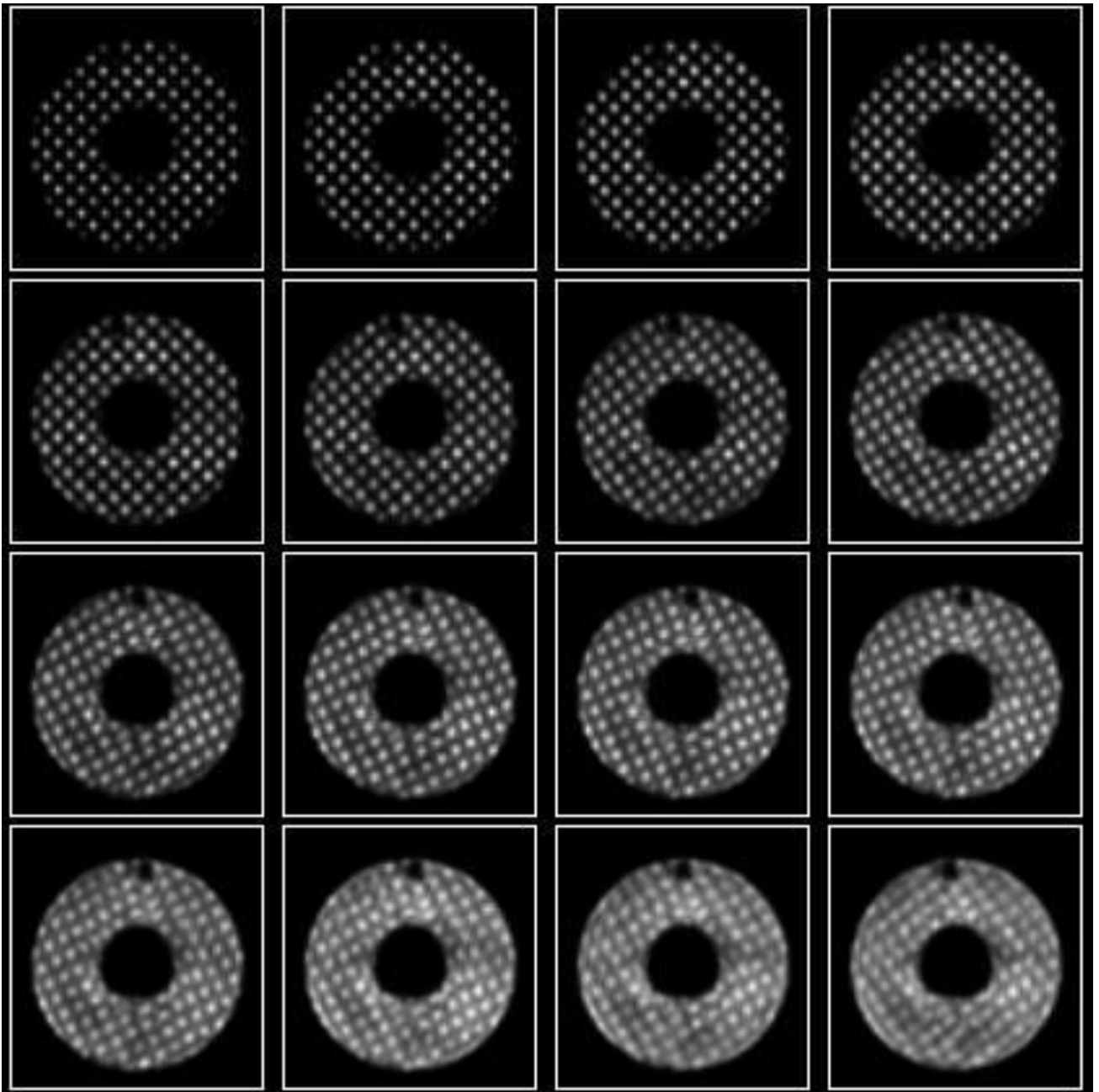


Figure 57. Set of grid tagged cine images from rotation motion phantom 20 degree rotation run # 2.

Tag 3 20 Degree Deformation - 5mm Tagging Line Thickness

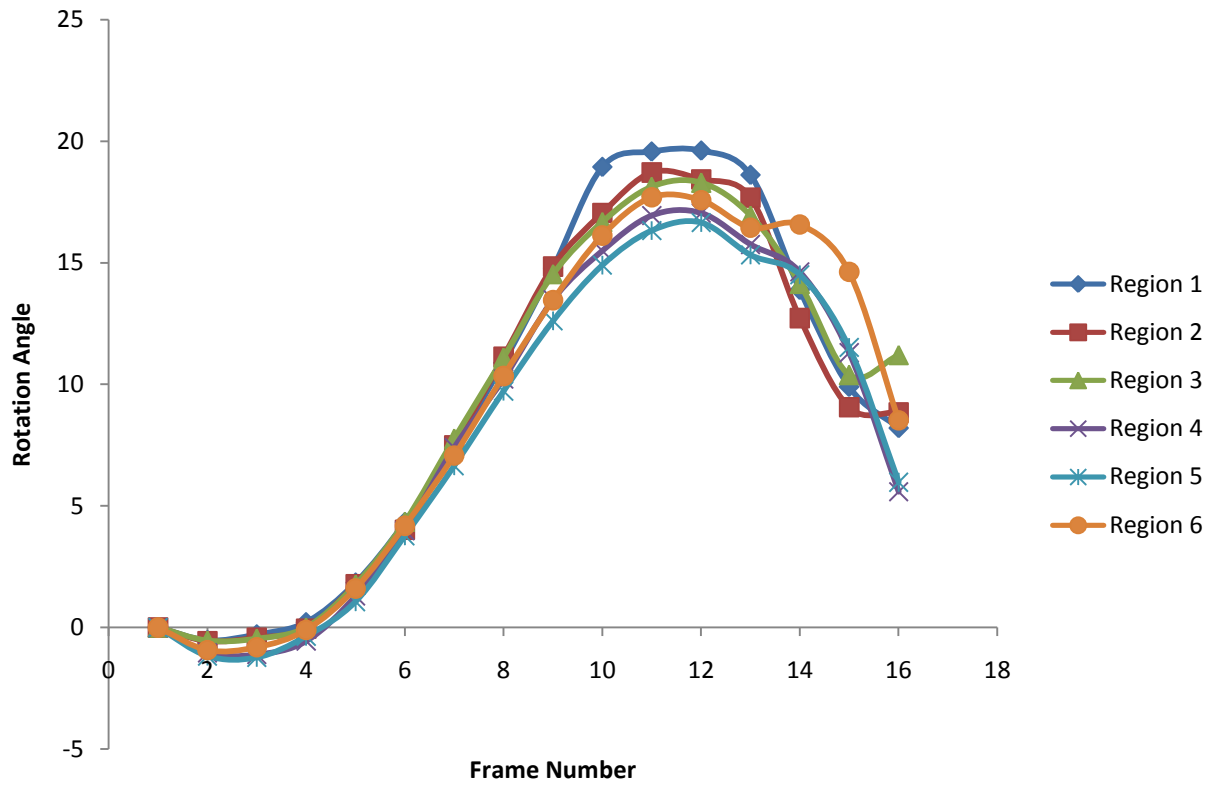


Figure 58. The rotation angle obtained in each frame during the one beat cycle for 20 degree rotation run # 3.

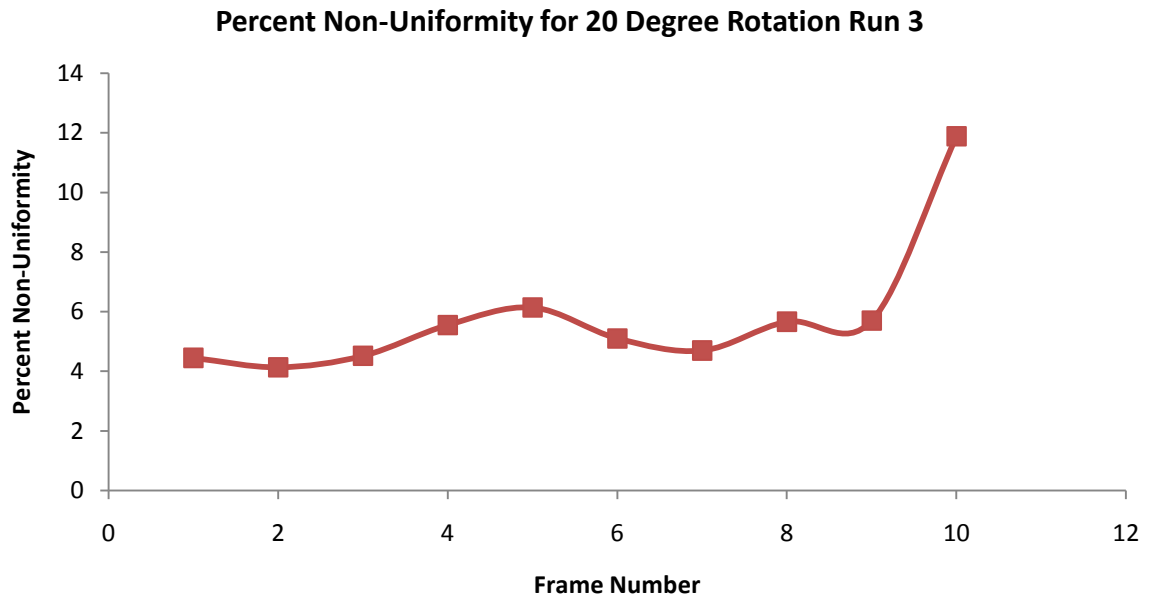


Figure 59. *The non-uniform deformation percentage through the cross section of the gel for 20 degree rotation run 3.*

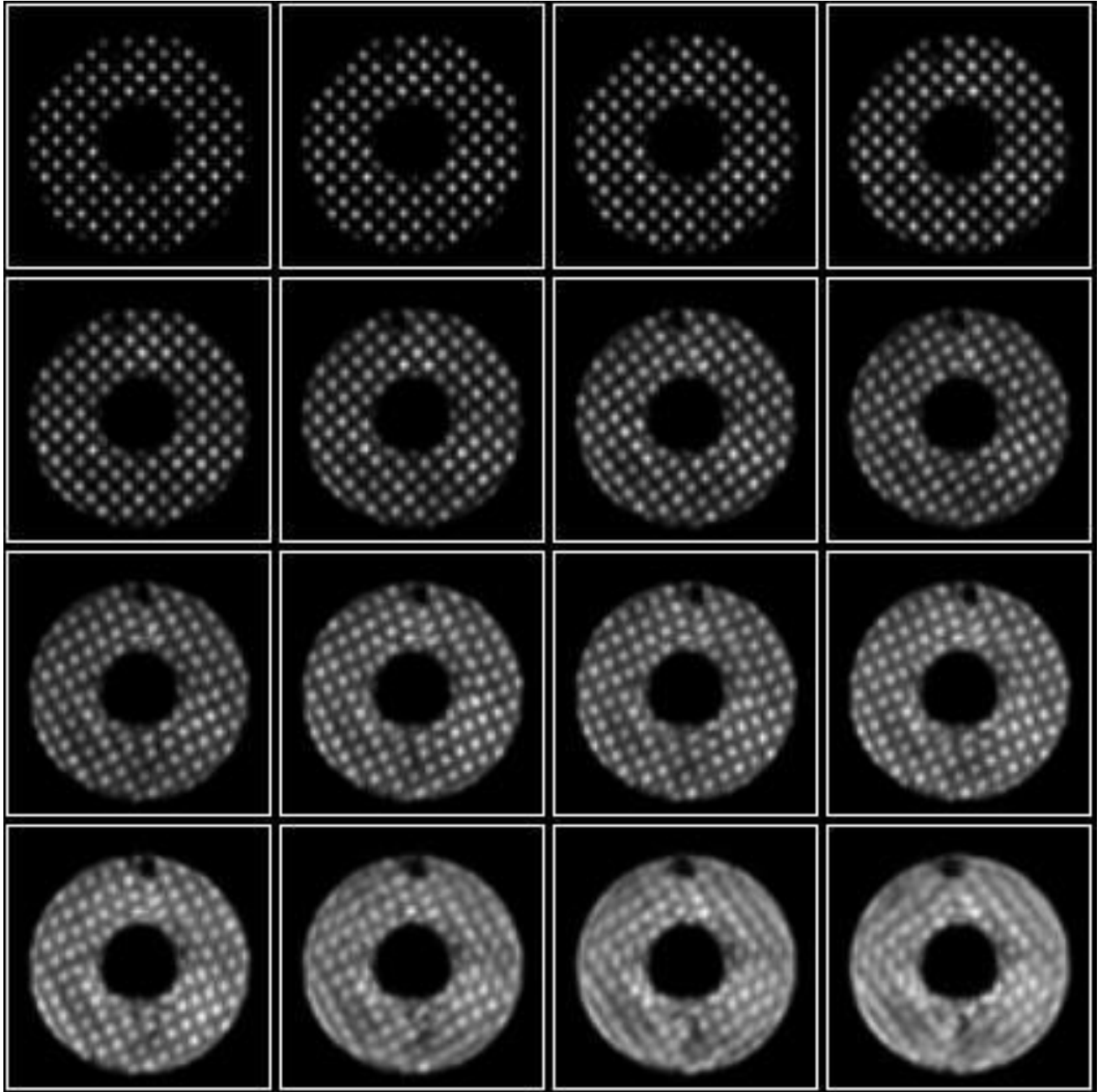


Figure 60. *Set of grid tagged cine images from rotation motion phantom 20 degree rotation run # 3.*

The graph below shows the average rotation degree values of 20 degree rotation run # 1, 2 and 3 in the same graph.

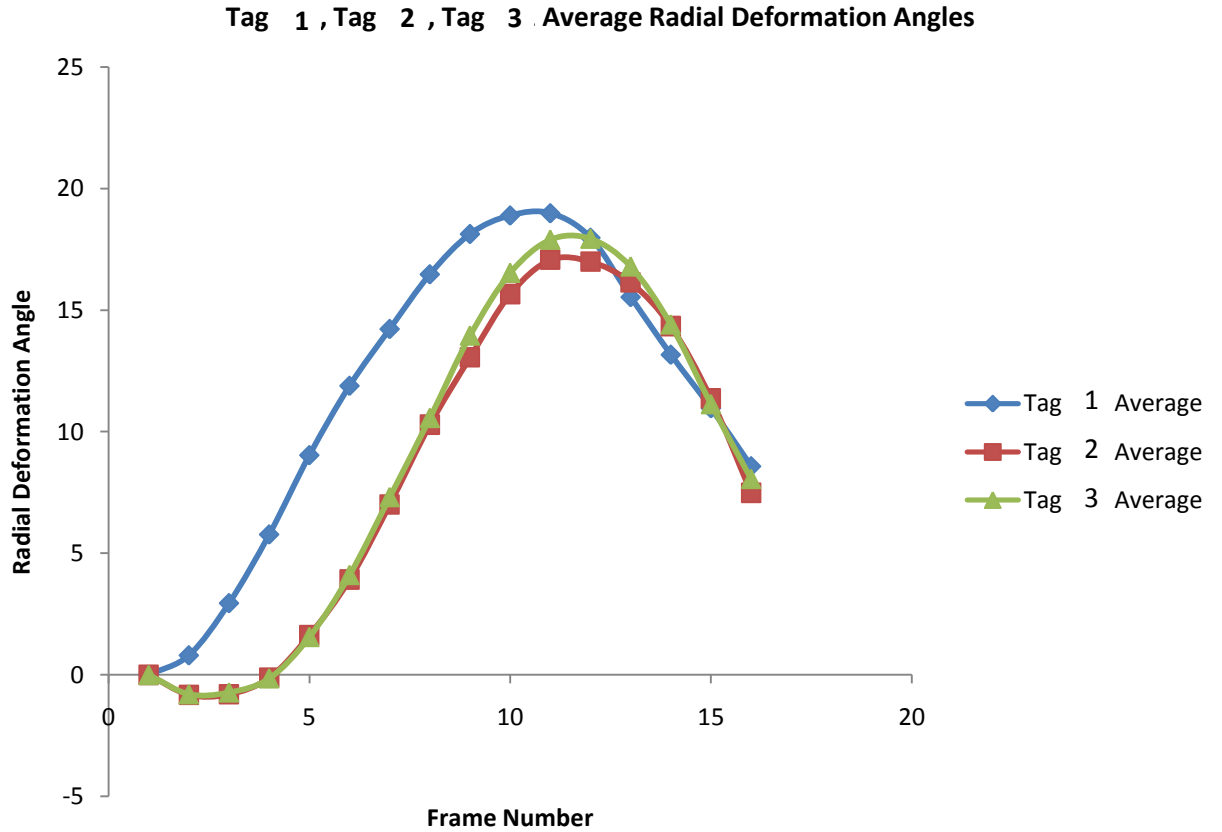


Figure 61. *The mean rotation angle obtained in three different 20 degree rotation runs # 1, 2, and 3.*

Percent Error of RT Motion Phantom with Motion Actuator for 20 Degree

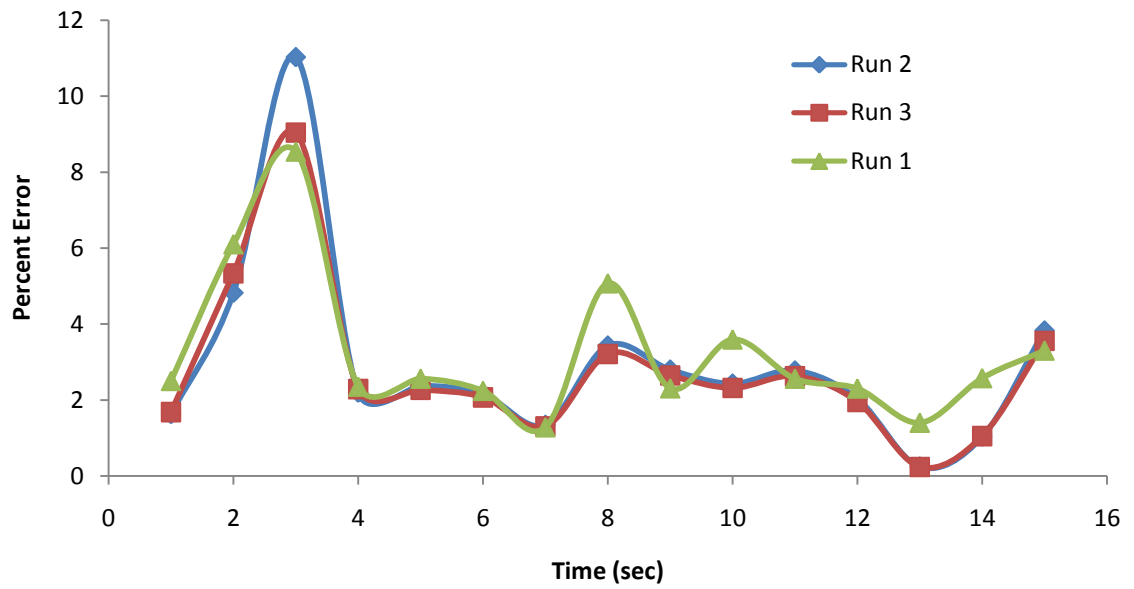


Figure 62. *The percent error for the reproducibility of the rotation motion phantom 20 degree rotation for different runs 1, 2, and 3 are shown.*

35° Rotation Deformation Motion

Three different experimental runs which were named as 1, 2, and 3 were done with adjusting the plastic actuator at 35 degree rotation settings.

Tag 1 35 Degree Deformation - 5mm Tagging Line Thickness

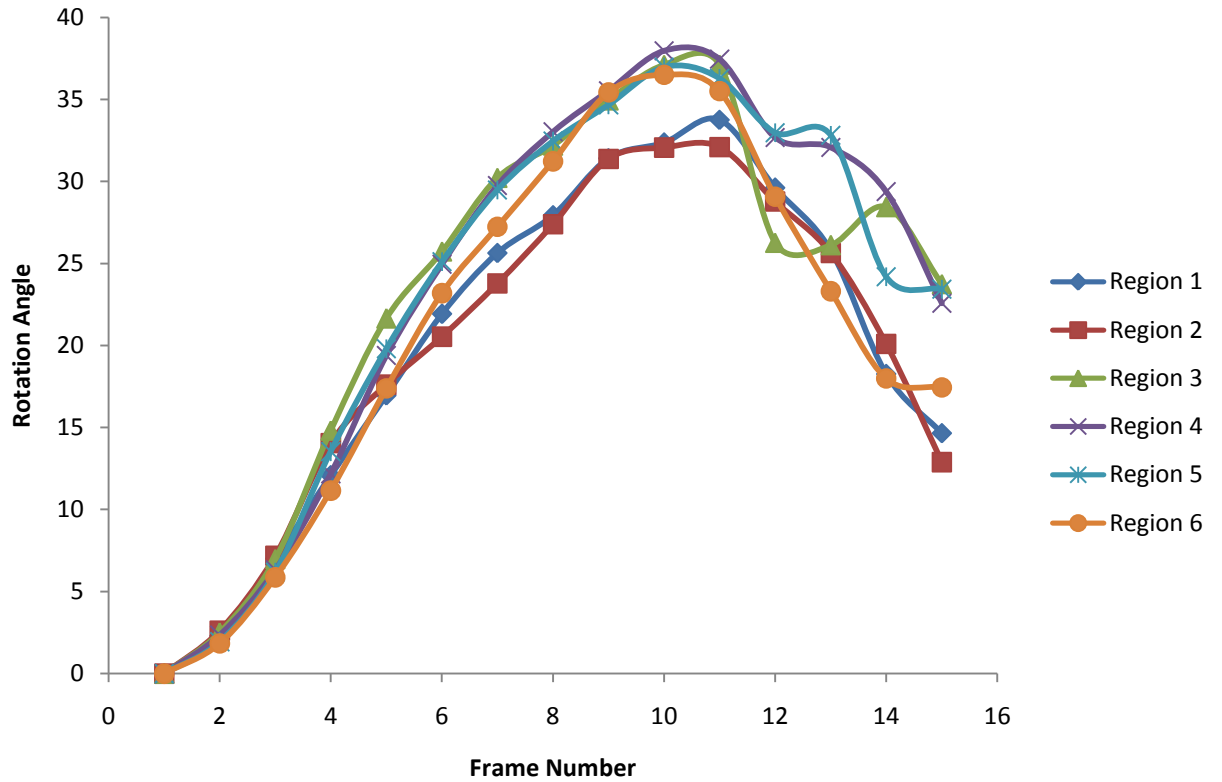


Figure 63. *The rotation angle obtained in each frame during the one beat cycle for 35 degree rotation run # 1.*

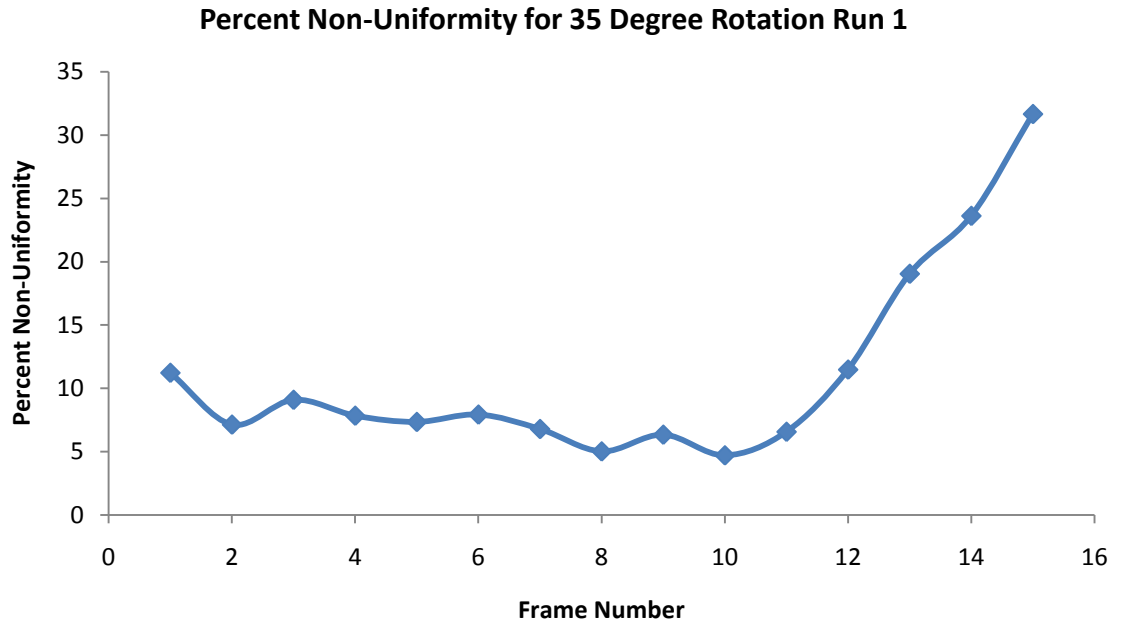


Figure 64. *The non-uniform deformation percentage through the cross section of the gel for 35 degree rotation run 1.*

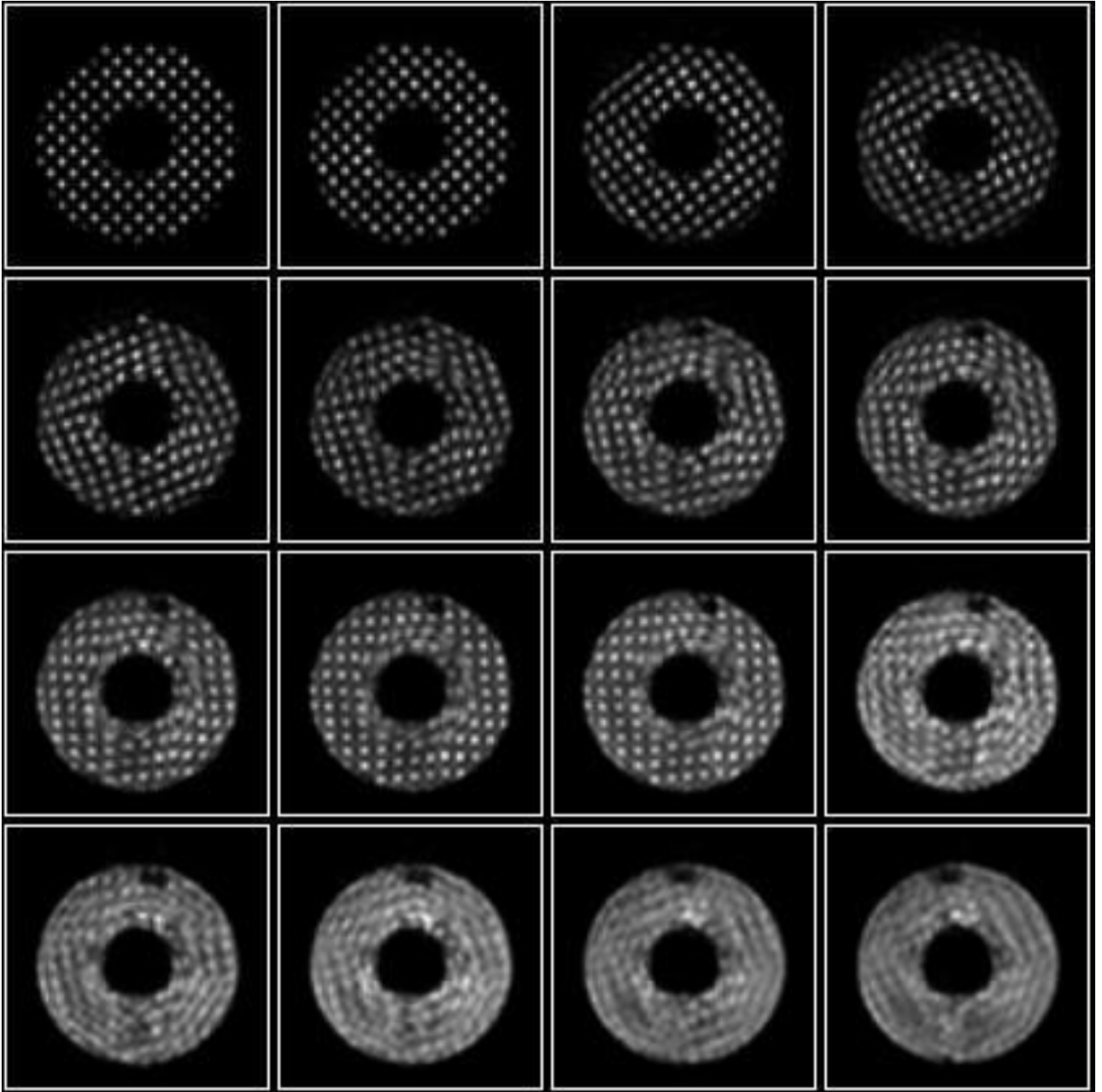


Figure 65. *Set of grid tagged cine images from rotation motion phantom 35 degree rotation run # 1.*

2 701 - 35 Degree Deformation - 5mm Tagging Line Thickness

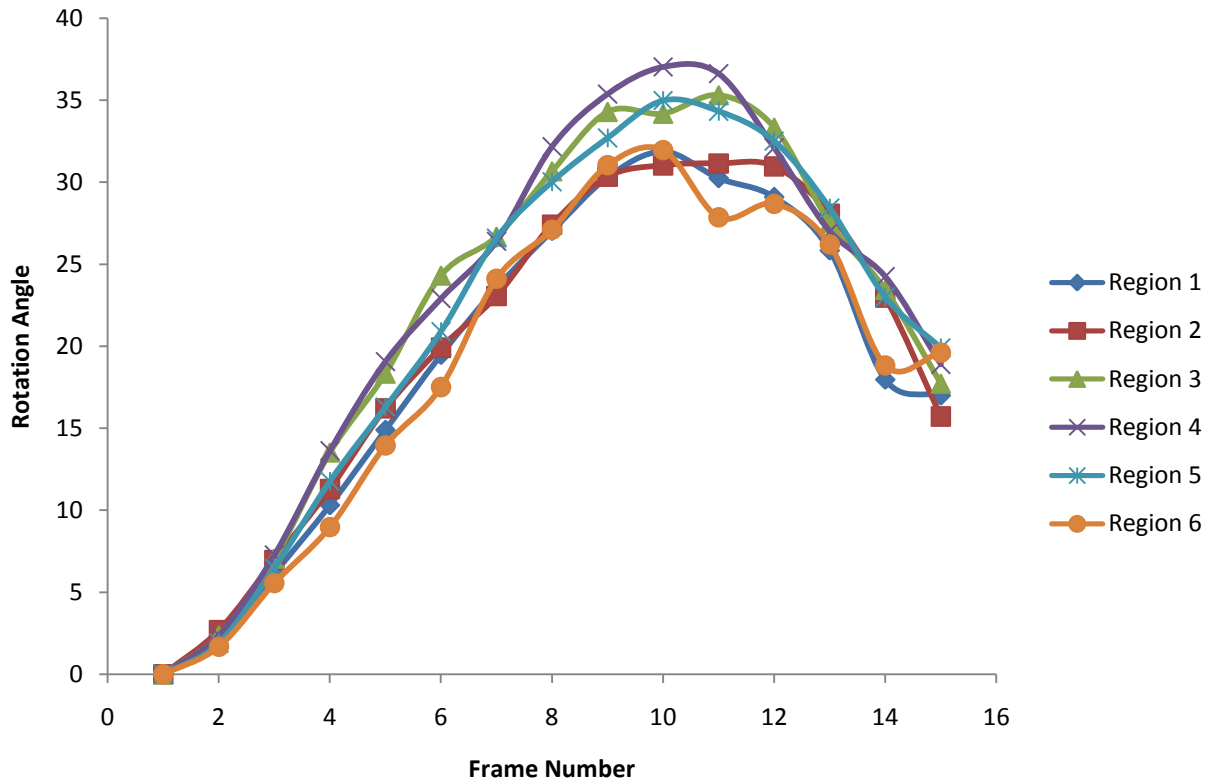


Figure 66. The rotation angle obtained in each frame during the one beat cycle for 35 degree rotation run # 2.

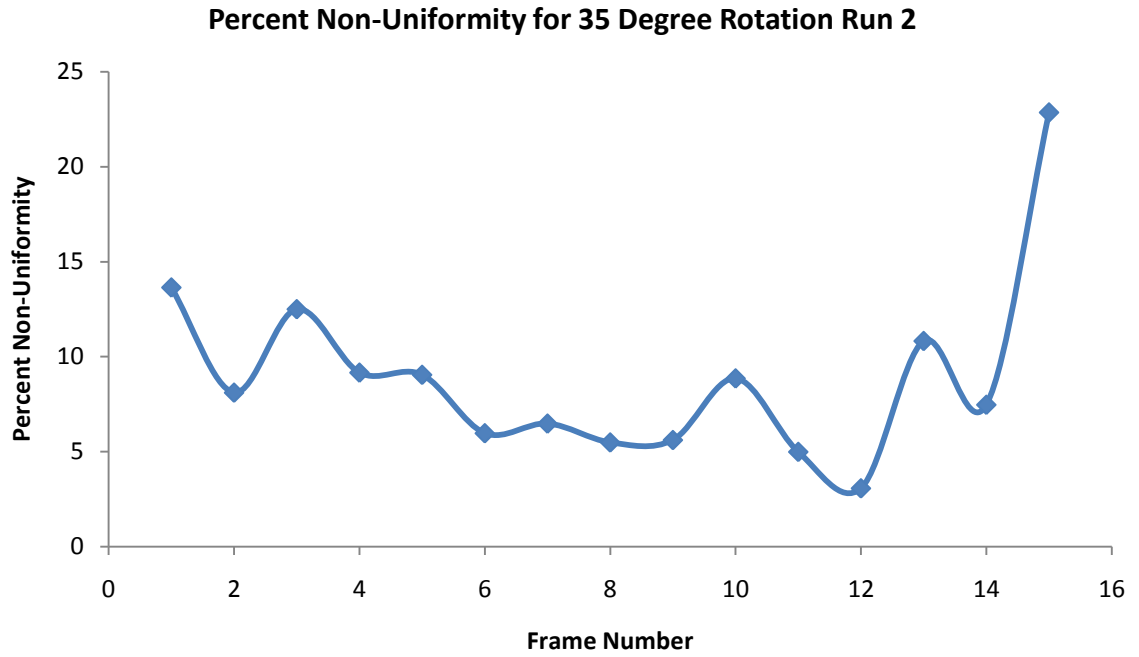


Figure 67. *The non-uniform deformation percentage through the cross section of the gel for 35 degree rotation run 2.*

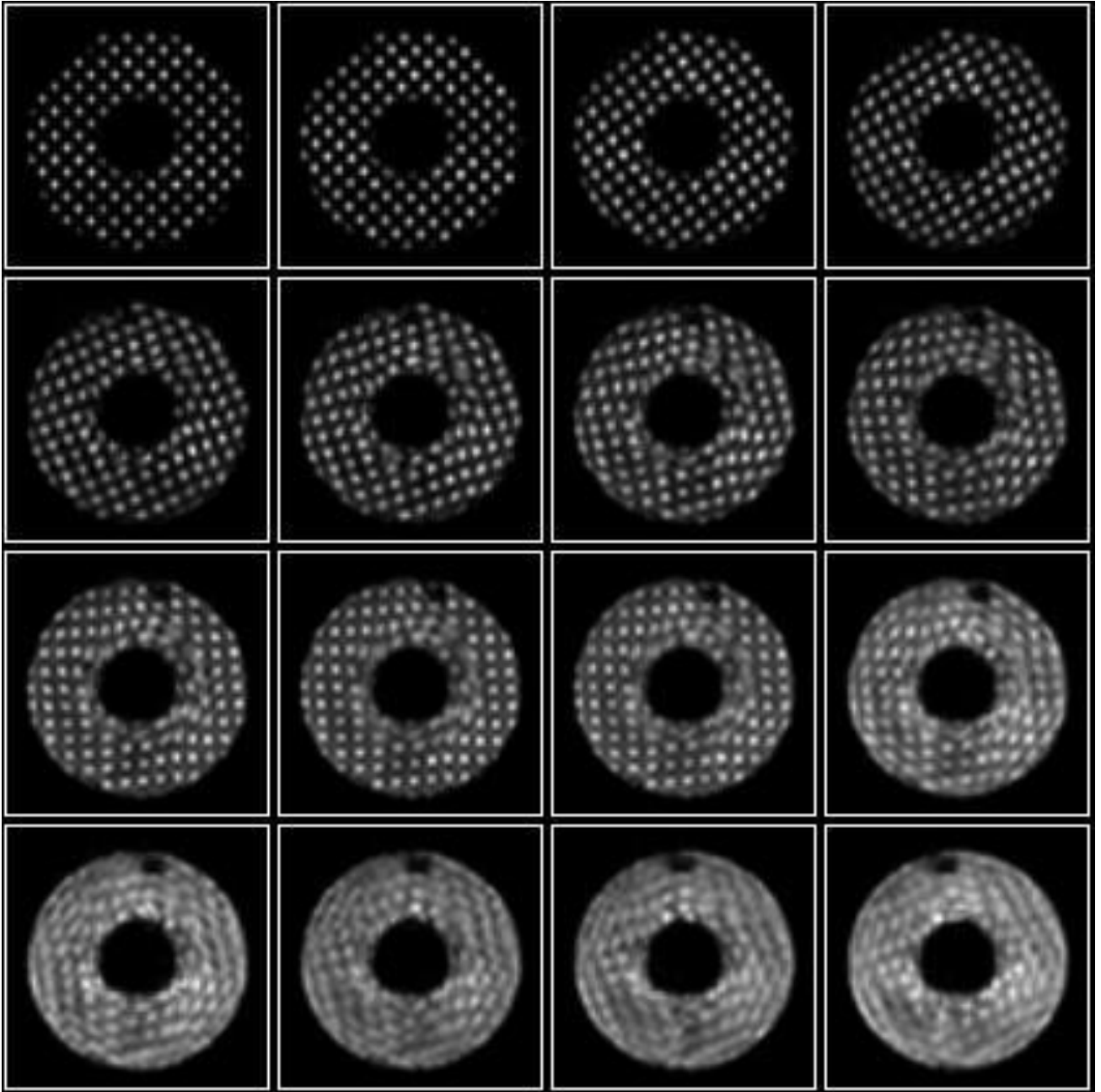


Figure 68. *Set of grid tagged cine images from rotation motion phantom 35 degree rotation run # 2.*

Tag 3 35 Degree Deformation - 5mm Tagging Line Thickness

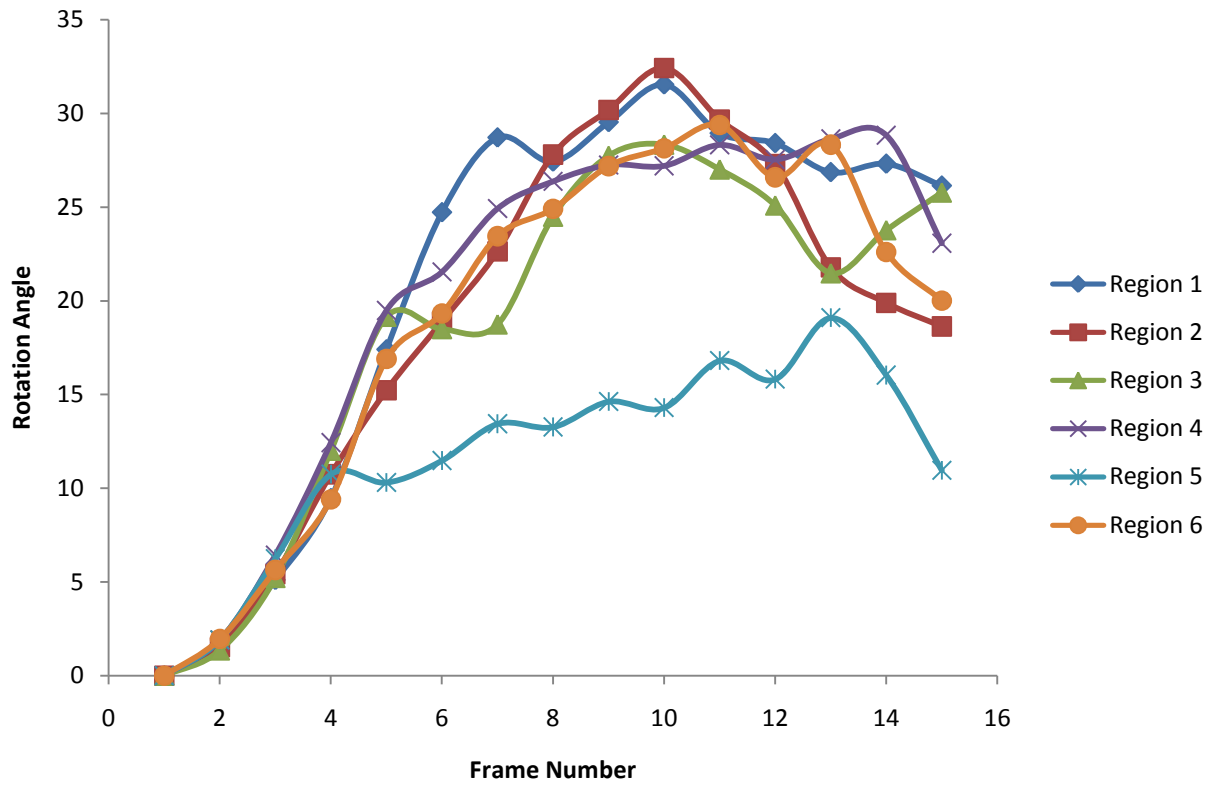


Figure 69. The rotation angle obtained in each frame during the one beat cycle for 35 degree rotation run # 3.

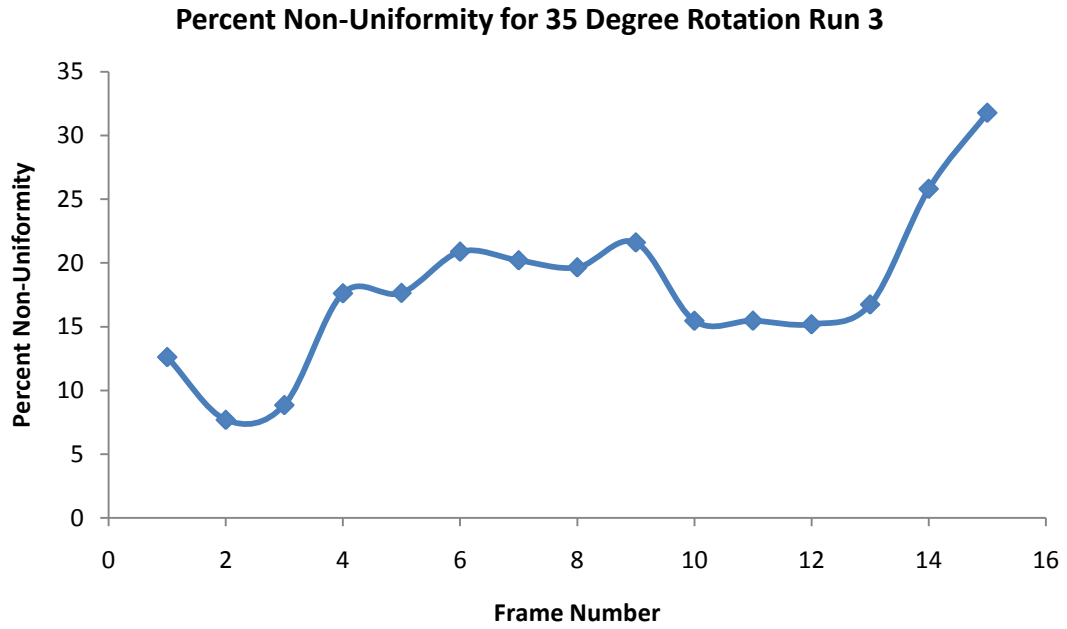


Figure 70. *The non-uniform deformation percentage through the cross section of the gel for 35 degree rotation run 3.*

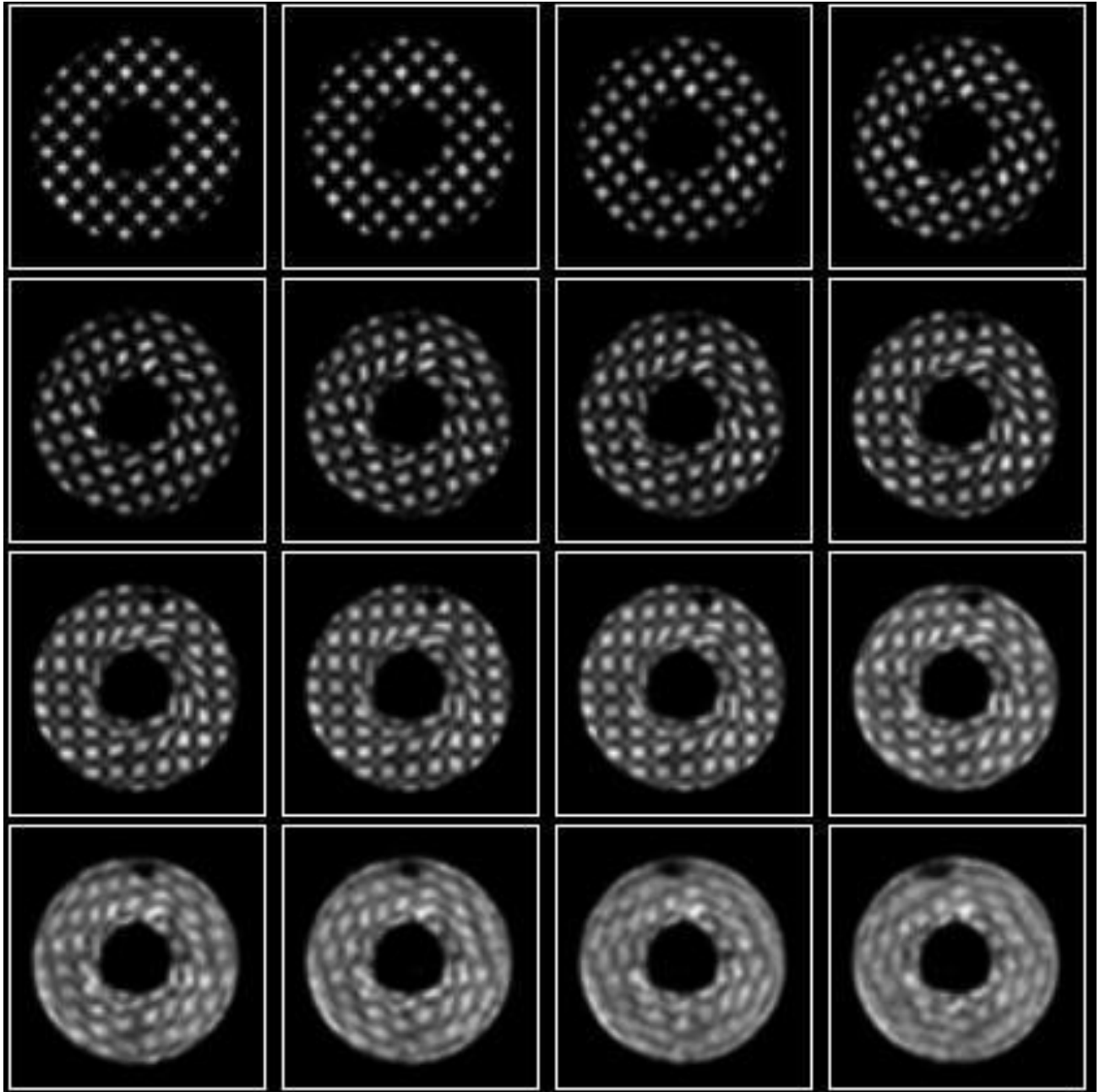


Figure 71. Set of grid tagged cine images from rotation motion phantom 35 degree rotation run # 3.

The graph below shows the average rotation degree values of 35 degree rotation run # 1, 2 and 3 in the same graph.

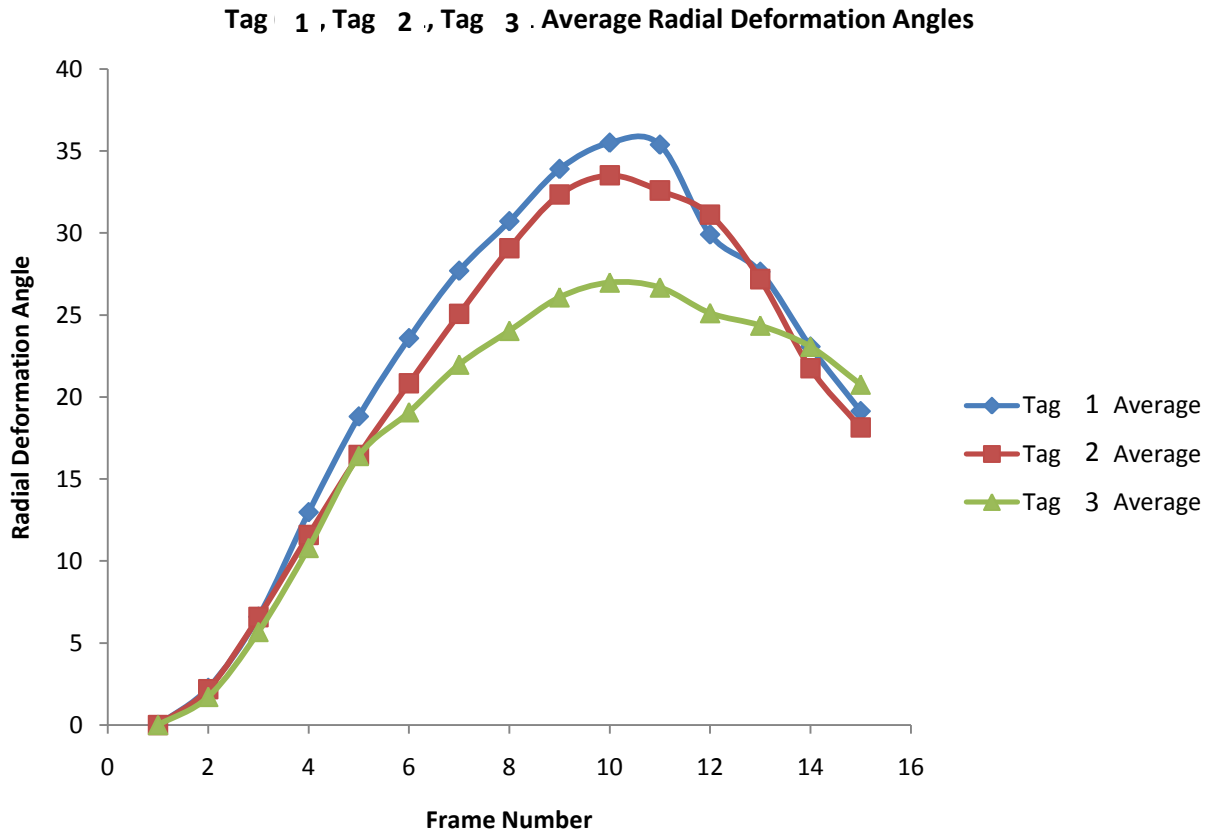


Figure 72. The mean rotation angle obtained in three different 35 degree rotation runs # 1, 2, and 3.

Percent Error of RT Motion Phantom with Motion Actuator for 35 Degree

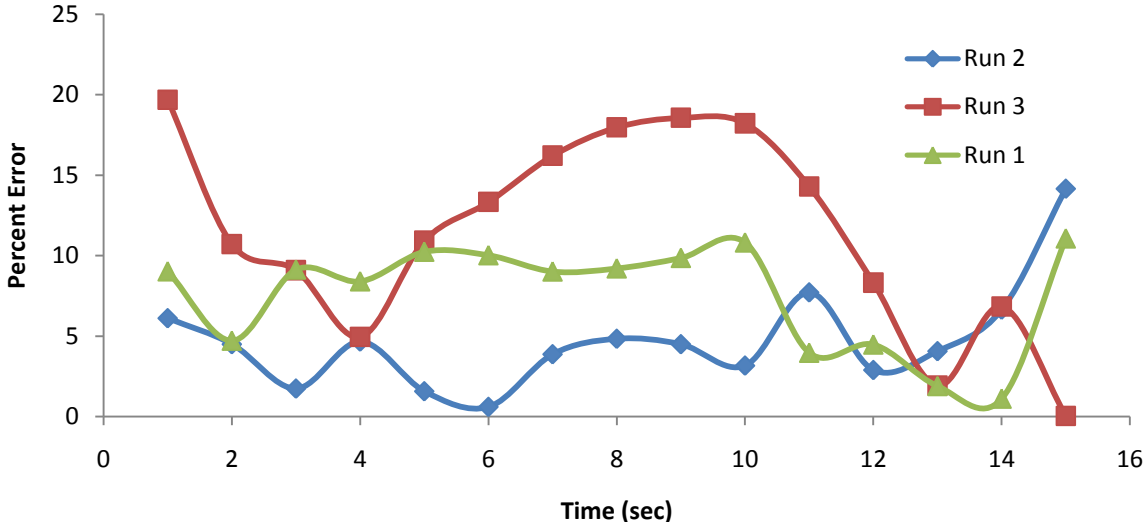


Figure 73. The percent error for the reproducibility of the rotation motion phantom 35 degree rotation for different runs 1, 2, and 3 are shown.

5.3.2 Discussion

According to results in section 5.3.1, the minimum reproducibility for the 15 and 20 degrees were 90% and for 35 degree was 80%. The different amount of angular deformations on the gel was achieved with 90% uniformity throughout the gel for 15 and 20 degrees. However, due to lack of enough tactility of the gel for 35 degree, there was non uniform deformation in the gel up to 32%. This resulted in 20% deformation variation at 35 degree in different runs. The design and build of the plastic actuator led the transitions between moving directions became insensible and rotation frequency ideally created enough to reproduce a model of heart twist motion with phantom. The triggering of the phantom motion was done automatically by attaching roller switch on to right crank shaft of the actuator (please see Figure 37). Also, adjustable crank pin enabled precise setting of the different rotation angles (15, 20 and 35 degrees). Amount of twist created in the left ventricle by the each beat of actual heart is 16 ± 2.4 degree which was in the range of phantom settings. The results obtained for 15 and 20 degrees shows that there was no fault in any components of the rotation motion experimental setup and result's waveform shape in the graphs were physiologic. Rotation motion phantom was concluded to be an essential tool to fulfill the needs of verification apparatus to test new pulse sequences and tagging techniques in MRI.

CHAPTER VI

CONCLUSION

The overall goal of this study was to design and build a low-cost left ventricular motion phantom which is capable of accurately modeling both the wall thickening and rotation motions of the left ventricle, with sufficient accuracy and repeatability for use in the evaluation of new pulse sequences. This was accomplished by constructing two different phantoms to mimic the two distinct motions of the left ventricle independently. The phantoms have been operated by each different motion actuators as air pump and actuator but both phantoms were housed in the same enclosure. Successfully, deformation patterns occur in the wall of the left ventricle in the human heart have been reproduced within the phantom gel.

The reproducibility of the deformation patterns depends upon the control of the air pump and the actuator in the experimental setup. By the motion actuators in each phantoms, the user dependent variability has been reduced and an external trigger integrated into both phantoms. In the current experimental conditions, the reproducibility

of the deformations for the wall motion phantom was 96% and the rotation motion phantom was 90%. The T1 relaxation time of the gel was measured as 728.3 milliseconds while myocardium relaxation time of the human is 1115.6 milliseconds.

Tagged cine images of the three different scanning results for each three different amount of angle rotation deformation patterns in the phantom were analyzed by using harmonic phase (HARP) analysis software (Diagnosoft, Inc.). The measured rotation of the grid patterns showed that there was no fault of the motion mechanism of the rotation phantom because the results of the same amount of rotation repetitions were same with each other for 15 and 20 degrees. However, due to lack of tactility of the gel, 35 degree rotation deformation had reproducibility up to 68%. It is also important to mention that the amount of rotation occurs in the actual healthy left ventricle of the human heart is 16 ± 2.4 degrees. In case of illness, rotation amount shows decrease to 10 ± 2.1 degrees. According to that, the results that obtained 15 and 20 degrees conclude that amount of the rotation reproduced in phantom corresponds to results observed in clinical practice.

The cine images of four different scanning results for the same amount of contraction experiments of wall motion phantom were analyzed by using Philips dedicated cardiac image analysis tool. From the cine images, it was observed that up to 77.5% contraction in the phantom walls has been achieved and different runs with the same deformation settings concluded the 96% reproducibility. In the human heart, there is a contraction around 48.43%. Thus, it was concluded that phantom created the deformation similar to clinical practice. The fault of the wall motion phantom was the insufficient pumping frequency by air pump version 2.0. This has been observed when the grid tagging sequences applied and the solution has been created. The latest version

of the air pump, air pump 3.0, was designed and built to solve this problem. According to the latest imaging experiments for motion phantom with the air pump 3.0, wall thickening motion phantom was capable of providing accurate data of the tagged cine images.

Overall, the rotation motion phantom and the wall motion phantom were sufficient enough to recur over and over, and the period of time required for each recurrence remained the same. The experimental setup and components of the phantoms were low-cost, simple to setup and MR-compatible. This study gives a rise to dynamic cardiac phantoms with its interesting approach to validation of new MR sequences.

CHAPTER VII

LIMITATIONS AND FUTURE WORK

7.1 Limitations

The model in this study is designed and built with rigid walls and symmetrical structures. In human heart, left ventricular wall consists of non symmetric cylindrical structure. Therefore, in vivo, left ventricle cannot be considered to have rigid walls and perfectly uniform the deformations in each cardiac cycle.

This study aims to create a model which is 100 percent MRI compatible. Neither motor nor electronic driving mechanism is not attached to system. The phantoms are human operated and this may lead to non consistent cardiac cycles in the model if the user is not well trained.

7.2 Future Work

Future studies are needed to develop a motion mechanism which will be able to operate both wall motion phantom and rotation motion phantom in the same time. One of the ideas of operating both phantoms in the same time can be improved by construction of new phantom in which wall motion and rotation motion phantoms are concentric. Since the phantoms are fully human operated, they can easily be attached to computer controlled motors to be operated automatically.

Another image analysis tool can be generated by using MATLAB to perform the analysis of the images obtained by the wall motion phantom with less user interaction.

REFERENCES

- [1] Atlas of Heart Disease and Stroke, WHO
- [2] Hunter, P. “Computational Mechanics of the Heart.” *Journal of Elasticity*, v. 61 issue 1-3, 2000, p. 113-141.
- [3] Ratib, Osman. “Morphologic and functional evaluation of congenital heart disease by magnetic resonance imaging.” *Journal of Magnetic Resonance Imaging*, v. 10 issue 5, 1999, p. 639-655.
- [4] Kubo, Naoki. “A new dynamic myocardial phantom for the assessment of left ventricular function by gated single-photon emission tomography.” *European Journal of Nuclear Medicine*, v. 27 issue 10, 2000, p. 1525-1530.
- [5] Buckberg, G., Hoffman, J., Mahajan, A., Saleh, S., and Coghlan, C. “Cardiac Mechanics Revisited: The Relationship of Cardiac Architecture to Ventricular Function.” *Circulation*, Dec 2008; 118: 2571 - 2587.
- [6] A.L. Baert, K.Sartor. Clinical Cardiac MRI. Springer-Verlag, Berlin Heidelberg, 2005.
- [7] Torrent-Guasp F, Kocica MJ, Corno AF, Komeda M, Carreras-Costa F, Flotats A, Cosin-Aguillar J, Wen H.” Towards new understanding of the heart structure and function.” *Eur J Cardio-thoracic Surg* 2005;27: 101—201.
- [8] Arts T, Prinzen FW, Snoeckx LHEH, Rijcken JM, Reneman RS. “Adaptation of cardiac structure by mechanical feedback in the environment of the cell: a model study.” *Biophys J* 1994;66:953—61.

- [9] W.J. Manning. Atlas of Cardiovascular Magnetic Resonance. Springer, Philadelphia, 2009.
- [10] J.G. Murphy, M.A. Lloyd. Mayo Clinic Cardiology. 3rd Ed., Mayo Clinic, Rochester, 2007.
- [11] R.H. Hashemi, W.G. Bradley. MRI: The Basics. Williams & Wilkins, Maryland, 1997.
- [12] Setser RM, Chatzimavroudis GP. "Magnetic Resonance Imaging Physical Principles and Instrumentation." Noninvasive Cardiovascular Imaging: A Multimodality Approach. Ed. Mario Garcia. Lippincott Williams & Wilkins, 2009.
- D.D. Stark, W.G. Bradley. Magnetic Resonance Imaging. 3rd Ed., Vol 1, Mosby, Missouri, 1999.
- [13] Nagel, E. "Assessment of systolic and diastolic LV function by MR myocardial tagging." *Basic Research in Cardiology*, v. 91 issue 1 Supl. 1, 1996, p. 23-28.
- [14] Axel, Leon. "Tagged magnetic resonance imaging of the heart: a survey." *Medical Image Analysis*, v. 9 issue 4, 2005, p. 376-393.
- [15] Venkatachari, Anand K. "Noninvasive quantification of fluid mechanical energy losses in the total cavopulmonary connection with magnetic resonance phase velocity mapping." *Magnetic Resonance Imaging (0730725X)*, v. 25 issue 1, 2007, p. 101-109.
- [16] Smith F, R., Rutt K, B., Holdsworth W, D. "Anthromorphic Carotid Bifurcation Phantom for MRI Applications" *Journal of Magnetic Resonance Imaging*, vol. 10, 1999, p.533-544.

- [17] Huber E, M., Stuber, M., Botnar M, R., Manning J, W. “Low-Cost MR-Compatible Moving Heart Phantom.” *Journal of Cardiovascular Magnetic Resonance*, 2(3), 2000, p. 181-187.
- [18] Khan, S. “Design of a dynamic cardiac MR phantom for the evaluation of cardiac MR systems.” *International Congress Series*,, 2003, p. 1165.
- [19] Visser J, N. “A realistic 3-D gated cardiac phantom for quality control of gated myocardial perfusion SPET: the Amsterdam gated (AGATE) cardiac phantom.” *European Journal of Nuclear Medicine & Molecular Imaging*, v. 31 issue 8, 2004, p. 1215-1216.
- [20] Delfino, G. Jana. “Three-directional myocardial phase-contrast tissue velocity MR imaging with navigator-echo gating: in vivo and in vitro study.” *Radiology*. 2008 Mar;246(3):917-25.
- [21] Lesniak-Plewinska, B. “A Dual-Chamber, Thick-Walled Cardiac Phantom for Use in Cardiac Motion and Deformation Imaging by Ultrasound.” *Ultrasound in Medicine & Biology*, v. 36 issue 7, 2010, p. 1145-1156.

APPENDIX



Thank You For Your Order!

Dear Mehmet,

Thank you for placing your order through Copyright Clearance Center's Rightslink service. Wolters Kluwer Health has partnered with Rightslink to license its content.

Your order details and publisher terms and conditions are available by clicking the link below:

http://s100.copyright.com/CustomAdmin/PLF.jsp?IID=2010070_1278987765126

Order Details

Licensee: mehmet ersoy

License Date: Jul 12, 2010

License Number: 2466811293126

Publication: Circulation

Title: Cardiac Mechanics Revisited: The Relationship of Cardiac Architecture to Ventricular Function

Type Of Use: Dissertation/Thesis

Total: 0.00 USD

To access your account, please visit <https://myaccount.copyright.com>.

Invoices are issued daily and are payable immediately upon receipt.

To ensure we are continuously improving our services, please take a moment to complete our [customer satisfaction survey](#).

B.1:v4.2

+1-877-622-5543 / Tel: +1-978-646-2777

customercare@copyright.com

<http://www.copyright.com>

